Title

A Better Steam Engine: Designing a Distributed Concentrating Solar Combined Heat and Power System

Permalink

https://escholarship.org/uc/item/49v9b0z1

Author

Norwood, Zachary Mills

Publication Date

2011

Peer reviewed|Thesis/dissertation

A Better Steam Engine:
Designing a Distributed Concentrating Solar Combined Heat and Power System

By

Zachary Mills Norwood

A dissertation submitted in partial satisfaction of the

requirements for the degree of

Doctor of Philosophy

in

Energy and Resources

in the

Graduate Division

of the

University of California, Berkeley

Committee in charge:

Professor Daniel Kammen, Chair
Professor Robert Dibble
Professor Duncan Callaway

Spring 2011

Abstract

A Better Steam Engine:
Designing a Distributed Concentrating Solar Combined Heat and Power System

by

Zachary Mills Norwood

Doctor of Philosophy in the Energy and Resources Group

University of California, Berkeley

Professor Daniel Kammen, Chair

The result of several years of analysis of Distributed Concentrating Solar Combined Heat and Power (DCS-CHP) systems is a design that is predicted to convert sunlight to heat at 8-10% solar-electric efficiency while simultaneously capturing ~60% of that initial sunlight as usable heat (at 100ºC). In contrast to similarly sized photovoltaic systems in the U.S. that cost ~$7.90/Watt (Wiser et al. [44]) of generator rated peak electrical output, in mass production the proposed collector and generator system sized at 1-10kW would cost ~$3.20/Watt electricity and ~$0.40/Watt-thermal, allowing adjustment of heat and electrical output on demand. The proposed system would revolutionize distributed energy generation in several ways: 1) by enabling rapid dissemination via avoidance of production limitations of photovoltaics such as expensive and limited materials, 2) by efficient local production of both heat and power to offset more greenhouse gases at a lower cost than other renewable energy technologies, and 3) by democratizing the means of electricity production; putting the power in the hands of the consumer instead of large utilities. With over 5.4 GW of photovoltaics added globally in 2008 and 20GW of solar thermal (REN21 [29]), there is a large proven market for solar energy. With widespread market penetration, this system would reduce greenhouse gas and criteria pollutant emissions from electricity generation and heating for a significant portion of the developed and developing world, including those in remote locations with no connection to an electric grid.

Chapter 1 begins with analysis of the relative demand for electricity and heat in California, showing that, on average, demand matches production of a theoretical solar CHP system. Then, we explore the economic and technological impetus for a solar powered combined heat and power Rankine cycle, showing cost and performance modeling in comparison to photovoltaics across

varying conditions, and concluding that solar CHP generated electricity is comparable to PV electricity in terms of cost "per peak watt". Chapter 2 shows results of a life cycle analysis of DCS-CHP in comparison to other renewable and non-renewable energy systems including its global warming potential (80 gCO_2eq/kWh electric and 10 gCO_2eq/kWh thermal), levelized electric and thermal energy cost ($0.25/kWh electric and $0.03/kWh thermal), and cost of solar water purification/desalination ($1.40/m^3). Additionally the utilization of water for this technology is shown to be much less than fossil-fuel based thermal power plants. Chapter 3 explores the expander as an enabling technology for small solar Rankine cycles and presents results of physical testing and characterization of a rotary lobe expander prototype developed by a small Australian company, Katrix, Inc. Testing of this expander using compressed air yields an impressive isentropic efficiency of 80-95% at pressure ratios of 6-11 making the rotary lobe expander a leading choice for DCS-CHP systems, if operation on steam is successful and reliability issues can be addressed.

Chapter 4 concludes with a description and analysis of a DCS-CHP system using simulation software developed in Matlab for the purpose of system analysis and optimization. This chapter focuses on the selection of an appropriate expander and collectors, the two key enabling technologies for DCS-CHP. In addition to discussion of the rotary lobe expander, we present a novel collector device appropriate for solar CHP systems that eliminates high pressure articulate joints, a typical failure point of solar concentrating systems. Given the results of the rotary lobe expander testing, comparison to previous expander modeling work, and comparison of the predicted cost and efficiency of the collectors analyzed, an appropriate technology version of the DCS-CHP system is selected and overall system performance is predicted across 1020 sites in the US.

Keywords: solar · CHP · Rankine · CSP · concentrating · distributed · LCA · desalination.

To my family and friends.

Contents

iii

List of Figures

List of Tables

Acknowledgments

Chapter 1

Preliminary Performance, Cost, and Demand Analysis of Solar Combined Heat and Power Systems

1.1 Background

Sustainable energy conversion is one of humankind's greatest challenges. We are beginning to realize the myriad of health and environmental effects, the most dire being global climate destabilization, that result from the combustion of fossil fuels as human society's predominant source of energy. As the political, economic, and environmental costs of fossil fuels rise, there is an urgent need for heating, cooling and electrical generation that is locally produced, cost-competitive, and nearly carbon neutral. Fortunately, solar energy is ubiquitous, and valuable when converted to high-grade heat or electricity. Yet, the solar conversion process has historically been too expensive to compete effectively against conventional power generation technologies when the economic system appropriately values neither environmental health nor social welfare (Casten and Ayres [4]).

There are currently two primary technologies for solar-electric energy conversion: photovoltaics which utilize the photo-electric effect for direct conversion of light to electricity, and solar thermal technologies that collect light as heat, typically driving mechanical-electrical generators. Combined Heat and Power (CHP) systems convert sunlight to both heat and electricity. The commercial efficiencies of PV technologies today are $10-20\%$, while commercial solar thermal systems are at $20-35\%$ solar-electric efficiency (Mills [18]). This research focuses on concentrating solar CHP for the following reasons: (a) concentrating solar CHP has the potential for $60-80\%$ solar-thermal conversion efficiency. (b) Electricity is currently very difficult to store economically; while energy in the form of heat can be cost effectively stored with available technologies. (c) Solar-thermal technology can be manufactured using abundant and easily processed engineering materials such as steel, glass, and rubber. (d) Thermal demands worldwide (including space heating and cooling) are a large fraction of total energy demands for small (less than 10kW peak) customers.

Concentrating solar CHP converts sunlight to heat and electricity from the same collector array, while photovoltaics, as the name implies, convert sunlight to electricity only. Solar thermal may thereby provide exceptionally low-cost, reliable and environmentally benign distributed generation in a variety of economies worldwide. As outlined in the 2005 Dept. of Energy publication "Basic Research Needs for Solar Energy Utilization," moderate temperature distributed concentrating solar has the potential for significant innovation to reduce the cost of solar energy (Lewis et al. [15]).

There has been especially high demand for inexpensive Distributed Generation (DG) technologies in developing regions where infrastructure does not support large-scale power plants. Distributed renewable energy has already gained notoriety in industrialized nations, where photovoltaic and wind power generation have recently seen unprecedented growth (REN21 [29]). The value proposition for DG compared to centralized generation favors DG for several reasons: (a) The price point for Levelized Cost of Electricity (LCOE) and natural gas for DG compares to electricity and natural gas at retail cost, not wholesale cost, as consumers will be producing electricity and displacing natural gas at the site of end-use. According to the U.S. Energy Information Administration the retail cost of electricity was roughly 100% greater than wholesale in 2010, giving DG this considerable advantage. (b) Distributed solar thermal is capable of

efficiently offsetting domestic demands for heating and cooling, unlike utility scale systems, which are not located in close enough proximity to end-users to take much advantage of the rejected waste heat from power generation. (c) Electrical transmission siting and efficiency concerns are alleviated because power is being generated at or near the point of use, where existing transmission infrastructure often already exists. (d) Water use for CHP technologies can be an order of magnitude less than that of average centralized electrical generation systems because heating load reduces the need for cooling water (USDOE [39]). There is demand today for small-scale solar-thermal CHP, as demonstrated by the strong growth in photovoltaics and recent growth in solar-thermal heating (Weiss et al. [42]), but distributed solar-thermal CHP technology does not exist in the marketplace today to fill that niche.

In the past, solar-thermal electric systems have been designed to operate either at high temperatures (>350˚C), as in the concentrating solar power (CSP) troughs in the central valley of California (Price et al. [26]), or at very low temperatures (<100˚C) and correspondingly low efficiencies (below 5%) (Spencer [33, 32]). To achieve the higher temperatures necessary to achieve system efficiencies above 20%, a tracking system is used that requires a moving array of collectors. This increases the efficiency of the system, but also increases cost and decreases reliability, the latter being especially undesirable for Distributed Generation (DG). With the development of low-cost concentrators that heat working fluid in excess of 200˚C, solar-thermal technologies are now viable for electrical generation and domestic heating/cooling applications (domestic hot water, refrigeration, drying, space heating/cooling, cooking, etc.). In order to efficiently produce electricity using a heat-engine, the hot side of the engine should be as hot as possible, yet typical solar-thermal collectors at working temperatures below 100˚C don't provide a sufficient temperature gradient to efficiently drive heat engine generators. Above ~150˚C, however, small heat engine generator development becomes attractive due to the increased solar-electric efficiencies such a system could produce. Our modeling predicts that 8-10% solar-electric conversion efficiency and greater than 50% solar-thermal conversion efficiency is reasonably attainable using a single-loop Rankine cycle heat engine with a variety of different possible solar collector configurations (Kalogirou [12]).

Distributed concentrating solar combined heat and power technology is on the cutting edge of 'disruptive' solar technology that could replace the traditional way heating/cooling and electricity generation is accomplished at an economic and environmental cost lower than competing technologies. In this paper we develop a new solar technology and a suite of analysis and design tools for evaluating this and other energy technologies: (1) To determine likely candidates for the expander design and working fluids for moderate temperature heat engine applications. (2) To characterize the environmental impact (energy, water, toxicity, and global warming pollution) of each potential material and process, and provide an example of how to consider these impacts during the design stage. (3) To use guiding principles of appropriate technology over the following parameters: solar conversion efficiency (Chapters 1 & 4), cost (Chapters 1 & 2), and sustainability (Chapters 1 & 2). (4) To evaluate moderate temperature expander designs and prototypes. In summary, this research is novel in the development of a small heat engine able to operate efficiently in mild concentration solar energy applications, and the integration of life cycle analysis in the early stages of design and prototyping.

In practice, the Rankine cycle a robust option for development of a solar-thermal combined heat and power system. Although many processes are interesting for thermal-electric conversion, the Rankine cycle is the most common worldwide, where an estimated 80% of all electric power is generated using a Rankine heat engine. Notably, nearly all concentrating solar power systems also use a Rankine power cycle. In comparison to the other heat engines including Brayton, Ericsson, and Stirling, the Rankine cycle has practical advantages for solar combined heat and power. Using a two-phase cycle, the majority of heat addition and heat rejection can be done isothermally (constant temperature at boiling point) which is ideal for maximizing overall system efficiency (i.e. minimizing entropy generation) . Compression work is also very low in the Rankine cycle due to the fact that liquid phase working fluid is compressed nearly isometrically (i.e. near constant volume, work is the integral of PdV). The main thermodynamic advantage the Rankine cycle holds over vapor cycles is the low compression work, on the order of 1% of the projected work output of the turbine. Compare this to a Brayton cycle where compression work may be 50% of the output of the turbine. Vapor cycles make up for this deficit by running at much higher temperatures and pressures. Providing these high temperatures with combustion is not a problem, but high temperature solar concentration adds significant cost and decreases efficiency of the collector array. Furthermore, at distributed solar temperatures (< 500K), the Brayton and Ericsson cycles need multiple stages of regeneration to achieve comparable efficiency, a need that only adds complexity and cost to a small system. Another advantage of the Rankine cycle is that a two-phase process has much improved heat transfer compared to vapor-only systems. Boiling water heat transfer in a solar collector is highly effective, and for use of the waste heat, a condenser is much preferable, in terms of cost, size and efficacy, to a vapor heat exchanger. Add to this the advantages of direct mass & heat transfer through the Rankine expander, and another advantage over a Stirling cycle becomes clear. One of the limitations of a Stirling cycle, in my experience, is that they require large amounts of heat exchange in a small area (into the engine itself) and this leads to the need to mount the engine directly in the sun to achieve decent efficiency. A Rankine cycle allows the solar collector and expander to be completely decoupled spatially, making for a more versatile and flexible system, both in terms of mounting location and ease of construction. Certainly there are applications for other thermodynamic cycles, but for low-cost, low temperatures, and reasonable second law efficiency, the Rankine cycle is an excellent choice.

The ideal solar-thermal Rankine cycle consists of the following four processes (Çengel and Boles [5]): (1) isentropic compression in a pump; (2) constant pressure heat addition in a solar collector; (3) isentropic expansion in an expander; (4) constant pressure heat rejection in a condenser. Making a few approximations and modifying the above cycle yields a reasonable approximation for an actual solar-thermal Rankine cycle, an example of which is shown in figure 1.1: (1) compression in a pump at a percentage of isentropic efficiency; (2) constant pressure heat addition in a solar collector at collector efficiency; (3) expansion in an expander at a percentage of isentropic efficiency; (4) constant pressure heat rejection in a condenser across a temperature gradient. This cycle ignores pressure losses in the pipes, but this effect is small compared to the other effects being modeled.

A preliminary solar Rankine model was constructed in Engineering Equation Solver software (EES) as shown in figure 1.2, allowing for rapid thermodynamic analysis using different
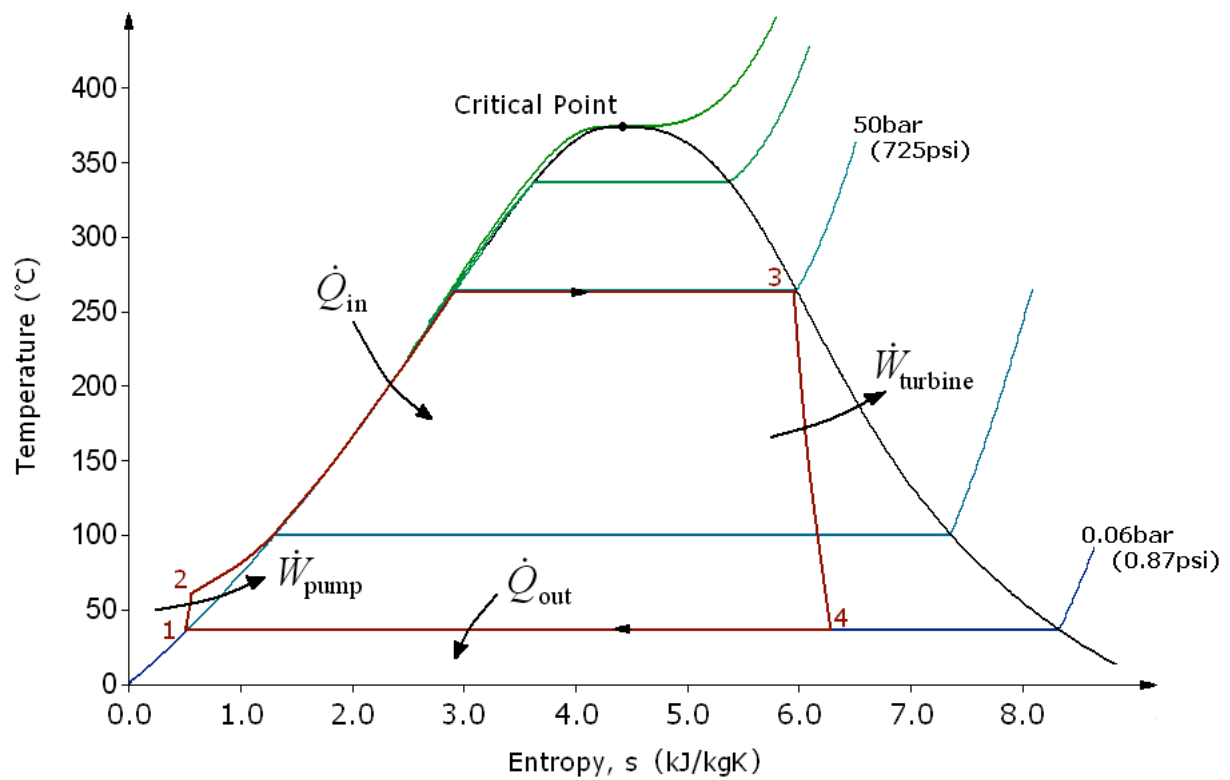
Figure 1.1: A typical wet steam Rankine cycle on a temperature-entropy diagram
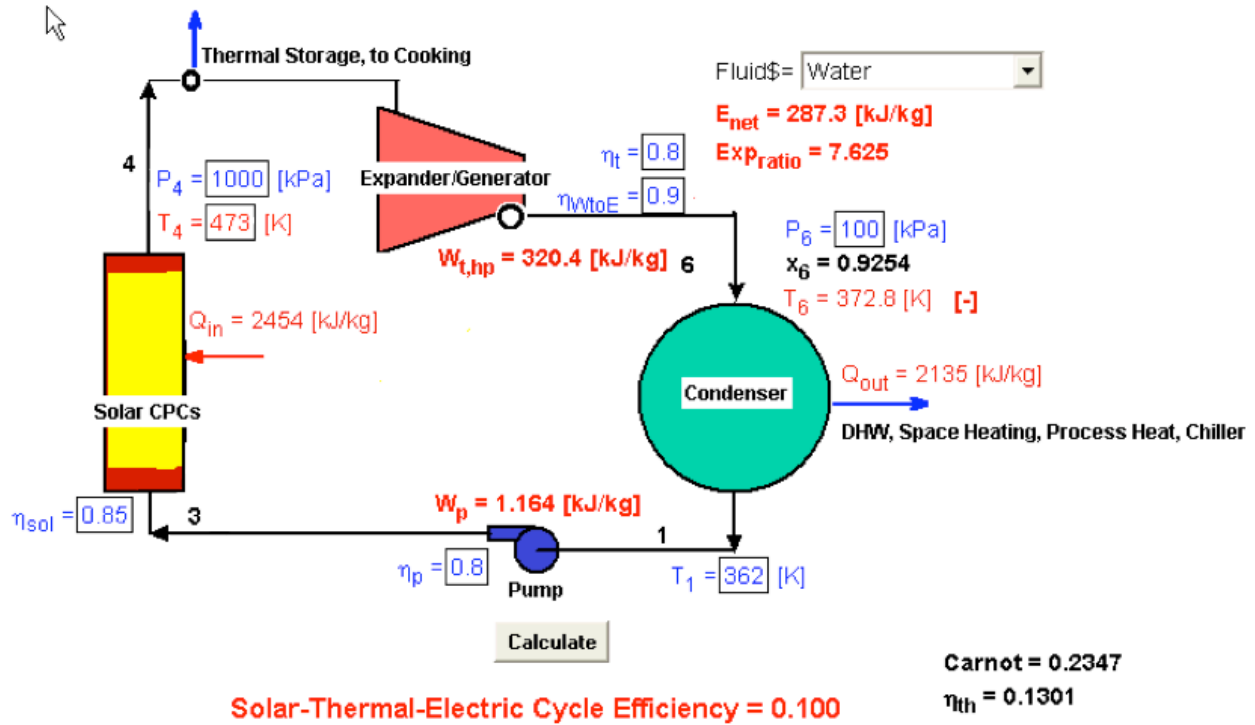
Figure 1.2: Rankine cycle for DCS-CHP modeled in EES

components and working fluids. Note that greater than 50% of Carnot efficiency is theoretically achievable with moderate temperatures (less than 250ºC), pressures (less than 11bar), and with a ubiquitous harmless fluid (water). Not any other thermodynamic cycle for solar power generation exhibits such promising results with attainable technology that is also appropriate for household or unsupervised operation. For instance, plumbing code in California requires that for steam operation much above these temperatures and pressures that a full-time on-site operator be present. Such requirements would practically rule out many other heat engine systems at small scale. Toxic or exotic working fluids are also eliminated in steam Rankine systems, making them a benign choice, and a low-cost choice for heat and electricity.

1.2   Solar Rankine thermodynamics matches California demand

To get a first approximation of the market impact such a technology would have, five scenarios for combined heat and power are considered, using average California solar insolation data with electric and natural gas demand data in Pacific Gas and Electric (PG&E) territory. These scenarios evaluate the potential for solar-thermal serving domestic hot water, space heating, and cooling (A/C) loads. The modeled system is sized to meet average electrical demand for each scenario, with results shown in figure 1.3. Notice the trend from Scenario 2 to Scenario 5 for less
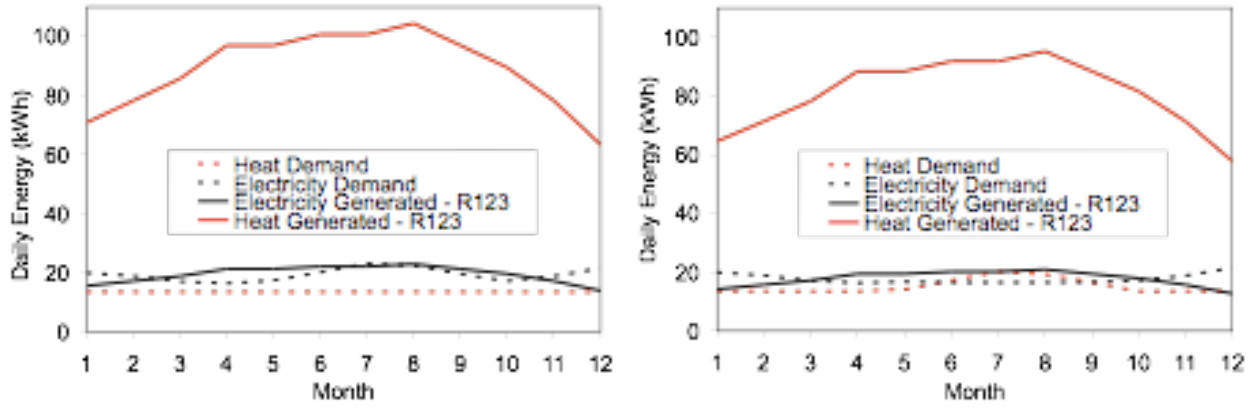
(a) Scenario 2: Household electrical and hot water loads served by solar

(b) Scenario 3: Household electrical and air-conditioning loads served by solar
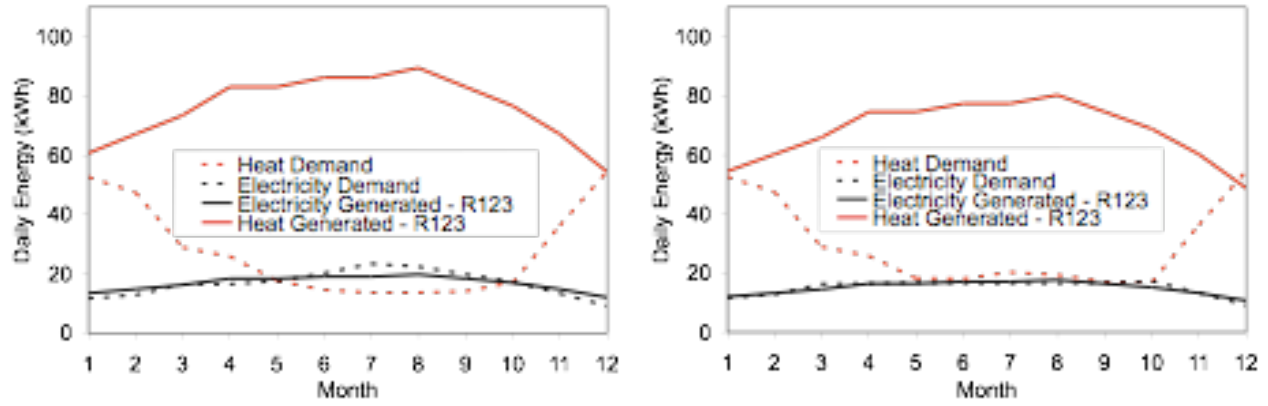
(c) Scenario 4: Household electrical, hot water and space heating loads served by solar

(d) Scenario 5: Household electrical, hot-water, air-conditioning, and space heating served by solar

Figure 1.3: Average California residential daily demand compared with the solar Rankine system's expected output of electricity (using R123 working fluid). (Norwood et al. [21])

heat generation and correspondingly smaller system size as more loads are shifted from electrical to thermal. This shifting of load is indicative of more efficient end-use of energy as thermal energy is used to serve thermal loads and electrical energy is used to supply only those loads that require electricity. Scenario 5 requires just under 30m^2 of panels to produce all the electricity, hot water, A/C (using absorption chillers) and space heating for an average California residence, assuming adequate storage is available to ride-through periods of inclement weather without sufficient solar radiation.

The A/C and space heating electrical demand that could be offset by solar-thermal was calculated throughout the year using industry average demand data provided by PG&E. Note that this model predicts that all thermal demands in all scenarios considered will be reasonably met with a system sized to meet yearly electrical demands. Note that the almost exactly coincident 'electricity

7

demand' and 'electricity generated' curves indicate a good temporal match of average demand to average production of the DCS-CHP system for this central California location. Note also that the result in scenarios 2 and 5 assumes heat driven absorption or adsorption cooling systems are in widespread use, although small customers rarely use these systems today. This analysis is not indicative of actual energy demand or output for any given California residence or solar system, but is nonetheless useful in determining how, in aggregate, wide-scale dissemination of DCS-CHP systems could meet our current California energy demands. The applicability of this technology in other locations will of course depend on the shape of their respective load curves.

1.3 Performance-Cost analysis of solar combined heat and power systems

Solar combined heat and power (CHP) systems can compete or exceed solar photovoltaics (PV) – which is often used as the benchmark in terms of efficiency, performance, and cost – in a range of distributed generation applications, and across a range of specific technology platforms. A common metric to evaluate the cost of photovoltaics is a cost per peak power output or "dollars per watt" metric. For the purpose of comparison, we develop a new analytic methodology to evaluate the cost of the electricity generated from a solar CHP system. The electricity generation and thermal subsystems of a solar CHP system are energetically intertwined, yet by comparing thermal and electrical outputs a sensible cost division can be determined. This method is then used to compare the cost of stationary PV and solar Rankine CHP systems with tracking and stationary collectors. The capacity factors of electricity generation for each system is found in simulation using NREL TMY3 climatic data for 1020 sites in the United States. The solar Rankine system with stationary collectors outperforms the PV system in warmer and sunnier climates relative to its rated "dollar per watt" output, while PV outperforms solar Rankine in cooler climates. With tracking concentrating collectors, the solar Rankine system outperforms PV systems in the vast majority of US sites at an estimated cost of $4/W and a collector high temperature of 250°C. In conclusion, a PV system and solar Rankine CHP system, sized equally in terms of peak power output, will produce comparable amounts of electricity (+/- 10% on average), however the solar Rankine CHP system will additionally provide 4 to 6 units of useful heat energy for every one unit of electricity generated.

1.3.1 Nomenclature

c Overall cost of peak electrical output $\left[\frac{\$}{\text{W}_{el}}\right]$

c_e Electric power subsystem cost per unit of peak output $\left[\frac{\$}{\text{W}_{el}}\right]$

C Overall cost per unit area of collector $\left[\frac{\$}{\text{m}^2}\right]$

C_c Collector subsystem cost per unit area of collector $\left[\frac{\$}{\text{m}^2}\right]$

C_x	Collector subsystem cost not offset by heat production, per unit area of collector $\left[\frac{\$}{\text{m}^2}\right]$
C_e	Electric power subsystem cost per unit area of collector $\left[\frac{\$}{\text{m}^2}\right]$
η_c	Collector efficiency
η_0	Carnot efficiency of Rankine cycle
η_p	Fraction of Carnot efficiency achieved in Rankine cycle
η_r	Overall efficiency of Rankine cycle
η_t	Fraction of waste heat recovered from Rankine cycle
G	Reference insolation level $\left[\frac{\text{W}}{\text{m}^2}\right]$
P_c	Collector heat output per unit area of collector $\left[\frac{\text{W}_{th}}{\text{m}^2}\right]$
P_t	Useful heat output of system $\left[\frac{\text{W}_{th}}{\text{m}^2}\right]$
P_x	Heat output of heat-only system not offset by CHP heat output
P_e	Electrical power output of system $\left[\frac{\text{W}_{el}}{\text{m}^2}\right]$
Q	Solar CHP to PV yearly performance ratio
R	Actual ratio of thermal to electrical power output
R_d	Desired ratio of thermal to electrical power output
T_a	Ambient temperature $[\text{K}]$
T_h	Rankine cycle high temperature (expander inlet) $[\text{K}]$
T_m	Heating load supply temperature (collector or expander outlet) $[\text{K}]$
T_l	Heating load return temperature (collector inlet) $[\text{K}]$
W_{CHP}	CHP system's electrical energy produced over a year $[\text{J}]$
W_{PV}	PV system's electrical energy produced over a year $[\text{J}]$
E, A, B	Collector performance coefficients $[\%]$, $\left[\frac{\text{W}}{\text{m}^2\text{K}}\right]$, $\left[\frac{\text{W}}{\text{m}^2\text{K}^2}\right]$
$[\,]^*$	Starred quantities refer to system producing heat only
$\bar{[\,]}$	Barred quantities refer to systems at reference conditions

1.3.2   Performance-Cost methodology

Distributed solar electric systems currently use photovoltaics almost exclusively. These systems are often compared on the basis of "dollars per watt," which represents the total cost of the installation divided by its peak electrical power output. Since different photovoltaic (PV) systems can be expected to react similarly under changing conditions, it is reasonable to compare them on the basis of this single reference point.

Solar combined heat and power (CHP) systems, however, produce both electricity and useful heat. While this dual output makes solar CHP systems potentially more valuable in distributed applications, it also makes their value more difficult to quantify and compare. One straightforward solution is to compare the overall costs and long term outputs of potential systems for a specific application. This method, however, produces application specific results that are not easily generalized.

Instead, an analytical method is developed to enable direct comparison of solar combined heat and power and PV technologies, based on the existing metric of dollars per peak electrical watt. It is intended to capture the major factors that affect solar CHP system performance, such as collector performance, unit costs, temperature limits, and efficiencies. At the same time, it attempts to avoid application specific information like system size and local meteorology.

Here, the method is developed for two variations on a solar Rankine system with either stationary evacuated tube collectors, or tracking concentrating dish collectors supplying heat to a Rankine cycle. The method is described conceptually, then derived analytically. The method is then used to estimate the cost of solar Rankine CHP systems with different types of collectors, and to compare them to PV systems. The assumption that PV and solar Rankine systems can be compared on the basis of this one reference point (cost per peak electrical watt) is tested by comparing the model to a parametrization of the real-world relative performance of each system. While the behavior of PV and solar CHP systems can diverge considerably under some circumstances, the systems are found to behave with reasonable similarity overall in terms of average electrical output. Thus, the "dollars per watt" metric represents overall performance well enough to justify its use in the preliminary design of solar Rankine systems, and in generalized comparisons to photovoltaics. In terms of heat output, the solar Rankine system will provide 4 to 6 units of thermal energy and one unit of electrical energy for every one unit of electrical energy produced by the same size (peak Watts electric) PV system.

To evaluate distributed solar CHP systems on the basis of cost per peak electrical watt, it is necessary to account for the value of the useful heat that is also produced. This is done by conceptually dividing the system into two parts: a collector subsystem and a power generation subsystem. The collector subsystem consists of the solar collectors and their associated equipment, such that it could embody a stand-alone solar heating system. It is assumed that this hypothetical stand-alone system would produce heat cost effectively (a reasonable assumption, since the collector technology is designed for solar hot water applications). The power generation subsystem consists of all the additional equipment necessary to produce electrical power from the thermal output of the collector subsystem.

With the system divided as such, it is now possible to determine the cost of its electrical output.
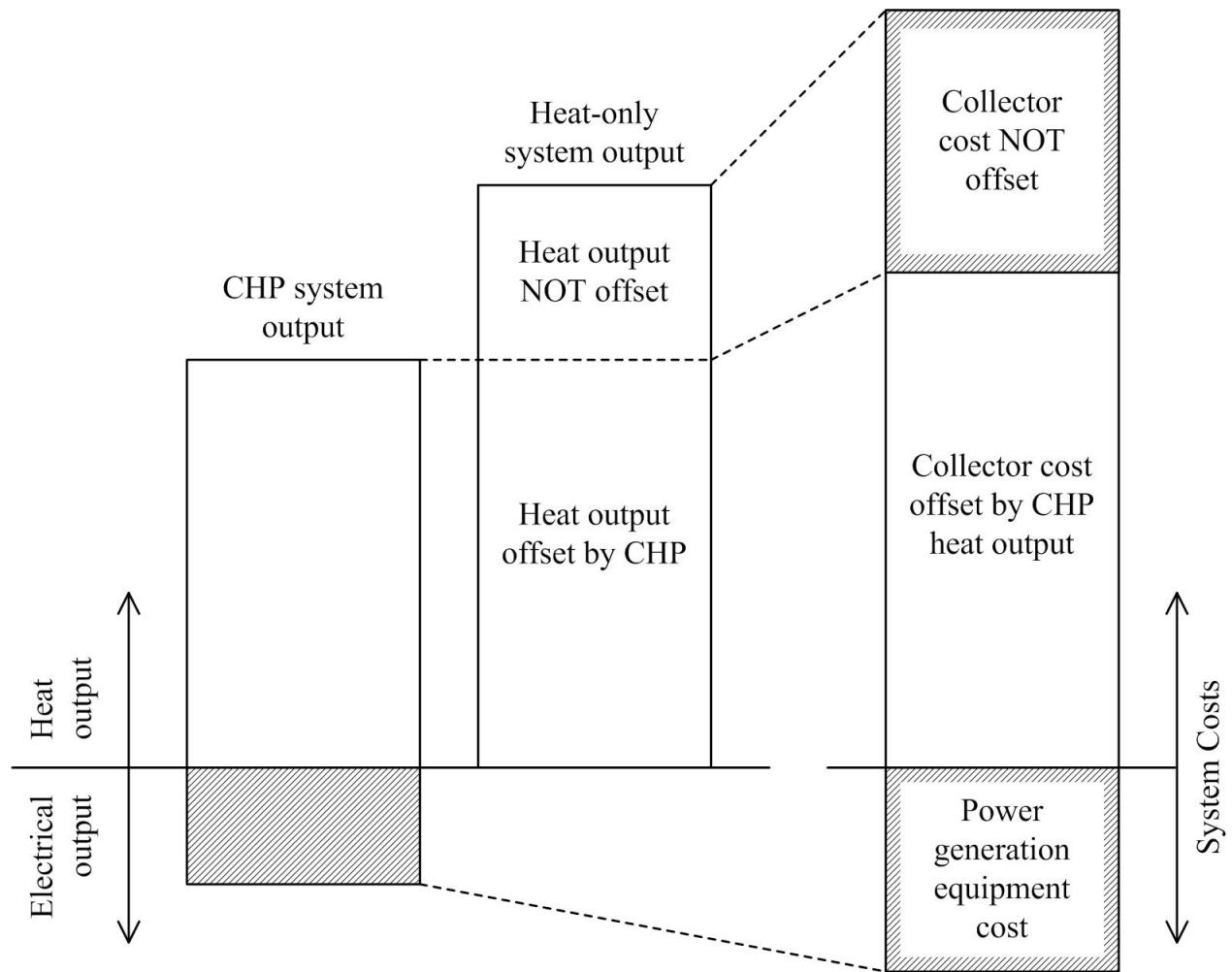
Figure 1.4: Distribution of collector costs; shaded regions represent power generation costs

Clearly, the cost of electricity should include the entire cost of the power generation subsystem. It should also include a portion of the collector cost: because the collectors operate less efficiently at the high temperatures necessary for power generation, and because some thermal energy is converted to electricity, the CHP system produces less useful heat than the collector subsystem would if operating independently. Thus, for the CHP system's heat output to remain economical, its electrical output must pick up some of the cost of the collector subsystem.

This cost accounting is achieved by comparing the CHP system output to that of an equally sized system producing heat alone. The heat produced by the CHP system offsets some of the heat that could have been produced by a heating-only system. Some portion of heat is not offset, however, so the power generation system picks up an equal portion of the collector subsystem cost. This is illustrated in figure 1.4.

In this way, the cost of electrical power accounts for both the extra equipment needed to generate that electrical power, and the required size increase of the collector subsystem. Meanwhile, the cost of thermal power remains equal to that of the heating-only system, which is assumed to be
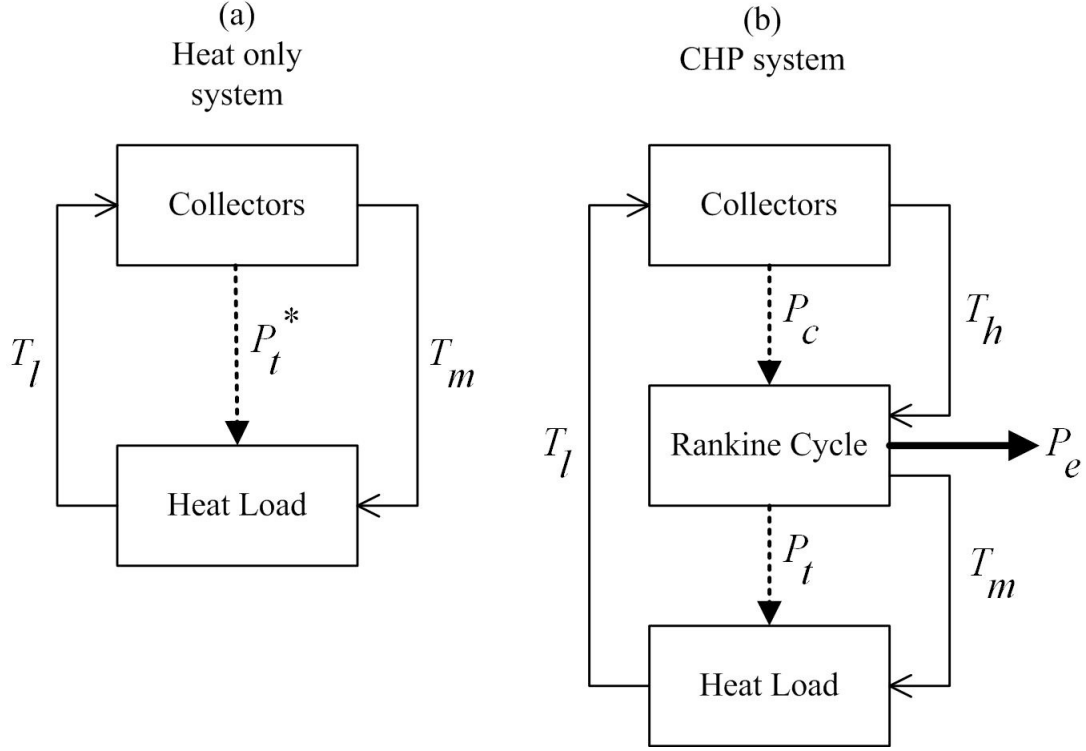
Figure 1.5: Heat-only and CHP system diagrams

economical.

1.3.2.1   Collector producing heat only

First, we evaluate the performance of the collector subsystem producing heat only. This system is shown in figure 1.5, diagram (a). The collector efficiency is a function of the ambient temperature T_a, the collector supply and return temperatures T_m and T_l, and the reference (peak) insolation G.

$$\eta_c^* = f\left(G, T_a, T_l, T_m\right) \tag{1.1}$$

The collector heat output per unit area is then

$$P_c^* = \eta_c^* G \tag{1.2}$$

The entire collector heat output is useful thermal power, so that

$$P_t^* = P_c^* \tag{1.3}$$

12

1.3.2.2 CHP system: General case

A solar CHP system produces both useful heat P_t and electricity P_e. Its cost, as discussed above, is the sum of the power generation subsystem cost C_e and the cost of the collector subsystem not offset, C_x.

$$C = C_e + C_x \tag{1.4}$$

These costs are evaluated per unit area of collector. The overall cost per unit of peak electrical output is found by dividing through by P_e:

$$
\begin{aligned}
c &= \frac{C}{P_e} \\
&= \frac{C_e}{P_e} + \frac{C_x}{P_e} \\
&= c_e + \frac{C_x}{P_e}
\end{aligned}
\tag{1.5}
$$

The cost of the collector subsystem not offset, C_x, is proportional to the amount of heat not offset, P_x^*, as illustrated in figure 1.4.

$$\frac{C_x}{C_c} = \frac{P_x^*}{P_t^*} \tag{1.6}$$

The amount of heat not offset is equal to the difference between the heat-only system output P_t^* and the CHP heat output P_t, as shown in figure 1.6. Solving for C_x and plugging it into eq. 1.5, the CHP system cost of electrical power is obtained. Shown in eq. 1.8, the final cost is calculated in terms of standard quantities: the power generation subsystem cost per unit of electrical power output (c_e), the collector cost per unit area (C_c), and the thermal and electrical power outputs that, it will be shown, can be calculated from estimated efficiencies and temperatures.

$$
\begin{aligned}
C_x &= C_c \frac{P_x^*}{P_t^*} \\
&= C_c \left(1 - \frac{P_t}{P_t^*} \right)
\end{aligned}
\tag{1.7}
$$

$$c = c_e + \frac{C_c}{P_e} \left(1 - \frac{P_t}{P_t^*} \right) \tag{1.8}$$

This analysis assumes all of the CHP system's thermal output is useful and valued. To evaluate whether this is the case, while remaining independent of system size, the ratio of heat output to electrical output R is calculated.

13
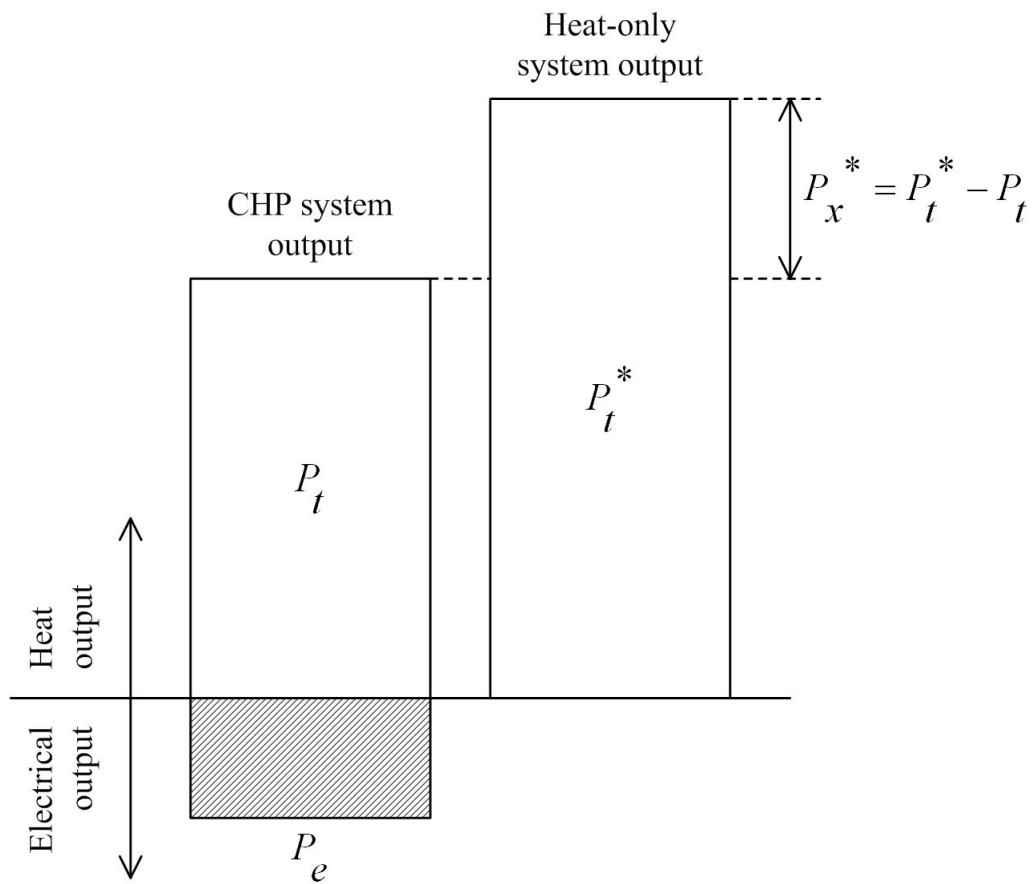
Figure 1.6: Determining the heat output that is not offset

$$R = \frac{P_t}{P_e} \tag{1.9}$$

If this ratio is too large for the application, a desired ratio R_d can be substituted for R. For example, California homes consume about one to five times as much thermal energy as electrical, depending on the season (Norwood et al. [21]).

$$
\begin{aligned}
R_d &= \frac{P_{t-useful}}{P_e} \\
&\leq R
\end{aligned}
\tag{1.10}
$$

Of course, if less heat is useful and valued, then less of the collector subsystem cost is offset, and the cost of the CHP system's electrical output will rise accordingly. Eq. 1.11 gives the cost of electrical power in terms of the desired heat-to-electricity ratio R_d.

$$
\begin{aligned}
c &= c_e + \frac{C_c}{P_e}\left(1 - \frac{P_{t-useful}}{P_t^*}\right) \\
&= c_e + \frac{C_c}{P_e} - \frac{C_c R_d}{P_t^*}
\end{aligned}
\tag{1.11}
$$

1.3.2.3 Rankine cycle power: Special case

In the previous section, the analysis considered a solar CHP system supplying arbitrary heat and power outputs. Now, a special case is considered, wherein the collector output is used to run a Rankine cycle at a high temperature T_h. The heat load is supplied by waste heat rejected from the Rankine cycle condenser at temperature T_m, and working fluid returns to the collector at low temperature T_l. This system is shown schematically in diagram (b) of figure 1.5. The collector efficiency is recalculated in terms of T_h:

$$\eta_c = f\left(G, T_a, T_l, T_h\right) \tag{1.12}$$

The overall Rankine cycle efficiency η_r is a function of the Carnot efficiency η_0 (which is the maximum theoretical efficiency for any heat engine operating between a high temperature source and low temperature sink) and the anticipated percent of the Carnot efficiency the cycle is expected to achieve, η_p.

$$
\begin{aligned}
\eta_r &= \eta_p \eta_0 \\
&= \eta_p\left(1 - \frac{T_m}{T_h}\right)
\end{aligned}
\tag{1.13}
$$

The CHP system's heat and electricity outputs (as always, per unit area of collector) are functions of these efficiencies and the fraction of waste heat that is expected to be recovered for use by the heating load (η_t). As such, P_e and P_t are no longer arbitrary. Rather, they are determined by the specific solar CHP scheme under consideration: its structure, temperatures, and expected efficiencies.

$$
\begin{aligned}
P_e &= \eta_r P_c \\
&= \eta_r \eta_c G
\end{aligned}
\tag{1.14}
$$

$$
\begin{aligned}
P_t &= (1 - \eta_r)\, \eta_t P_c \\
&= (1 - \eta_r)\, \eta_t \eta_c G
\end{aligned}
\tag{1.15}
$$

The cost of electricity is calculated by plugging P_e and P_t into eq. 1.8. As before, this cost represents the total cost per peak watt of electrical output. It is independent of system size (to the extent that its inputs are independent of system size) and is a function of unit component costs, temperatures, and anticipated efficiencies.

$$
\begin{aligned}
c &= c_e + \frac{C_c}{P_e}\left(1 - \frac{P_t}{P_t^*}\right) \\
&= c_e + \frac{C_c}{\eta_r \eta_c G}\left(1 - \frac{(1 - \eta_r)\, \eta_t \eta_c G}{\eta_c^* G}\right) \\
&= c_e + \frac{C_c}{G}\left(\frac{1}{\eta_r \eta_c} - \frac{\eta_t}{\eta_r \eta_c^*} + \frac{\eta_t}{\eta_c^*}\right)
\end{aligned}
\tag{1.16}
$$

The ratio of thermal to electrical power output R of this system is

$$
\begin{aligned}
R &= \frac{(1 - \eta_r)\, \eta_t \eta_c G}{\eta_r \eta_c G} \\
&= \eta_t \left(\frac{1}{\eta_r} - 1\right)
\end{aligned}
\tag{1.17}
$$

If less heat is required per unit electrical output, eq. 1.16 is recalculated using R_d:

$$
\begin{aligned}
c &= c_e + \frac{C_c}{P_e} - \frac{C_c R_d}{P_t^*} \\
&= c_e + \frac{C_c}{G}\left(\frac{1}{\eta_r \eta_c} - \frac{R_d}{\eta_c^*}\right) \quad \text{where } R_d \leq \eta_t \left(\frac{1}{\eta_r} - 1\right)
\end{aligned}
\tag{1.18}
$$

16

1.3.3 Application to a potential system

The cost of a solar Rankine CHP system, like the one described in the previous section, is estimated using the properties listed in Table 1.1with sources. In this table, estimates are provided for a steam Rankine cycle heat engine achieving 50% of Carnot efficiency in electrical generation operating at the high and low temperatures indicated with 80% waste heat recovery. Three hypothetical systems are compared using different collector arrays, all assumed to have the same cost per aperture area. Two systems use evacuated tube collectors with efficiency calculated using eq. 1.19, given manufacturer supplied constants E, A, and B.

$$\eta_c^* = E - \frac{A}{G}\left(\frac{T_{inlet} + T_{outlet}}{2} - T_a\right) - \frac{B}{G}\left(\frac{T_{inlet} + T_{outlet}}{2} - T_a\right)^2 \qquad (1.19)$$

The third system uses a model for a tracking concentrating dish collector, where the collector performance coefficients come from published data for a trough collector (trough coefficients are comparable to those for a dish collector). Direct normal solar insolation is used in eq. 1.19 to calculate collector efficiency. Rather than being fixed from the outset, the collector output temperature T_h is varied to find the operating point that minimizes the installed cost of electricity. All other things being equal, because collector efficiency decreases and Rankine cycle efficiency increases with increasing collector temperature, there is a minimum (optimum) cost point for these systems. Using these values and eq. 1.16 the installed cost of this hypothetical system with non-concentrating evacuated tube collectors would be about $\$6.00/\mathrm{W}_{el}$, at an optimal collector output temperature of approximately$170°$C, and with tracking dish collectors would be $\$4/\mathrm{W}_{el}$ at a collector temperature of $250°$C, as seen in figure 1.7. This cost compares favorably to residential ($P_e < 10$kW) photovoltaic systems that were $\$7.90/\mathrm{W}_{el}$ installed in 2007(Wiser et al. [44]). The relative thermal to electric output ratio for the evacuated tube systems would be approximately 6:1, and for the dish system 4:1.

This cost assumes that all of the heat produced (in this case 4-6 units of heat for every unit of electricity) is useful. If the demand for heat is less ($R_d < R$), the cost of electricity rises as does the optimal collector output temperature. This suggests that solar Rankine systems will be most economical where there exists a large demand for low temperature heat (below $100°$C) relative to demand for electricity. In such cases, $R_d = R$: the entire waste heat stream is useful and valued, so the cost of electricity is minimized.

1.4 Verification of the model for comparison to PV

The cost metric developed here considers system performance at a specific set of reference conditions (essentially summer peak performance). While it may suggest that a specific solar Rankine system is cost competitive with PV, this conclusion is supported only at such conditions. At other conditions, which depend on location, weather, and diurnal and seasonal variations, the performance of a solar CHP system to that of a PV system remains unknown. For example, one could imagine a solar CHP system that performed brilliantly in ideal conditions, but dismally in
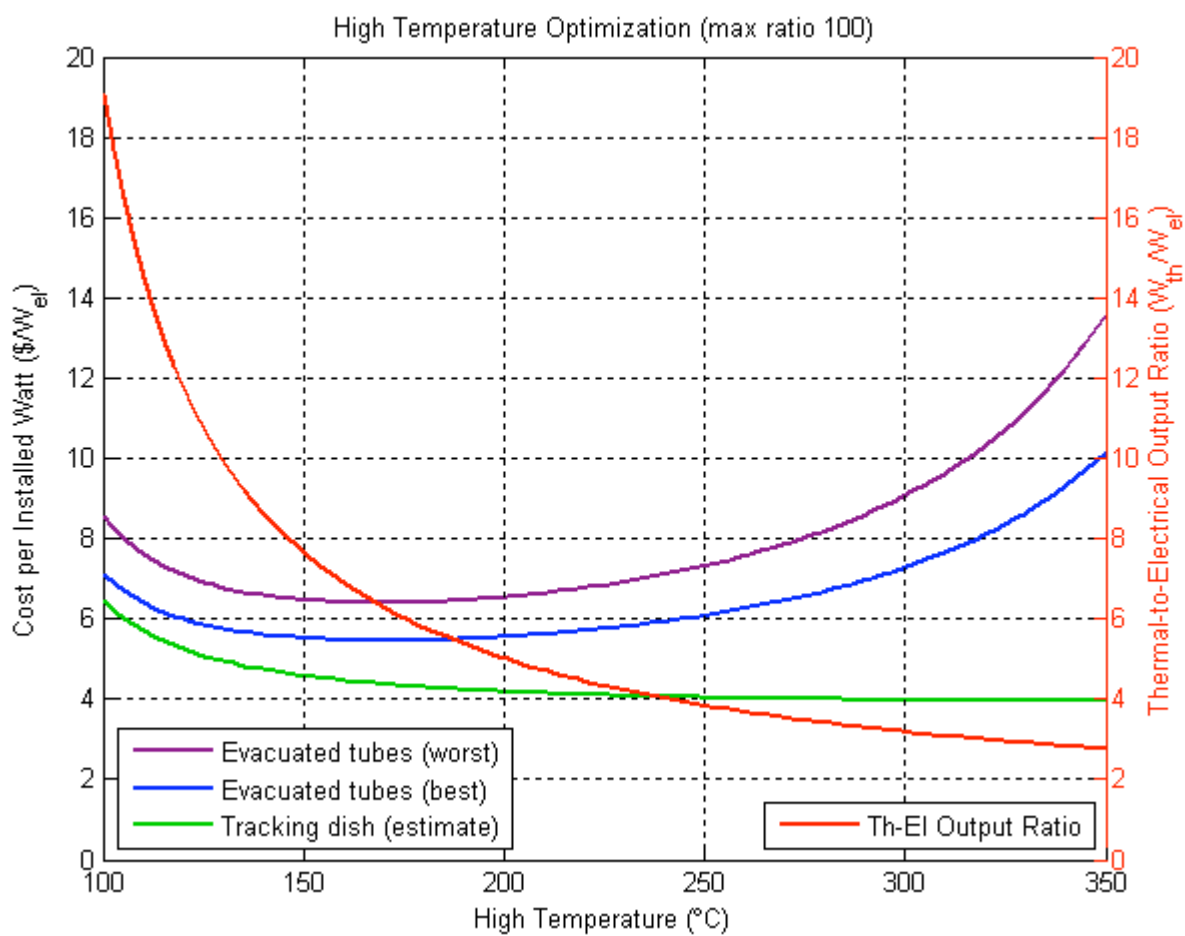
Figure 1.7: Cost and performance optimization results

Table 1.1: Modeled solar CHP systems' properties

	Tubes (worst)	Tubes (best)	Dish	Source
T_h	variable	variable	variable	Vary to find high temperature at lowest cost
T_m	70°C	70°C	70°C	Required heat load temperature, plus margin
T_l	14.5°C	14.5°C	14.5°C	Ambient temperature, plus margin
η_p	50%	50%	50%	Estimated percent of Carnot efficiency achieved
η_t	80%	80%	80%	Estimate of waste energy recovered
c_e	$2.50/W_{el}$	$2.50/W_{el}$	$2.50/W_{el}$	Small Rankine power subsystem (Mills [18])
C_c	$500/m^2$	$500/m^2$	$500/m^2$	Cost bid for small dish collectors (RawSolar [27])
E	61%	80%	76%	Tubes (worst): GreenOneTec VK4000 (Müller-Steinhagen [20])
A	0.85	1.2	0.21	Tubes (best): Thermomax (Mahjouri [16])
B	0.010	0.012	0.0017	Dish (estimate): IST trough (Kalogirou [12])
G	$1000\frac{W}{m^2}$	$1000\frac{W}{m^2}$	$1000\frac{W}{m^2}$	Standard reference insolation level

marginal conditions. This system would appear competitive in terms of cost per peak electrical watt, but would perform poorly on the whole.

Thus, solar CHP and PV systems can be compared on the basis of peak performance only if they behave similarly in changing conditions. In other words, the metric of peak electricity cost is meaningful only to the extent that it reflects long term, condition dependent performance.

To evaluate whether solar CHP and PV systems perform similarly in changing conditions, their respective performance over one year is modeled at a variety of locations. This is accomplished by creating a Matlab software simulation based on NREL's TMY3 data, which provides solar radiation and other environmental data for one "typical meteorological year" at 1020 sites throughout the United States. For each location, the electrical output of each system, W_{CHP} and W_{PV} are calculated. Next the capacity factor of each system is found by dividing each system's electrical output by its output at reference conditions, $\bar{W}_{CHP}$ and $\bar{W}_{PV}$ ($1000\frac{\text{W}}{\text{m}^2}$ direct normal and $14.5°$C ambient temperature). Finally, the capacity factors are compared by finding the CHP-PV performance ratio Q:

$$Q = \frac{CapacityFactor_{CHP}}{CapacityFactor_{PV}} = \frac{\frac{W_{CHP}}{\bar{W}_{CHP}}}{\frac{W_{PV}}{\bar{W}_{PV}}} \tag{1.20}$$

If, for a particular location and time period $Q = 1$, the systems are expected to behave similarly: comparing them on the basis of peak power is fair because it represents overall performance equally well for both systems. However, if $Q > 1$, the solar Rankine system will perform better than determined by the peak power comparison, because its capacity factor exceeds that of the equivalent PV system. If $Q < 1$, the opposite is true: the peak power comparison is overly optimistic for the solar Rankine system.

The CHP-PV Performance Ratio could be found for any time scale (hour, day, month, season, or year). In this model, it is calculated on yearly and seasonal bases, to capture the overall differences in system performance, and their variation throughout the year. In figures 1.8, 1.9, 1.10, and 1.11 the yearly and seasonal CHP-PV Performance Ratios of a stationary evacuated tube (good) system and a tracking concentrating dish system with characteristics given in Table 1.1 are plotted for sites in the US on a longitude vs. latitude axis. The data plotted indicates the expected relative electrical output (performance ratio as defined above) over one year under typical weather conditions.

These results show that comparisons between solar CHP and PV systems depend to some extent on location. In general, the stationary collector solar CHP system is expected to perform better (relative to a comparably rated PV system) where and when insolation is highest (that is, during the summer months and in locations that are sunny year round) as seen in figures 1.8 and 1.9. For example, a stationary collector solar CHP system based in Las Vegas (where $Q > 1$) would be more economical with respect to PV than predicted by the "cost per watt" figure. Likewise, a stationary solar collector CHP system based in New England (where $Q < 1$) would be less cost effective than a PV system with an identical cost per watt. However, on the whole, stationary solar collector CHP and PV system performance are quite comparable (Q is close to 1), with relative performance ratios of 0.4 to 1.15 and an average of 0.93 over all sites. Stationary
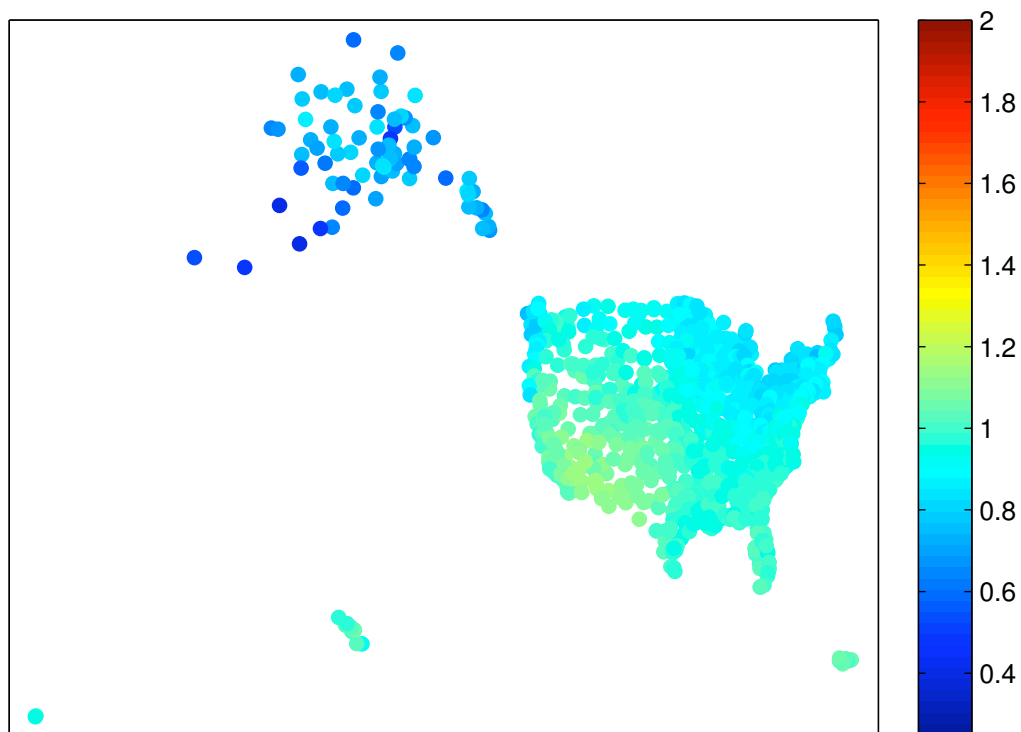
Figure 1.8: Stationary collector CHP to stationary PV performance ratio over a year (Range 0.4 to 1.15, Mean 0.93)
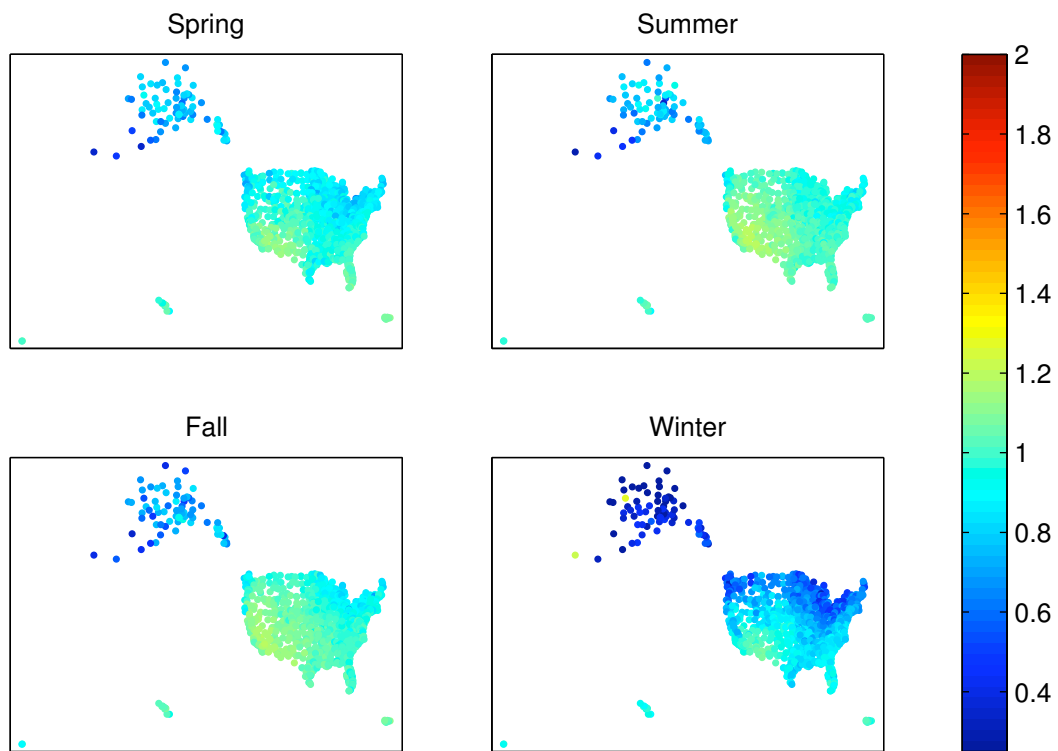
Figure 1.9: Stationary collector CHP to stationary PV performance ratio by season
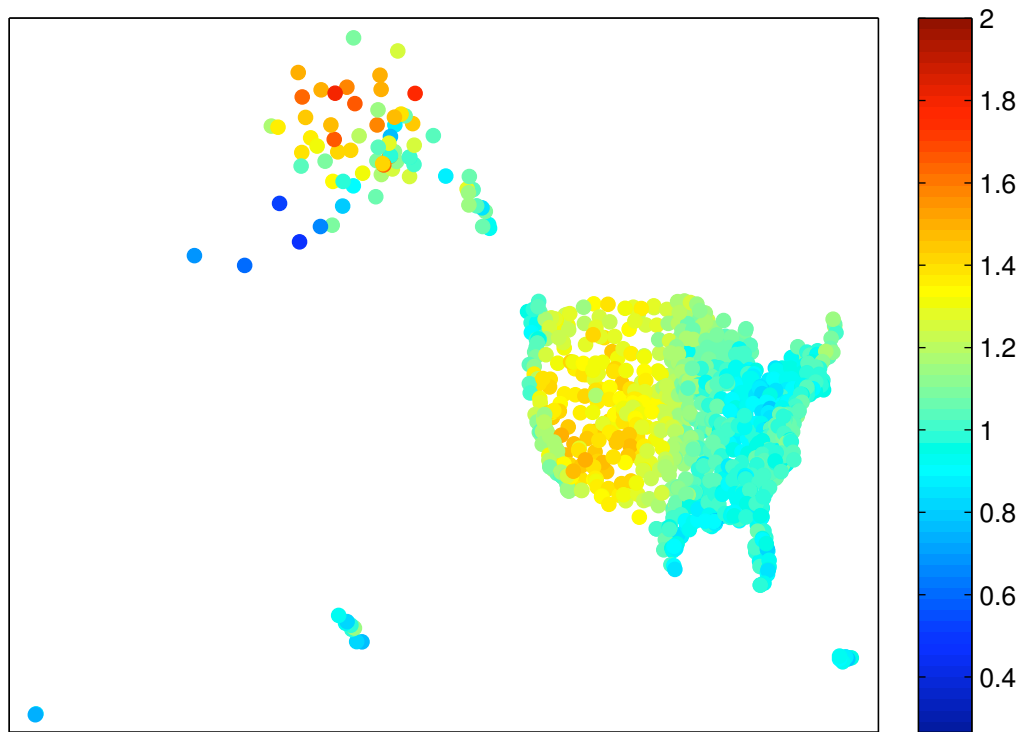
Figure 1.10: Tracking collector CHP to stationary PV performance ratio over a year (Range 0.48 to 1.8, Mean 1.1)
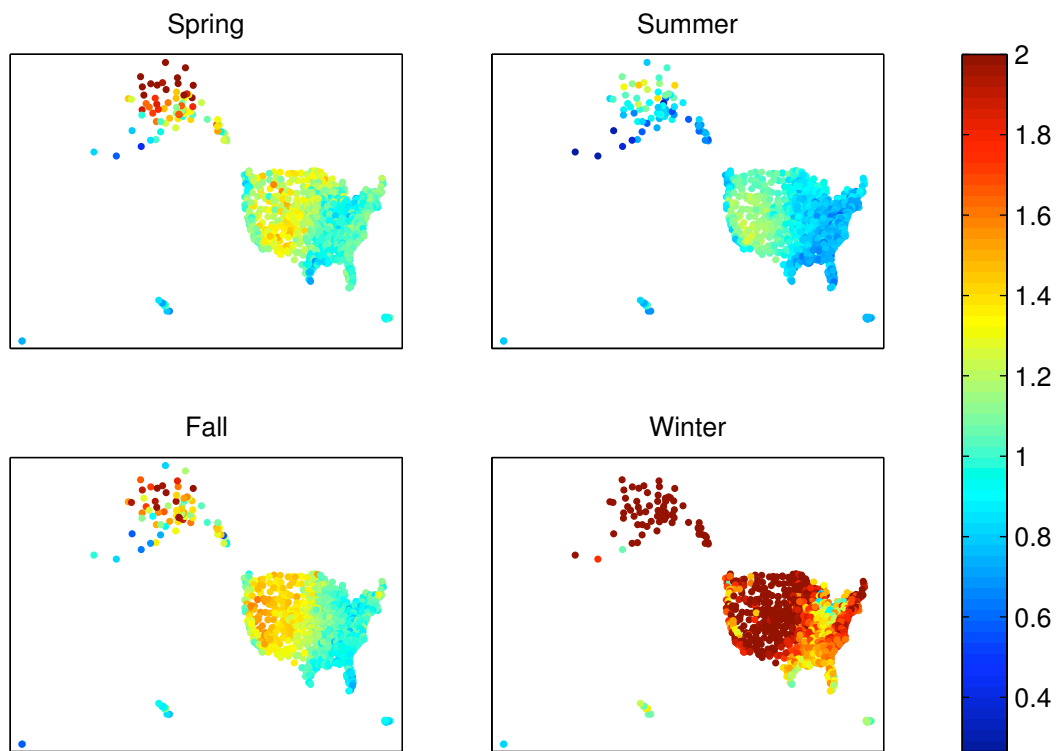
Figure 1.11: Tracking collector CHP to stationary PV performance ratio by season

collector solar CHP system performance is especially advantaged where insolation is highest. Thus, the cost per watt metric is most conservative with respect to solar CHP systems in locations where it makes the most sense to utilize a solar power system to begin with.

Comparing tracking solar CHP systems to stationary PV yields a very different seasonal result seen in figure 1.11, but the same general comparability exists in overall capacity factors for the two systems. The tracking system (always facing the sun) when compared to a stationary PV system (tilted at latitude) will perform much better in many northerly locations, like Alaska, because cosine losses will be highest for the stationary collectors in that season. The tracking dish system will also outperform the PV system in locations where most sunlight is direct, and little diffuse light is collected. Because aperture angle and concentration are inversely related, the tracking collector is unable to collect much light on cloudy days, whereas the stationary system is relatively good at collecting diffuse light coming from a wide swath of sky. The modeled range of performance ratios of tracking collector solar CHP to stationary PV is 0.48 to 1.8, and 1.1 on average over all sites.

1.5   Discussion and conclusions

A sensitivity analysis of the modeling results discussed in this chapter shows that collector costs, collector efficiency, and expander efficiency most heavily influence the cost results. This is intuitive based on the efficiency calculations derived earlier in this chapter. For instance, it is not surprising that the pump's isentropic efficiency has a relatively small effect on solar-electric system efficiency, given that pump work is on the order of 1% of the turbine output in this Rankine cycle. Collector efficiency and expander efficiency, on the other hand, heavily influence the cost of the system because the collector array is such an expensive component, and any significant decrease in either the collector efficiency or that of the heat engine significantly impacts the levelized cost of energy generated. The efficiency and pressure ratio of the expander are the most important variables in determining overall heat engine efficiency and also have a large effect on the ratio of electric to thermal energy delivered. Both the generator and the collector are multiplicative factors in determining overall solar-electric efficiency, so large impacts in levelized cost are also observed when varying these parameters.

The analysis in this chapter ignores the fact that there are real costs associated with the infrastructure necessary to use the heat collected by a solar CHP system. In reality, technological synergies do exist between human needs and different sources of heat. For instance, houses in the United States are typically heated by forced air furnaces or radiant systems (such as radiant floors, baseboard radiators, etc.). For retrofits, radiant heating is probably more suited to integration with a DCS-CHP system than is forced-air heating because the radiant heating system operates at temperatures low enough to use the waste heat from a Rankine cycle. Also, the higher latency and use of thermal mass in radiant-type systems lends itself well to an intermittent energy supply like the sun. Forced-air systems, on the other hand, tend to have lower latency, and would also require a liquid-air heat exchanger as opposed to the more cost effective liquid-liquid heat exchanger used in radiant systems. Cooking is another area where the type of use dictates the usefulness of waste

heat. Typical stove top cooking temperatures far exceed the condensation temperature of a DCS-CHP Rankine cycle, yet some communities have successfully set up solar pressure cookers at temperatures appropriate for DCS-CHP (Weisman [41]), showing that it is possible to reconstruct the built environment to be more suited to solar thermal energy sources. Air conditioning is a different story: Typical heat-driven absorption and adsorption systems operate at temperatures low enough to use the heat from a DCS-CHP system, however price has limited small-scale application of thermally-driven cooling. As electric compressor chillers become more efficient there is also competitive pressure for heat-driven cooling systems to become more cost-effective (Norwood et al. [22]). As can be seen from these varied thermal end uses, there are some places where a DCS-CHP system would reduce the cost of auxillary infrastructure, and other places where it would increase the cost (e.g. in retrofits). This is to say nothing of the potential need for thermal storage or a non-solar back-up when operating with a DCS-CHP system, neither of which are explored here. Instead this analysis focuses on the cost of delivering a unit of solar thermal and solar electric energy from a DCS-CHP system; a discussion that is continued in Chapter 2 along with the introduction of DCS-CHP and water desalination.

In this chapter we looked at California demand and a simple model to compare average demand with expected output of a DCS-CHP system, concluding that thermal and electrical loads are well matched to system production. We then develop a methodology for sensibly disentangling the costs of electrical and heat production from a solar combined heat and power system. Using typical meteorological year solar data we compare the output of a solar Rankine CHP system with an identically sized (in terms of peak power) photovoltaic system. This shows that within a bound of plus or minus 10%, with either tracking or stationary collectors, that the average electrical cost of a solar CHP system is comparable to that of a stationary PV system in terms of "cost per watt". However, the solar Rankine CHP system will additionally provide 4 to 6 units of useful heat energy for every one unit of electricity generated whereas the typical photovoltaic system will provide no useful heat. For the purposes of research and development into solar Rankine CHP systems, peak power rating is therefore a metric that permits fair comparison of solar CHP electrical output to distributed photovoltaics of power less than 10kW. However, due to the extreme variations in weather patterns and the differential effects of these patterns on system output, site specific weather data is necessary to realistically predict and compare the levelized cost of electricity production for these two systems.

Chapter 2

Life Cycle Analysis: Economics, Global Warming Potential, and Water for Distributed Concentrating Solar Combined Heat and Power

2.1 Introduction

Ultimately, the goal of this project is to develop an energy generation system that utilizes a renewable energy source (the sun) while working towards mitigation of global climate destabilization. To ensure this goal is achieved the following three steps are necessary: (1) determine and utilize appropriate metrics for solar energy technology (2) establish and utilize methods for life-cycle assessment (LCA) of emerging technologies (3) optimize the system based on the chosen metrics and LCA results.

Many assessments of alternative energy systems have focused on the energy payback time of the system, however given the goal of mitigating climate chaos at the lowest possible cost, more appropriate metrics to use are greenhouse gas intensity and life cycle costing. Greenhouse gas intensity, indicating the units of GHG emissions produced for every unit of electricity or heat generated over the system lifetime, improves upon energy metrics that fail to appropriately acknowledge the different global warming potentials of working fluids or differences in fuel sources used during manufacturing of components. For specific sites, other LCA metrics like Greenhouse Gas Return on Investment, and the Water Availability Factor would be appropriate for assessing appropriateness of distributed concentrating solar combined heat and power (Reich-Weiser et al. [28]). The economic input-output life-cycle assessment (EIOLCA) database provided by Carnegie Mellon University can provide economic life cycle data with appropriate categorization of system component costs into EIOLCA categories (Hendrickson et al. [9]). These metrics and other environmental considerations are incorporated early in this design process, given only cost and materials estimates. As development of a particular design moves forward, more detailed process-based analysis (Pehnt [24]) can be used to understand design trade offs between environmental, performance, and economic goals. In addition to greenhouse gas emissions, water use and toxicity are assessed as decisions are made on materials and functional form.

To these ends, the first part of this chapter is devoted to LCA economics and GWP analysis of a proposed DCS-CHP system, and the latter part of this chapter explores the water use and potential for water purification/desalination using DCS-CHP. For the purposes of life cycle analysis, the problem of joint production makes it difficult to allocate the relative costs of a CHP system to electrical and heat production (Wade [40]) so costs are divided using the methodology described in Chapter 1 (Norwood et al. [23]).

2.2 Life Cycle Assessment of a single solar dish collector DCS-CHP system

Performing a life cycle assessment (LCA) is a useful way of comparing the environmental impacts of different power generation systems. Here, a life cycle assessment is completed on a single solar dish collector solar Rankine combined heat and power system using the Industry Benchmark US Department of Commerce EIO model from 1997 (Hendrickson et al. [9]). The global warming potential (GWP) per kWh of energy, the energy payback time (EPBT), the cost

per installed peak watt, and the levelized cost of electrical and thermal energy are calculated. These results show DCS-CHP generates an estimated GWP of 80 gCO2 equivalent greenhouse gases per kWh electricity, putting it below the competitive range with photovoltaics (PV), which range from 110-180 gCO_2eq/kWh according to a couple recent studies(Stoppato [34], Lenzen [14]). The EPBT for the DCS-CHP system, estimated at 27 months, makes it competitive with PV systems. The levelized cost of energy generated by the DCS-CHP system over its lifetime is estimated to be \$0.25/kWh electric, and \$0.03/kWh of 100ºC heat, or \$3.20/W electric and \$0.40/W thermal in terms of installed capital cost per peak power output. The LCA of the system affirms that small scale solar combined heat and power systems can economically compete with other renewable energy systems and have comparable environmental footprints to PV systems.

2.2.1 Assumptions of LCA

The Industry Benchmark US Department of Commerce EIO model from 1997 adjusted for inflation, with the breakdown of selected sectors shown in Figure 2.1, provides a basis for this LCA.

The RawSolar prototype collector (RawSolar [27]), with the performance parameters specified in Chapter 1 for a dish collector, provides an estimate of collector efficiency. Using the data for the Katrix rotary lobe expander from Chapter 3, and NREL typical meteorological year solar insolation data for Oakland, CA along with the collector efficiency, we run the DCS-CHP modeling software parameterized as described in Chapter 4. Working from a cost estimate from RawSolar complete with bids for materials and labor (for installing the concentrating solar thermal system in Richmond, CA) we add the necessary components for electricity generation to come up with a final system cost as broken down in Table 2.1. Costs are divided between electrical and heat generation according to the methodology described in Chapter 1. The simplified levelized energy cost LEC assuming fixed yearly operation and maintenance costs M over the lifetime of 25 years n, a 7% interest rate r, the initial capital costs I, and total energy produced per year E is (Appropedia [2]):

$$LEC = \frac{I \left(\frac{r}{1-(1+r)^{-n}} \right) + M}{E} \tag{2.1}$$

2.2.2 LCA of economics and GWP results

The DCS-CHP system is estimated to produce ~80 gCO_2eq/kWh of electricity and ~10 gCO_2eq/kWh thermal assuming the 1997 mix of fuels reported in the US EIO database. This is much less than fossil fuel based power generation methods, which produce hundreds of gCO_2eq/kWh. In comparison to renewable energy technologies, according to Lenzen, the DCS-CHP system GWP is higher than that of wind turbines (21 gCO_2eq/kWh) and hydroelectricity (15 gCO_2eq/kWh) but lower than photovoltaics (106 gCO_2eq/kWh) (Lenzen [14]). Overall, the GWP contribution of the DCS-CHP system was split evenly between the dish

Dish Components	Estimated price in 2009 $US	Sector / References in EIO LCA database	GWP / Component
Mirror	$ 254	333314 Optical Instrument and Lens Manufacturing	82363
Structure	$ 465		
Aluminum (Tubing/Rod)	$ 200	331315 Aluminum Sheet, Plate, and Foil Manufacturing	296684
Steel	$ 170	331111 Iron and Steel Mills	348492
Misc (nuts. bolts. etc.)	$ 35	332722 Bolt, Nut, Screw, Rivet, and Washer Manufacturing	14689
Paint	$ 60	325510 Paint and Coating Manufacturing	52777
Tracking and Sensing	$ 180		
Motors/Actuators	$ 130	335312 Motor and Generator Manufacturing	62893
Circuit Board	$ 35	334412 Bare Printed Circuit Board Manufacturing	12706
Sensor Eyes	$ 15	334513 Industrial process variable instruments	3735
Receiver Piping	$ 60		
Receiver Coating	$ 5	332812 Metal Coating, Engraving (except Jewelry and Silverware)	3914
Steel Coil and Pipe	$ 25	331210 Iron and Steel Pipe and Tube Manufacturing from Purchased Steel	25159
Insulation	$ 30	3261A0 Foam product manufacturing	21088
Manufacturing Labor	$ 200	weighted value	132299
Miscellaneous Parts	$ 100	33291 Metal Valve Manufacturing	39434
Installation, labor/material	$ 1,000	235110 Plumbing, Heating, and Air-Conditioning Contractors / 234910 Water, Sewer, and Pipeline Construction / 235610 Roofing, Siding, and Sheet Metal Contractors	521806
Maintenance	$ 2,500	230340 Other maintenance and repair construction	1530011
Total	**$ 4,759**		**3148048**

(a) Cost estimates, sector references, and associated GWP (gCO2 equivalent) based on EIO-LCA for the RawSolar concentrating dish components

Other System Components	Estimated price in 2009 $US	Sector / References in EIO LCA database	GWP / Component
Structure	$ 65		
Misc (nuts. bolts. etc.)	$ 35	332722 Bolt, Nut, Screw, Rivet, and Washer Manufacturing	14689
Paint	$ 30	325510 Paint and Coating Manufacturing	26388
System component	$ 1,740		
Pump	$ 150	333911: Pump and pumping equipment manufacturing	62729
Turbine	$ 990	333611: Turbine and turbine generator set units manufacturing	390497
Alternator	$ 100	335312: Motor and generator manufacturing	47932
Heat Exchanger	$ 500	332410: Power boiler and heat exchanger manufacturing	260530
Controllers	$ 100		
Pump controller	$ 100	333911: Pump and pumping equipment manufacturing	41819
Piping	$ 150		
Steel Coil and Pipe	$ 100	331210 Iron and Steel Pipe and Tube Manufacturing from Purchased Steel	100634
Insulation	$ 50	3261A0 Foam product manufacturing	35147
Miscellaneous Parts	$ 100	33291 Metal Valve Manufacturing	39434
Installation, labor/material	$ 2,000	235110 Plumbing, Heating, and Air-Conditioning Contractors / 234910 Water, Sewer, and Pipeline Construction / 235610 Roofing, Siding, and Sheet Metal Contractors	1043613
Maintenance	$ 5,000	235110 Plumbing, Heating, and Air-Conditioning Contractors / 234910 Water, Sewer, and Pipeline Construction / 235610 Roofing, Siding, and Sheet Metal Contractors	3060021
Total	**$ 9,155**		**5123433**

(b) Cost estimates, sector references, and associated GWP (gCO2 equivalent) based on EIO-LCA for the other system components

Table 2.1: Cost estimates and EIO-LCA data for DCS-CHP system

components and the Rankine cycle components. Most of the GWP contribution comes from maintenance of the dish and Rankine cycle components as seen in Figure 2.1a. Considering the GWP of only the initial components, Figure 2.1b shows that the dish structure and the Rankine expander contribute the majority of the GWP.

This analysis predicts a single dish collector system with peak capacity of ~1kW electric would produce electricity for $3.20/W capital cost and a levelized cost of electricity of $0.25/kWh. Local electricity rates in the San Francisco Bay Area are about $0.14/kWh, but in the author's experience, many larger households pay more for electricity because of increasing block tariffs. The DCS-CHP system is additionally expected to produce useful heat energy with a peak capacity of ~5kW (80% waste-heat recovery factor) for a capital cost of $0.40/W or levelized cost of $0.03/kWh. Energy Payback Time (EPBT) for our system, including both electricity and heat production, is expected to be 27 months.

2.3 Water and solar energy

The ties between water and solar energy are inextricable. The sun drives the giant distillation process called the hydrological cycle. The energy from sunlight evaporates water, 97% of which is saline, covering three-quarters of the earth's surface, and transforms it into fresh water vapor, condenses it in the atmosphere in the form of clouds, transports it via wind, and delivers much of it to the land as rain where it fills our rivers, lakes and aquifers. Humans often replicate this cycle, which has been occurring endlessly for eons, albeit on a more modest scale. As early as 400 BC Aristotle wrote of distilling impure water to create potable water (Kalogirou [13]). More recently, humans have tapped the power of sunlight to create electricity, through a variety of processes including photovoltaic, and thermodynamic cycles named Brayton, Ericsson, Rankine, and Stirling. These cycles are the means by which nearly all electricity on the planet is produced, and their predominant energy source is the combustion of fossil fuels. The same heat engines that convert thermal energy to electricity in a natural gas, coal or nuclear power plant can instead harness solar energy as the fuel. The need undoubtedly exists to transition away from a predominantly fossil fuel driven society, and there is urgency in the 'developing' world to move in the direction that this name implies. The question remains: will that development path allow us to stabilize at the imperative 350 ppm carbon dioxide in the atmosphere outlined by Hansen (Hansen et al. [8])?

Compounding the problem is that approx. 0.9 billion people lack access to safe drinking water, and 2.6 billion lack basic sanitation (WHO and UNICEF [43]). This is another area where solar energy and water exhibit synergy. Because all thermodynamic cycles must have a means of rejecting heat to a lower temperature sink, there is much thermal energy to be dissipated in concentrating solar power plants. Because these facilities are usually large and located far from an area where the heat could be used, this heat is usually dissipated into a body of water or, in cases where there is a scarcity of water, into the air. If instead these facilities were small and distributed so that they could be located near the demand for energy and potable water, in populated areas, then the otherwise wasted heat could also be used for the purpose of desalination
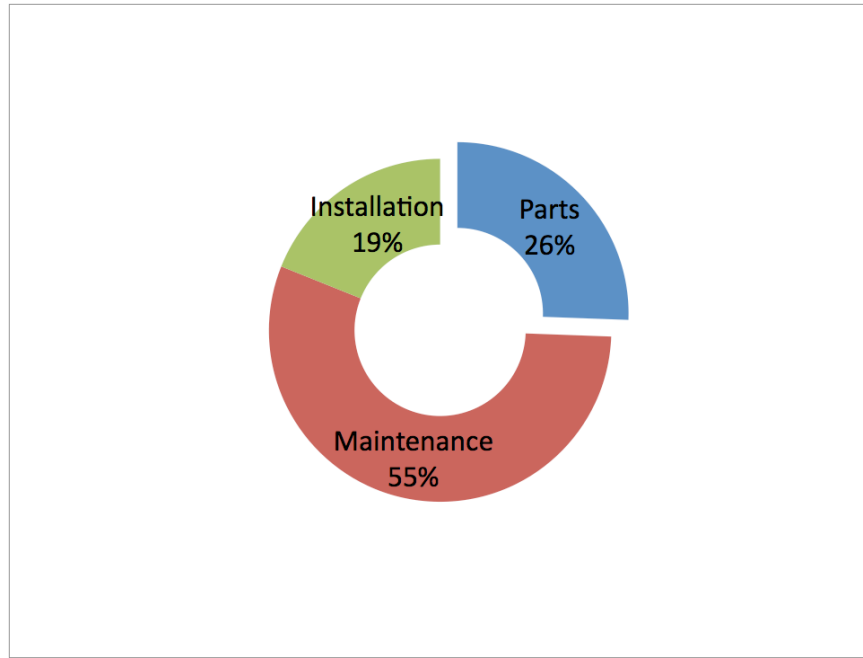
(a) Percentage of GWP attributed to i) components (parts cost expanded in sub-figure b), ii) initial installation, and iii) maintenance over lifetime
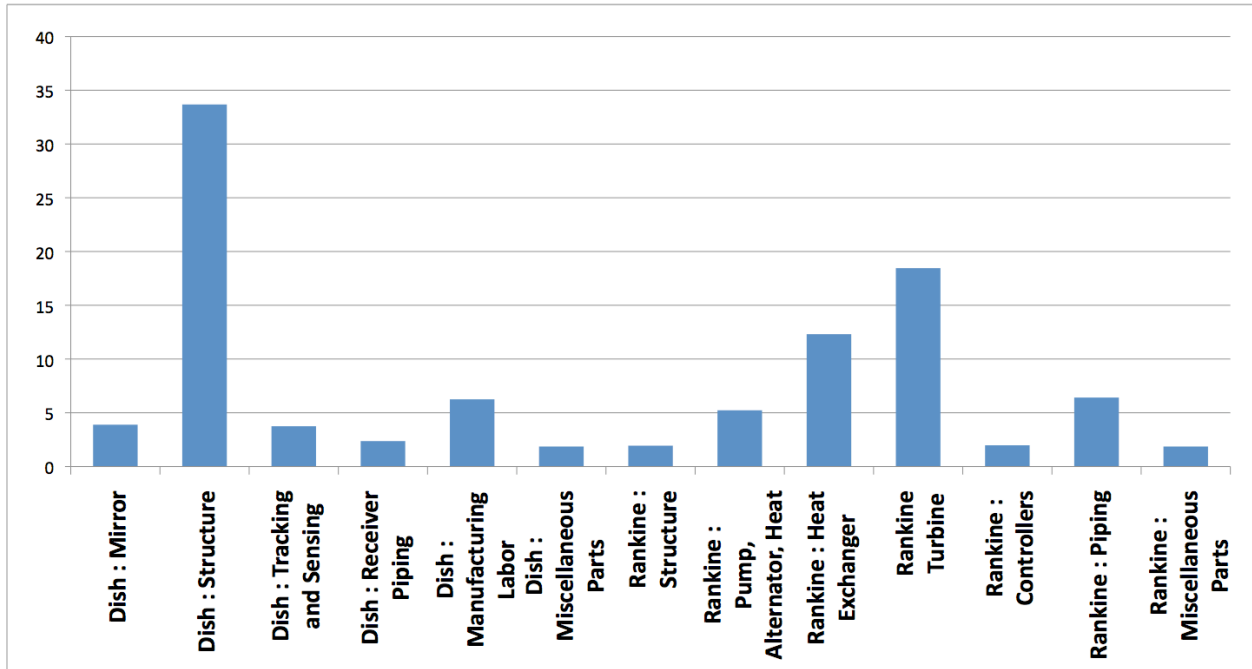
(b) Percentage of GWP attributed to each component in the DCS-CHP system, not including installation

Figure 2.1: Global Warming Potential over lifetime of DCS-CHP system, based on EIO-LCA analysis

or purifying water through a distillation process. Not only that, but rejected heat could be used for cooking, space heating, domestic hot water, etc. This would decrease the cost of electricity generation by providing cooling to the heat engine while, at the same time, producing another valuable co-product, potable water, from this distributed concentrating solar combined heat and power (DCS-CHP) system.

2.3.1 Background of solar-water nexus

Dublin Principle number 4, the last principle in the Dublin Statement on Water and Sustainable Development arising out of the 1992 Earth Summit, states:

> Water has an economic value in all its competing uses and should be recognized as an economic good. Within this principle, it is vital to recognize first the basic right of all human beings to have access to clean water and sanitation at an affordable price. Past failure to recognize the economic value of water has led to wasteful and environmentally damaging uses of the resource. Managing water as an economic good is an important way of achieving efficient and equitable use, and of encouraging conservation and protection of water resources.

So, given that water has an economic value, and it is inextricably tied to solar energy, what is the value of potable water in the developing world and what would be the cost of producing water as a byproduct of DCS-CHP described above? In answer to the first part of that question, figure 2.2 shows that water ranges from a cent to over ten dollars per cubic meter in selected developing countries depending on whether the water is provided through the water utility (generally inexpensive) or the informal private sector (more expensive).

To answer the second part of that question, in the next section we delve into the details of solar desalination in an effort to estimate its cost in this application. Finally, to complete the water and DCS-CHP story we consider the consumptive use of water in the electricity generation subsystem, and review available cooling methods through an analysis of current solar power plants.

2.3.2 Solar desalination and purification

Of the 3% of water on the planet that is fresh water, only 1/1000 of that is produced from desalination plants. Desalination systems are many and varied, however, numbering over 13000 worldwide, most in the U.S. and Middle East (Gleick [7], El-Dessouky et al. [6]). There are many types of desalination systems, as seen in figure 2.3, which are generally divided into two categories: membrane systems and phase-change systems. Of the membrane systems, reverse osmosis (RO) garners the most worldwide popularity, and multiple stage flash (MSF) distillation is the most common of the phase change processes followed by multiple effect boiling (MEB). Solar stills have historically been a popular system on the village and small scale, and are usually single-stage distillation where the energy from the evaporated water is typically not recovered

City	Cost of water for domestic use (a)(house connection: 10 m³/month) in US$/m³	Price charged by informal vendors (b) in US$/m³	Ratio (b/a)
Vientiane (Lao PDR)	0.11	14.68	135.92
Male* (Maldives)	5.70	14.44	2.53
Mandalay (Myanmar)	0.81	11.33	14.00
Faisalabad (Pakistan)	0.11	7.38	68.33
Bandung (Indonesia)	0.12	6.05	50.00
Delhi* (India)	0.01	4.89	489.00
Manila (Philippines)	0.11	4.74	42.32
Cebu (Philippines)	0.33	4.17	12.75
Davao* (Philippines)	0.19	3.79	19.95
Chonburi* (Thailand)	0.25	2.43	9.57
Phnom Penh (Cambodia)	0.09	1.64	18.02
Bangkok* (Thailand)	0.16	1.62	10.00
Ulaanbaatar (Mongolia)	0.04	1.51	35.12
Hanoi (Viet Nam)	0.11	1.44	13.33
Mumbai* (India)	0.03	1.12	40.00
Ho Chi Minh City (Viet Nam)	0.12	1.08	9.23
Chiangmai* (Thailand)	0.15	1.01	6.64
Karachi (Pakistan)	0.14	0.81	5.74
Lae* (Papua New Guinea)	0.29	0.54	1.85
Chittagong* (India)	0.09	0.50	5.68
Dhaka (Bangladesh)	0.08	0.42	5.12
Jakarta (Indonesia)	0.16	0.31	1.97
Colombo* (Sri Lanka)	0.02	0.10	4.35

* Some water vending, but not common.

Figure 2.2: House connection prices versus informal vendor prices for water (in US$) in selected developing countries (UNESCO [38])

Phase-change processes	Membrane processes
1. Multi-stage flash (MSF)	1. Reverse osmosis (RO)
2. Multiple effect boiling (MEB)	–RO without energy recovery
3. Vapour compression (VC)	–RO with energy recovery (ER-RO)
4. Freezing	2. Electrodialysis (ED)
5. Humidification/ dehumidification	
6. Solar stills	
–Conventional stills	
–Special stills	
–Cascaded type solar stills	
–Wick-type stills	
–Multiple-wick-type stills	

Figure 2.3: Desalination processes (Kalogirou [13])

thus leading to lower overall system efficiency. MSF systems tend to be larger (on the scale of 1000 to 100,000 m^3/day), but MEB systems have been designed in rugged varieties suitable to deployment in small villages under less controlled and less skilled operation (Thomas [37], Kalogirou [11]).

Looking at the energy required for each type of plant can help guide the selection of the technologically and economically optimum desalination system to run off the waste heat of a distributed concentrating solar combined heat and power system (DCS-CHP). Figure 2.4 shows the required energy for different desalination systems.

It is interesting to note that membrane systems consume the least energy, yet all that energy must be mechanical work, making them an inappropriate technology to use with a system like DCS-CHP where thermal energy is abundant and thermal to electrical/mechanical energy conversion efficiency is low. The fact that the most abundant energy available from a DCS-CHP system is moderate grade heat (at around 370K), rules out the use of vapor compression, reverse osmosis, and electrodialysis as the optimum choice for desalination. Of the remaining choices, it is important to look at the method of operation of the system to further narrow down the selection. Kalogirou has published several papers on the selection of optimal desalination systems for solar (Kalogirou [13, 11]). He concludes that the MEB process with a multiple effect stacked (MES) evaporator is the most appropriate for solar, a schematic of which is shown in figure 2.5.

An MES with a DCS-CHP system would function like this:

1. Low pressure steam (generated from the condenser of the Rankine cycle) will enter into a tube array in the 1st effect as the feed-water is sprayed down from above.

2. The steam will condense while causing the feed-water (at lower pressure) to evaporate on the outside of the tubes. The condensate that forms inside the tubes will become part of the

Process	Heat input (kJ/kg of product)	Mechanical power input (kW h/m³ of product)	Prime energy consumption (kJ/kg of product)[a]
MSF	294	2.5–4 (3.7)[b]	338.4
MEB	123	2.2	149.4
VC	–	8–16 (16)	192
RO	–	5–13 (10)	120
ER-RO	–	4–6 (5)	60
ED	–	12	144
Solar still	2330	0.3	2333.6

[a] Assumed conversion efficiency of electricity generation of 30%.
[b] Figure used for the prime energy consumption estimation shown in last column.

(a) Energy consumption of desalination system (Kalogirou [13])
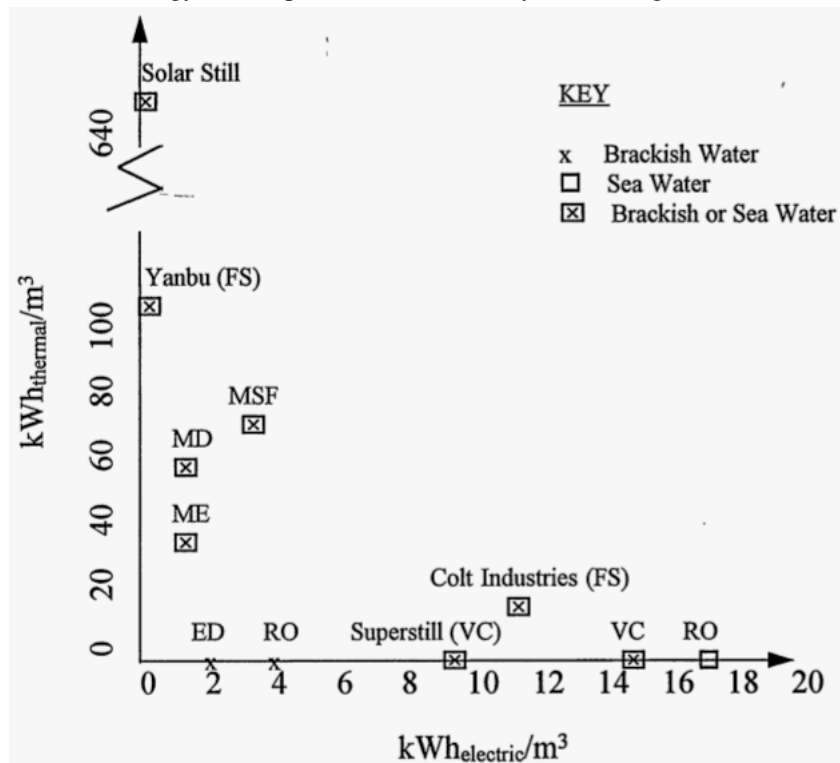
(b) Thermal vs. electrical energy demands: FS is freeze separation, ME is multiple effect boiling (Thomas [37])

Figure 2.4: Energy comparison of desalination systems
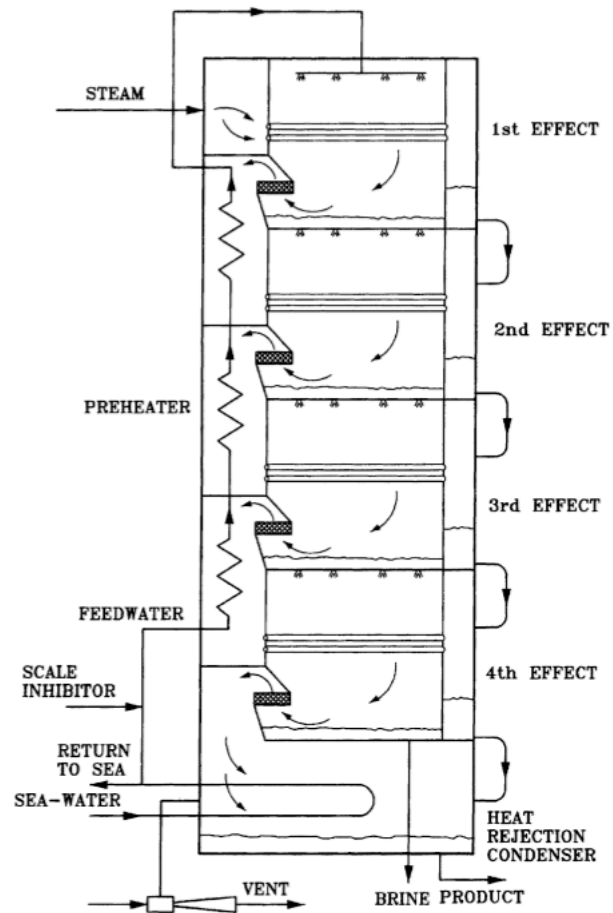
Figure 2.5: Schematic of MES evaporator (Kalogirou [13])

product water while the evaporate from the outside of the tubes will flow into the next effect.

3. The feed-water that doesn't evaporate drips down into a pool in the first effect and goes through a nozzle dropping the pressure and falling onto the tubes of the 2nd effect where the steam inside the tubes (the evaporate from the first effect) again causes vaporization of the now slightly more saturated feed-water solution.

4. This effect continues and at each stage the condensate coming from the tubes becomes part of the product until the last stage where the unheated feed-water loop condenses the last evaporate to add to the final product while the brine from the last stage is removed.

5. At the same time steps 1-4 are occurring the feed-water is being heated sequentially, as it is piped up from the 4th effect to the 1st, gradually warming as it goes until it is sprayed onto the tubes of the 1st effect as described in step 1.

The choice of a MEB distillation system is synergistic with the DCS-CHP concept because the temperatures needed for a MEB are in the 340-370K range, which exactly matches the condensation temperature for the steam Rankine system. Because MEB is an indirect solar distillation process (i.e. the sunlight would not be directly evaporating the water to be purified) the condenser will effectively act to transfer energy from the condensing working fluid of the Rankine subsystem to the feed-water of the desalination/purification system as illustrated in the system schematic of figure 2.6.

Kalogirou surveyed dozens of solar MEB systems installed worldwide (results shown in figure 2.7) and concluded the following benefits of MEB systems for solar desalination:

- Like any boiling process, MEB inherently removes salinity, manganese, fluoride, heavy metals, microbiological contamination and pesticide/herbicide residues.

- MEB is the cheapest of all indirect collection systems (See figure 2.7).

- MEB is robust in that it does not require highly trained operators to keep it running safely. There are no complicated additives to use, nor, as in RO, can misoperation cause damage to the membrane allowing contaminated water to be passed through.

- MEB is stable for varying energy supply from 0 to 100% of capacity, so it is uniquely suited for fluctuating solar insolation levels.

- Very small amounts of descaling agent can be used in seawater desalination as the system is effectively a once-through process, and the feed-water is at its lowest impurity concentrations a the highest temperature.

- The total cost of MEB with solar thermal is less than RO with photovoltaics because of the high cost of photovoltaic electricity.

- Improved energy efficiency is possible because the brine is not heated above its boiling point, leading to less irreversibility (i.e. less entropy generation).
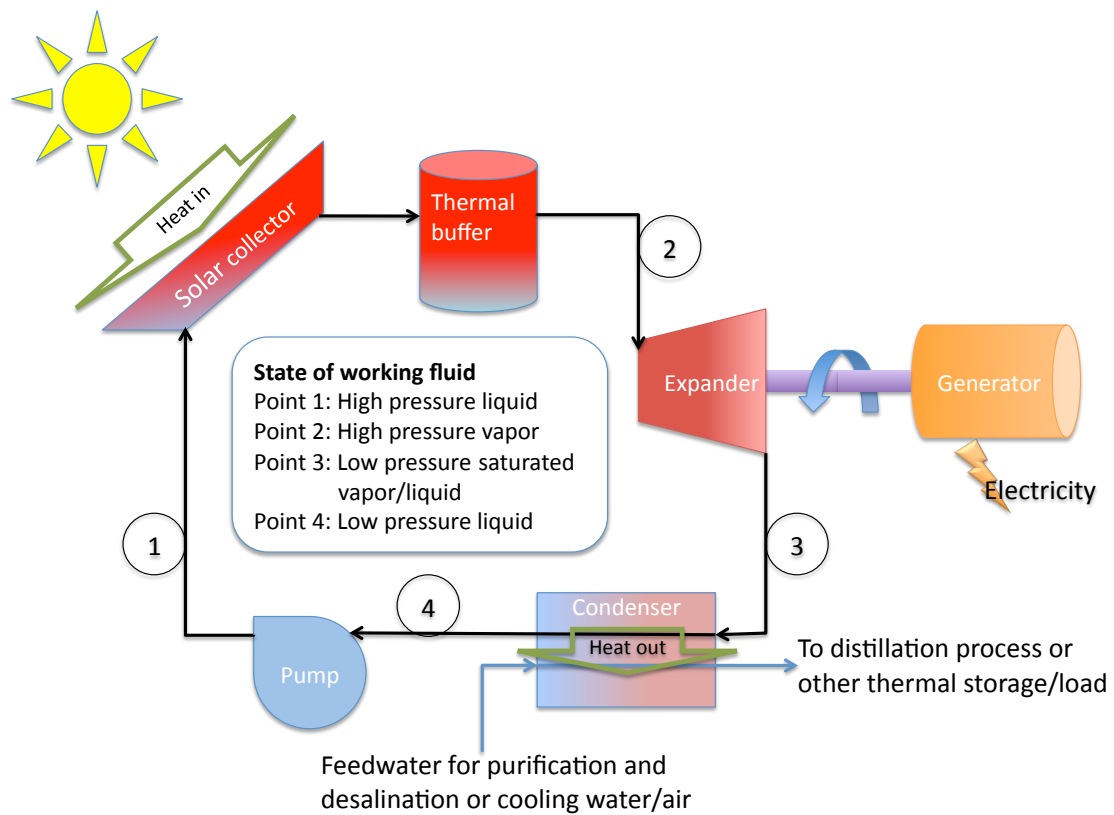
Figure 2.6: Distributed concentrating solar combined heat and power with desalination

Item	MSF	MEB	VC	RO	Solar still
Scale of application	Medium–large	Small–medium	Small	Small–large	Small
Seawater treatment	Scale inhibitor anti-foam chemical	Scale inhibitor	Scale inhibitor	Sterilizer coagulant acid deoxidiser	–
Equipment price (Euro/m^3)	950–1900	900–1700	1500–2500	900–2500 membrane replacement every 4–5 yr	800–1000

Low figures in equipment price refer to bigger size in the range indicated and vice versa.

Figure 2.7: Comparison of desalination plants; price is reported in capacity per day (Kalogirou [13])

- There is low electrical demand compared to other desalination technologies: No high pressure pumping losses as in RO, no MSF recirculation pumps, nor vapor compression, etc (see figure 2.4).

- Plant simplicity is promoted because fewer effects are needed for a given performance ratio.

Perhaps most importantly to the DCS-CHP desalination concept, Kalogirou agrees with Thomas in concluding that MEB is better suited for small applications than the other indirect solar distillation techniques (Kalogirou [13], Thomas [37]).

2.3.3   Utilization of water in power system operation

In addition to the potential benefit of potable water as a co-product, a DCS-CHP system consumes water in cleaning the concentrating collectors, for make-up water to replace water lost due to leaks, and in some cases for water cooling. To fully understand the relationship between water and solar energy this water needs to be considered. Figure 2.8 shows the relative consumptive use of various power plant technologies. For a DCS-CHP system we assume water use comparable to a parabolic trough with air cooling since the optimal high temperature of the working fluid in parabolic trough collectors is in the right range, 500K, (Kalogirou [12]) and the thermal load effectively acts as a water cooling loop without the water consumption.

In the case when there is no desalination or thermal loads to dissipate heat from the condenser an air cooling system is shown to have just a 2-9% cost penalty, but water consumption of just 0.3 m^3/MWh as compared to recirculating water cooling of 3 m^3/MWh (USDOE [39]). Of course, operating a DCS-CHP system with air or water cooling implies that there is not sufficient thermal load to absorb the energy rejected from the electric power generation subsystem. This in turn would lead to a higher cost of electric generation, and would decrease the economic value of the system. The least expensive energy produced by these small scale concentrating solar systems is indeed thermal energy. There is no question, as compared to coal, nuclear, and natural gas, that even water-cooled concentrating solar power water consumption is on par with the best available technologies in the electric power sector.

Technology	Cooling	Gallons MWhr	Perform. Penalty*	Cost Penalty**	Reference
Coal / Nuclear	Once-Through	23,000 – 27,000***			1, 3
	Recirculating	400 - 750			1, 3
	Air Cooling	50 - 65			1, 3
Natural Gas	Recirculating	200			4
Power Tower	Recirculating	500 - 750			(estm.)
	Combination Hybrid Parallel	90-250	1-3%	5%	10, 11
	Air Cooling	90	1.3%		9
Parabolic Trough	Recirculating	800			5
	Combination Hybrid Parallel	100-450	1-4%	8%	7, Appx. A
	Air Cooling	78	4.5-5%	2-9%	6, 9
Dish / Engine	Mirror Washing	20			5
Fresnel	Recirculating	1000			(estm.)

Figure 2.8: Comparison of consumptive use of various power plant technologies using various cooling methods: * - Annual energy output loss is relative to the most efficient cooling technique. ** - Added cost to produce the electricity. *** - Majority of this amount is returned to the source but at an elevated temperature. (USDOE [39])

2.3.4 Solar desalination economics

Thomas reviewed the costs of various desalination systems for the village scale and states that solar thermal MEB has a levelized cost of $0.70-$4.00/m^3 with the low end referenced to a capital cost of $1000/m^3 of capacity on a daily basis (Thomas [37]). We would expect system cost to be in this range for a DCS-CHP system where the solar field cost is split between the electrical generation and the solar thermal generation as described by Norwood et al. (Norwood et al. [23]). With a predicted levelized solar thermal cost of $0.03/kWh, this leads to a limiting estimate of the cost of a solar still at $21/m^3 (based on the thermodynamic minimum energy, 2800 J/g, to evaporate water from ambient temperature). Since the multiple effect evaporator has about 1/15th the energy use of a solar still we would predict a cost of $1.40/m^3 for an indirect solar MEB as described in this paper. El-Dessouky cites the cost of a low-temperature MEB at $0.45/m^3 from fossil fuel sources, or about one third the predicted cost from DCS-CHP with desalination of $1.40/m^3. This is at the high end of the household cost of water for selected Asian developing countries as presented in figure 2.2, and is competitive with the informal sector for about half of those countries.

2.4 Conclusions

The life cycle analysis presented in the first part of this chapter affirms that a solar Rankine CHP system can be cost effective and directly competitive with other fossil and renewable energy production methods in small scale. The cost and environmental benefits of this system could be improved by further refinements in both trough and dish collector systems, and by continued development of a low-cost expander like the Katrix rotary lobe expander for use with steam as the working fluid. LCA economics of this specific DCS-CHP system agree well with the generic case study of Chapter 1. The results presented here predict levelized costs of $0.25/kWh electricity and $0.03/kWh thermal, for a system with a life-cycle global warming potential of ~80 gCO$_2$eq/kWh of electricity and ~10 gCO$_2$eq/kWh thermal.

Based on the reasonable economics shown for air-cooling, and the fact that any combined heat and power system reduces the need for cooling while at the same time boosting the overall solar efficiency of the system, DCS-CHP does rate among the best electric power generation systems in terms of minimization of water use in the maintenance and operation of the plant. Additionally, the LCA of the embodied water in the manufacture of a concentrating solar system, which uses primarily common metals and glass in simple manufacturing processes, promises to be insignificant, (on the order of 0.03 m^3/MWh) even as compared to the modest water use in operation (Montgomery [19]) .

The outlook for water desalination coupled with distributed concentrating solar combined heat and power is another story. Based on the economics described in the last section, water desalination with DCS-CHP would be economical and practical only in areas where water is very scarce or moderately expensive, primarily available through the informal sector, and where contaminated, or salt water is easily available as feed-water. Additionally, the cost of fossil fuels

would have to be greater than DCS-CHP solar energy for the economics to favor solar desalination in the first place. It is also interesting to note that $0.40-$1.90/m^3 is the range of water prices in the developed world (UNESCO [38]), so DCS-CHP desalination systems, at a predicted cost $1.40/m^3, would be an economical solution there under some conditions. Of course, in most developed countries the cost effective option to meet water scarcity problems is to increase water end-use efficiency and forgo energy-intensive supply side augmentation such as desalination altogether.

Chapter 3

Testing of the Katrix Rotary Lobe Expander
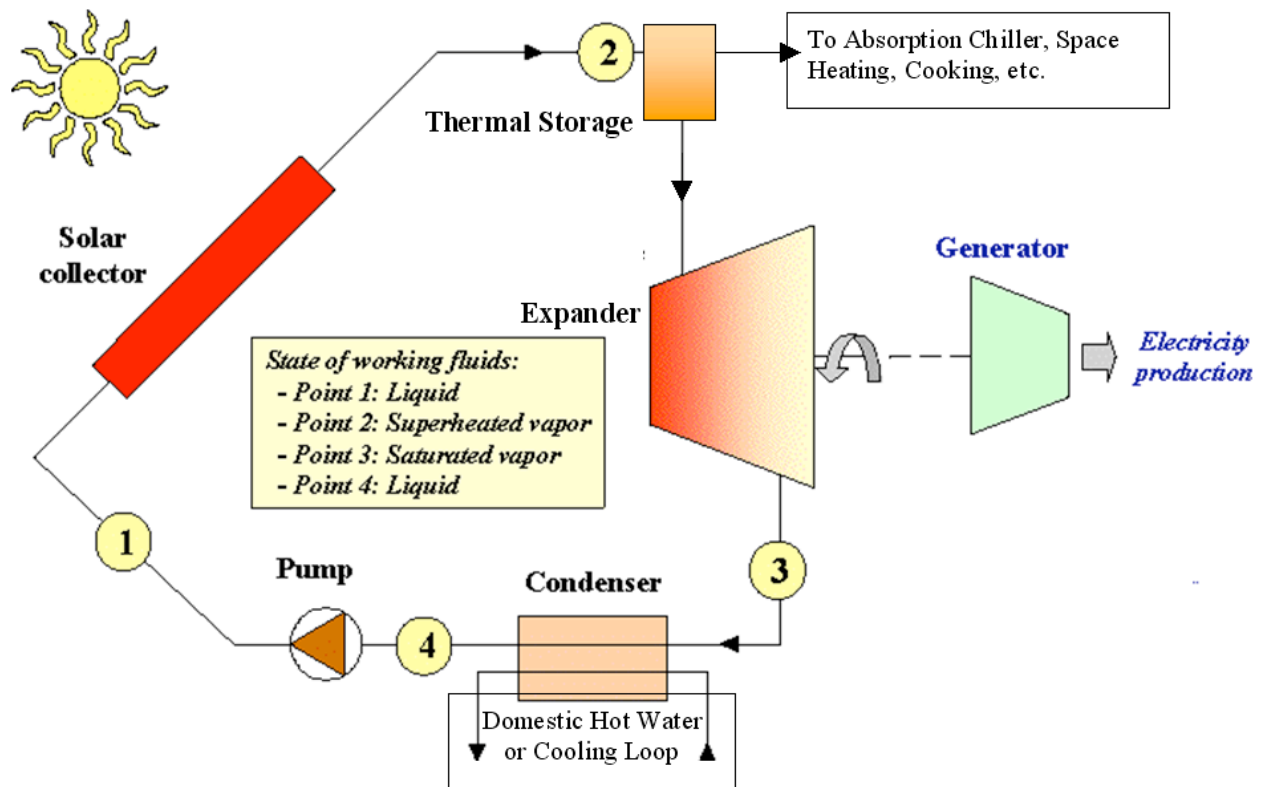
Figure 3.1: A solar Rankine CHP system.

3.1 Introduction

The purpose of this research is the analysis and development of a small-scale solar system that would compete with available distributed technologies for heat and electricity generation. In developing such a system we focus on the small-scale expander because no suitable product has yet been commercialized. Figure 3.1 is a diagram of a solar CHP system that uses a Rankine cycle with the following characteristics. Water (or another working fluid), is pumped to high pressure (~1000 kPa), heated in a concentrating solar collector to greater than 473K, then expanded producing work on a shaft which is attached to a generator. The cooled fluid exits the expander and is condensed back to its original state. Ideally, the cold reservoir, to which the working fluid dumps energy, is some useful thermal load, hence completing the combined heat and power Rankine cycle.

The test system consists of a compressed air expander (a prototype that was loaned to us by Katrix, Inc. of Australia) connected to an inductive motor driven by a variable frequency drive (VFD) enabling expander testing at varying shaft speeds. This chapter describes the results of the expander testing and the relevant technical and policy issues of using an inductive generator to

45

regenerate electricity on UC Berkeley campus. I describe the test procedure, discuss grid harmonic analysis of my test setup (per IEEE 519), and describe the Pacific Gas and Electric Rule 21 policy issues to small inductive motor renewable technology. I conclude that small inductive motor power generators are not, at this time, allowable on PG&E's grid without going through rigorous, costly, and time consuming certification and engineering reviews according to Rule 21. Although harmonic distortion is within required limits and, being powered by an electric compressor, this test setup produces no net electrical energy, I nonetheless dissipate the regenerated electric energy to a bank of dynamic braking resistors to satisfy the campus EH&S and physical plant engineers' requirements of compliance with Rule 21. Results of the expander testing are a qualified success. Although the expander does not complete testing due to an internal failure, the isentropic efficiency (80-95%) and pressure ratio (6-11) at the tested speeds is impressive for a device this small and simple. Future refinements could lead to a new class of expanders with unequaled low-cost and high-performance for use in solar combined heat and power.
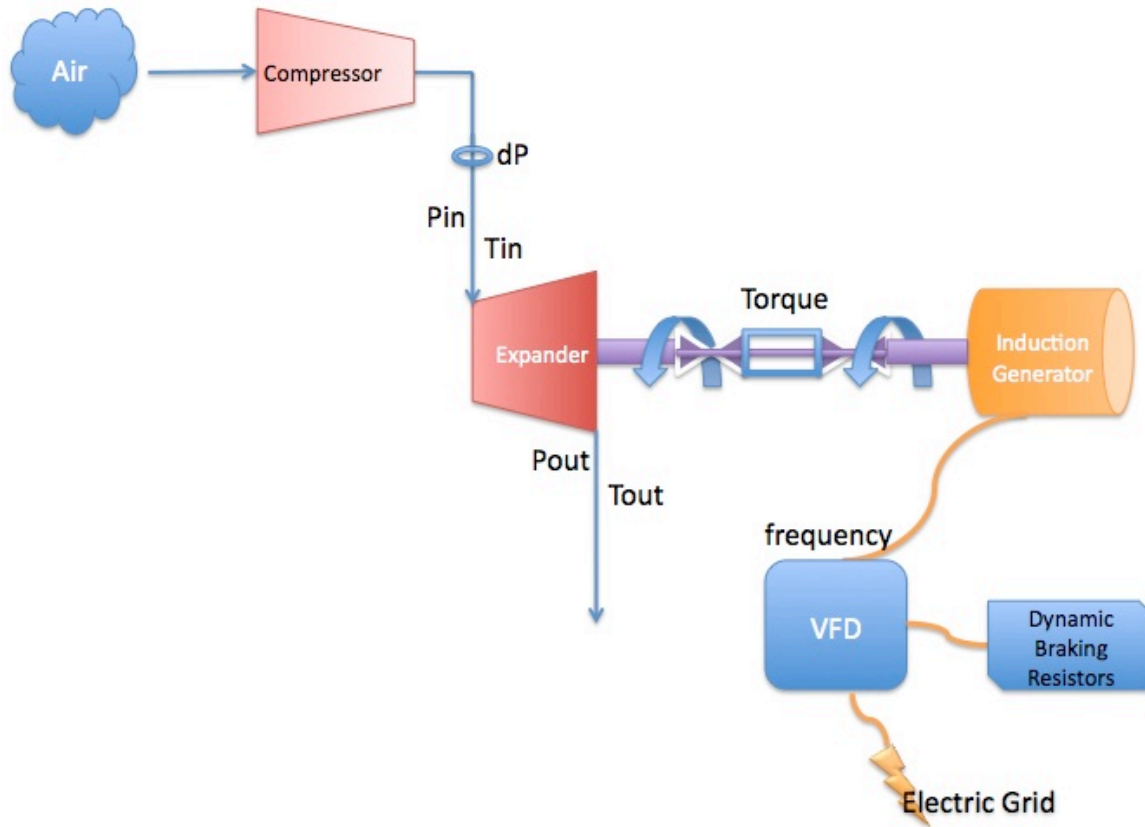
Figure 3.2: Simplified expander test setup schematic: Collected measurements are pressure across the orifice plate (dP), pressure at inlet of expander (Pin), temperature at inlet (Tin), pressure at outlet (Pout), temperature at outlet (Tout), torque, and frequency set point of the variable frequency drive

3.2   Test setup for a Katrix rotary lobe expander

The Australian company Katrix, Inc. contacted us last year asking us to test their newest prototype expander for use in a solar CHP system. Initially, our intent was to characterize the expander efficiency with air and steam as the working fluid, but due to time constraints, expense limitations, and problems with the current prototype, we did not complete the steam testing. This chapter describes results of partial completion of testing of the Katrix expander with air, at varying angular velocity. The final test system consists of the following main components:

- A compressor with booster pump producing greater than 1000 kPa absolute pressure gas,

- the Katrix rotary lobe expander,
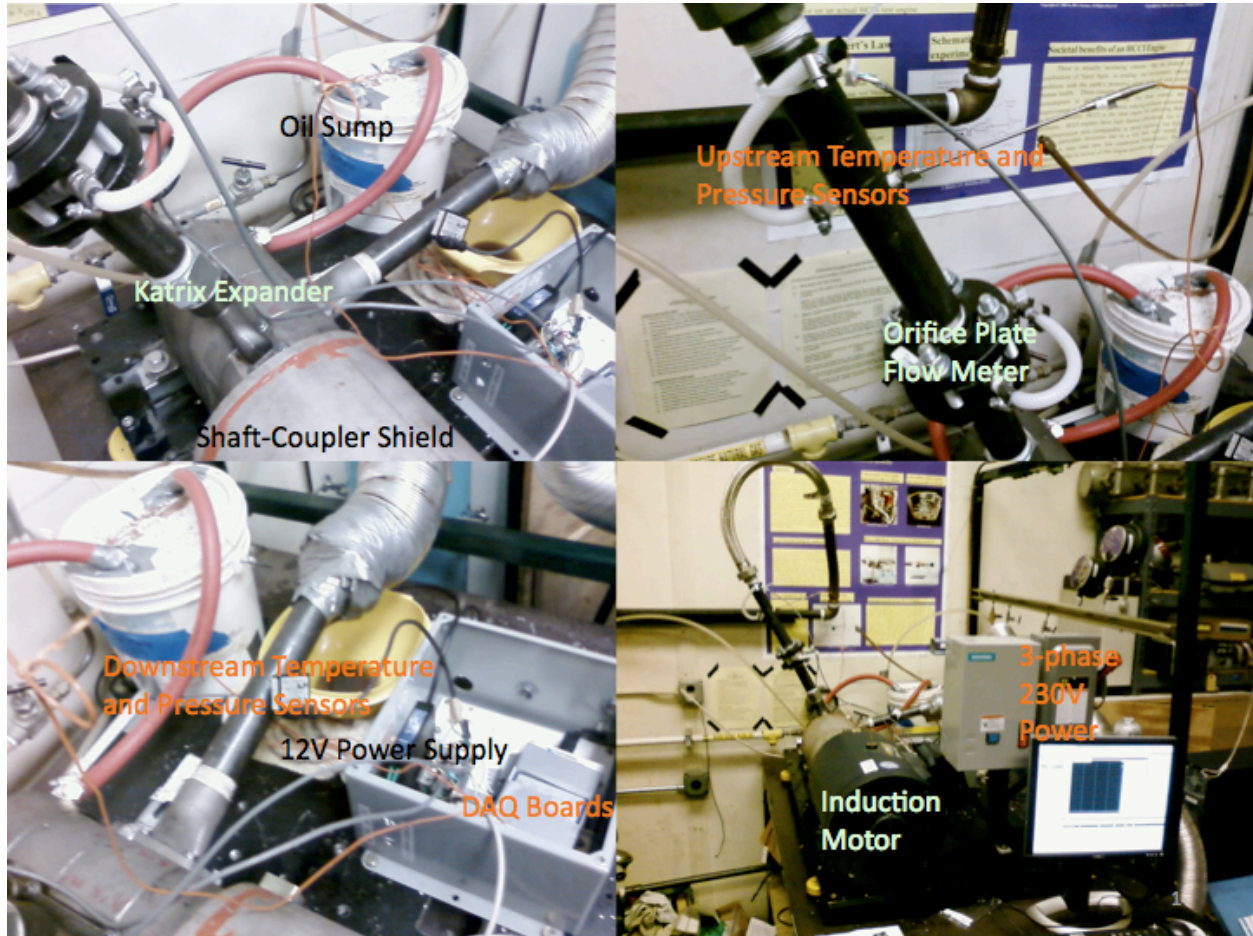
Figure 3.3: Actual test setup as installed in Hesse Hall

- upstream and downstream pressure and temperature probes (used to calculate enthalpy change of the working fluid),

- an in-line shaft torque measurement device,

- an upstream orifice plate flow meter with differential pressure sensor and a rotameter of known calibration (used to calculate flow rate),

- and a variable frequency drive with dynamic braking resistor pack providing load to the expander.

Figure 3.2 shows a simplified schematic of the test setup with relevant data measurement points, and figure 3.3 shows actual pictures of the test equipment in the basement of Hesse Hall on the UC Berkeley campus. Appendix A also contains a list of all equipment used in the testing, including the VFD, which is not shown in the pictures.

Experiments follow this operating procedure:

1. Turn on the VFD to the desired frequency set point (in this case 10-60 Hz AC, which corresponds to 31-188 rad/sec or 300-1800 rpm) so the electric motor spins the expander up to the desired angular velocity.

2. Turn on the compressed air supply so the expander powers the shaft to the electric motor and any excess regenerated electrical power is dissipated in a resistor bank connected to the VFD.

3. After the system runs for 10-15 minutes to "warm up" (i.e. reach steady state temperature at expander inlet and outlet) start data acquisition on the upstream and downstream pressure and temperature of the working fluid, torque on the shaft, and differential pressure across the orifice plate flow meter.

4. After a 10-15 minute data collection period, stop data acquisition and increase the VFD frequency set point by 5Hz.

5. Repeat steps 3 and 4 until the VFD frequency reaches 60Hz (the limits of the VFD and motor) being sure to wait for steady state operation before doing data acquisition at each speed.

6. Shut off the compressed air and turn off the VFD, in that order.

7. Find a 300 second period of recorded data with fairly steady characteristics of upstream pressure and temperature and calculate isentropic efficiency of the expander.

Matlab and Engineering Equation Solver software is used for post-processing of the experimental data. Using the two independent state variables of measured temperature and pressure, fluid inlet and outlet states can be fully determined. The specific enthalpy drop of the working fluid across

the expander multiplied by the mass flow rate (from the orifice plate flow meter) yields the drop in working fluid enthalpy. Work is simply torque multiplied by angular velocity of the shaft. Dividing total work output by the enthalpy drop in the working fluid yields the efficiency of the expander over the data collection period. This data is used to map out the device efficiency over a range of rotational frequencies. Appendix B shows the full Matlab code for data processing.

3.3   Harmonic analysis, regulations for distributed generation

The intent of any solar power device is the capture of sunlight to generate power onto an electric grid. Whereas the sun would be heating the working fluid in a solar application, in this testing the power source is the electric air compressor. Also, for the purposes of the test, the induction generator and variable frequency drive (VFD) act as the load. Any electrical power generated by the test rig is dissipated in the braking resistor pack when an over-voltage condition occurs on the VFD's DC bus. The variable frequency drive controls the motor and, through the shared shaft, the expander device at varying rotational speeds thereby enabling characterization of the expander's steady-state efficiency. When a VFD runs at varying rotational speeds the drive must convert the 60Hz grid AC signal to DC, and then back to AC at the new frequency. When the VFD is serving a load (as in many conventional applications such as HVAC fans) this AC-DC-AC conversion creates non-linear loading which disturbs the perfect sinusoidal voltage and current waveforms of the electric supply leading to harmonic distortion. In this case, where the induction motor is instead acting as a generator, the same harmonic distortion is created when the power is fed back onto the grid. Although we eventually decided against the grid back-feeding approach, opting to dissipate generated power in the braking resistor, I have nonetheless included the analysis of how such a VFD device connected directly to the grid would behave for illustrative purposes.

The IEEE 2008 application guide describes the concept of harmonics succinctly:

> Harmonic distortion is a form of electrical noise; harmonics are electrical signals at multiple frequencies of the power line frequency. Many electronic devices—including personal computers, adjustable speed drives, and other types of equipment that use just part of the sine wave by drawing current in short pulses (as shown in figure 3.4)—cause harmonics. Linear loads, those that draw current in direct proportion to the voltage applied, do not generate large levels of harmonics. The nonlinear load of a switched power supply superimposes signals at multiples of the fundamental power frequency in the power sine wave and creates harmonics. The nonlinear loads connected to area EPSs include static power converters, arc discharge devices, saturated magnetic devices, and, to a lesser degree, rotating machines. Static power converters of electric power are the largest nonlinear loads. Harmonic currents cause transformers to overheat, which, in turn, overheat neutral conductors. This overheating may cause erroneous tripping of circuit breakers and other equipment malfunctions. The voltage distortion created by nonlinear loads may create voltage distortion beyond the premise's wiring system, through the area EPS, to another user. (IEEE [10])
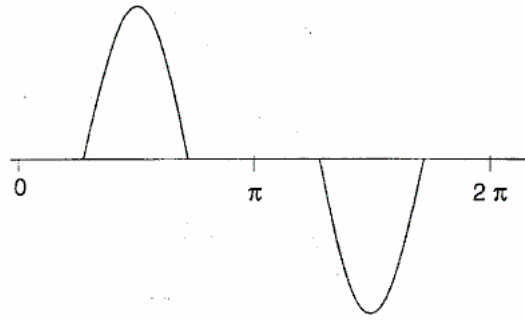
Figure 3.4: Wave of switched-mode power supply (IEEE [10])
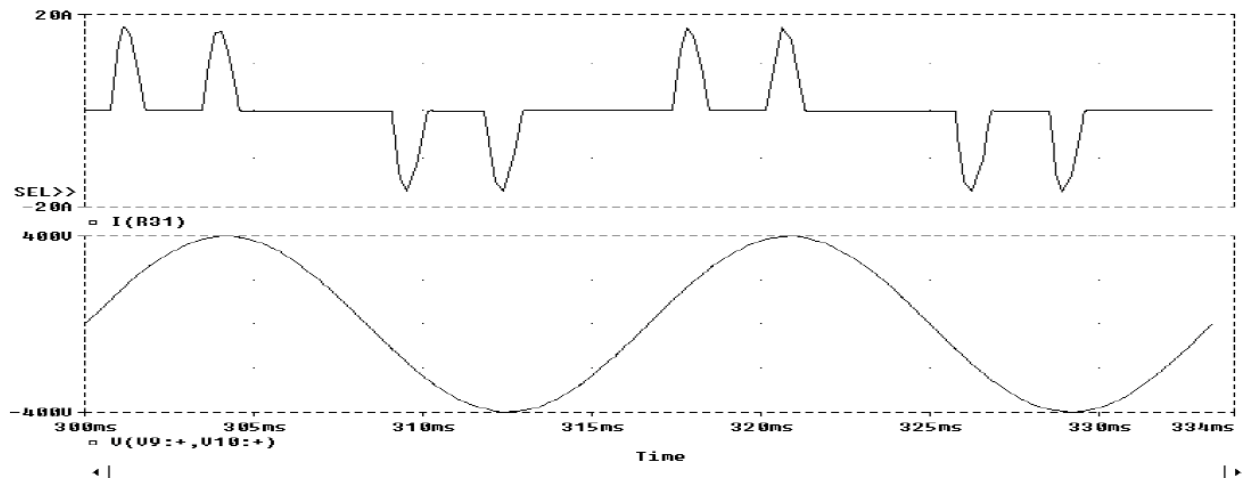
Figure 3.5: Typical pulsed waveform as seen at the input terminals of a VFD. The top graph is current and the bottom voltage. (Swamy [36])

Dissipating the regenerated power in a dynamic braking resistor pack mitigates the harmonic effect. For the purposes of testing I use a dynamic braking resistor, however the harmonic analysis for a regenerative (or bi-directional) VFD is still informative. Figure 3.5 shows what the current and voltage waveforms look like at the input of the VFD.

Results of a harmonic analysis (using the Yaskawa P7 Harmonics estimator software) show that the choice of the point of common coupling (PCC) determines the outcome of the test. Often the point of common coupling is defined at the area electric power system (EPS), which in this case is the distribution network at the point where the building connects to the PG&E grid. However, this doesn't ensure that other customers inside the building have adequate power quality, so IEEE-1547 has instead defined the point of common coupling at the input terminals of the device, or at the point closest to the device where the same feeder serves another piece of equipment. The results using this PCC show that our variable frequency drive, the Yaskawa V1000, would exceed the IEEE-519-1992 harmonics recommendation if operated at full capacity (15 kW). Although the maximum capacity we plan to achieve is just 1 kW, this is nonetheless relevant information in case we ever want to produce more power on this test rig. The measured total demand distortion

51

(TDD), defined as the current harmonic distortion in percent of maximum demand load, for any such device at the input terminals must be less than 5% to meet the IEEE-1547 standard (IEEE [10]).

One should be in compliance with all local utility regulations when feeding electricity onto the grid. Because the University of California must abide by rules governing it's local utility, all safety and interconnection regulations should be approved through Pacific Gas and Electric (PG&E). Although PG&E's Rule 21 is based in part on IEEE-1547, the implementation of the PG&E rule prevents connection of any device that puts power onto the grid (even if that power is simply coming from an storage device fed by the grid as in our case with the compressed air) without going through a lengthy and costly engineering review by PG&E engineers. So, despite the myriad benefits of distributed renewable generation including potentially higher reliability of grids, decreased transmission constraints, and decreased cost of heat and electricity grid (Casten and Ayres [4], Norwood et al. [23]), attaching a device the back-feeds the grid in California PG&E territory is difficult. Rule 21 dictates that the initial application cost is $800, a building disconnect switch dedicated to the generator need be installed, and that a supplemental engineering review might be necessary at PG&E's discretion and further cost to the applicant.(PG&E [25]) To circumvent this process, the test system wastes the electrical energy generated during testing into resistor banks, which in turn dissipate heat into the room, thereby increasing the load on the building HVAC system.

3.4   Results of the Katrix expander testing

Testing on the Katrix expander using compressed air was partially completed before the failure of a bolt inside the expander halted further testing at higher speeds. The manufacturer tells us that this failure mode will be corrected in future prototypes. That being said, the Katrix expander shows excellent promise in achieving very good isentropic efficiency (80-95%) at reasonable pressure ratios (6-11) as shown in figure 3.6 and figure 3.7. The average values produced from 300 seconds of steady-state operation are shown as points on the figure. Full data from the test runs is also shown in Appendix A.

As can be seen in the figures, data was collected at VFD set points corresponding to a shaft speed between 31 and 110 rad/sec (300-1050 rpm). Results of testing at higher speeds were thrown out due to excessive saturation of the torque sensor leading to inaccurate results as further discussed in the following sections. Testing around 60 rad/sec caused such severe resonance of the mechanical test bench that a full 15 minute run could not be completed without the VFD faulting. This data was therefore omitted from the final results. The internal failure of the expander occurred at a VFD set point corresponding to a 141 rad/sec (1350 rpm) shaft speed, halting all further testing.

3.4.1   Data processing

We intended to merely calibrate the orifice flow meter using the rotameter, but instead left the rotameter in line during testing, therefore providing a redundant mass flow measurement. This
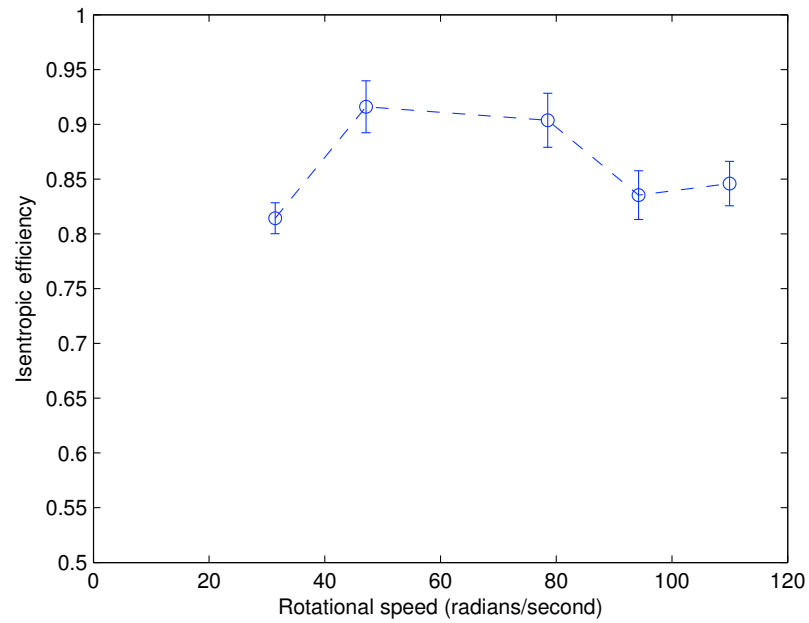
Figure 3.6: Isentropic efficiency of Katrix expander on compressed air (error bars indicate one standard deviation)
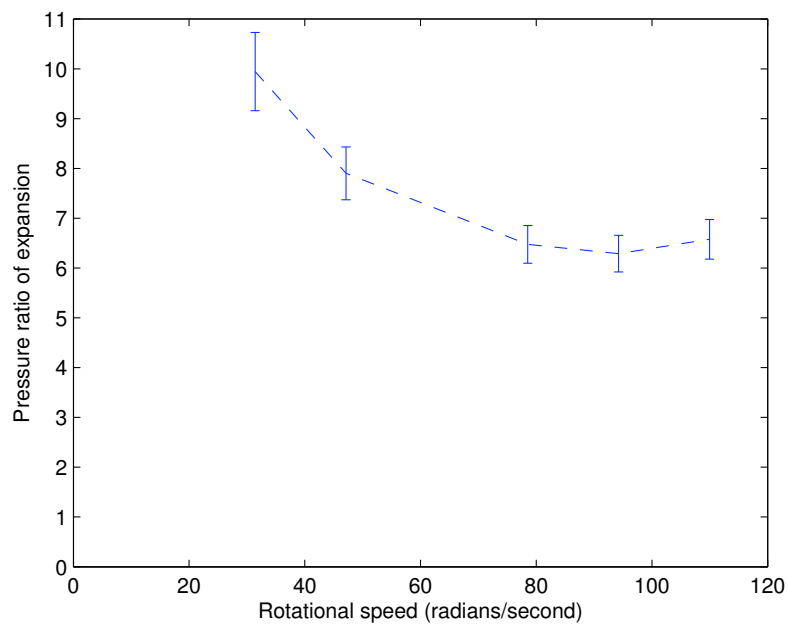

Figure 3.7: Pressure ratio of Katrix expander on compressed air (error bars indicate combined total accuracy)

redundant measurement allows for more precise reporting of the notoriously uncertain mass flow measurement as seen in figure 3.8. Mass flow rate is first calculated using Blevins's orifice equation for incompressible flow through a thin square-edged orifice (Blevins [3]):

$$\dot{m} = \frac{\rho \pi d^2 C}{4\left[1 - (d/D)^4\right]^{\frac{1}{2}}} \left[\frac{2(p_u - p_d)}{\rho}\right]^{\frac{1}{2}} \tag{3.1}$$

where the coefficient C, the ratio of the actual flow rate to the ideal flow rate, for corner tap orifices is defined as:

$$C = 0.5959 + 0.0312\beta^{2.1} - 0.1840\beta^8 + 91.71\beta^{2.5} Re^{-0.75} \tag{3.2}$$

where the ratio of the inner diameter of the orifice to the inner diameter of the pipe on each side $\beta = \frac{d}{D}$, and the Reynolds number:

$$Re = \frac{\frac{D}{d} U D}{\nu} \tag{3.3}$$

where U is the velocity of air through the pipe, d is the inner diameter of the orifice, D is the inner diameter of the pipe, ρ is the density of air in the pipe, ν is the kinematic viscosity, and $(p_u - p_d)$ is the differential pressure across the orifice.

The algorithm I developed solves for the mass flow rate when seeded with an air velocity estimate by first solving eq. 3.2 for C and subsequently eq. 3.1 for $\dot{m}$. This mass flow rate leads to a new U with which to start the next iteration using

$$U = \frac{\dot{m}}{\rho \pi (\frac{D}{2})^2} \tag{3.4}$$

This procedure is repeated in code until suitable convergence on mass flow rate is reached. This calculation yields a mass flow rates that agree well with the results of the spreadsheet provided by the orifice plate manufacturer (Dwyer Instruments).

Calculating mass flow rate for the rotameter is more straightforward. During each test run I view the rotameter float and record the percent of scale shown in steady-state. Then using the upstream pressure and temperature measurements I calculate mass flow rate by finding the calibration of the rotameter at those conditions (with the manufacturer's calibration software). See Appendices A and B for the Matlab code and instrument details.

I use error bars in two ways in reporting the results of the expander testing. First, for quantities where there are redundant sensor measurements, or those derived from redundant sensor data (e.g. power, efficiency, mass flow rate) the error bars indicate the standard deviation s, of a data vector x, with the number of elements in the sample, n (Mathworks [17]):

$$s = \left(\frac{1}{n}\sum_{i=1}^{n}(x_i - \bar{x})^2\right)^{\frac{1}{2}} \tag{3.5}$$
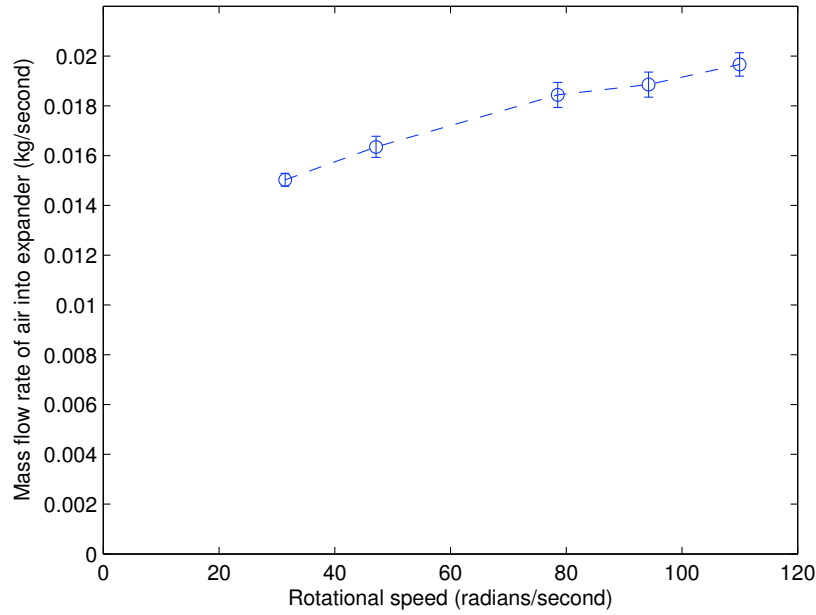
Figure 3.8: Mass flow rate of air through expander (error bars indicate one standard deviation)

where

$$\bar{x} = \frac{1}{n} \sum_{i=1}^{n} x_i \tag{3.6}$$

This calculation assumes that all derived measurements are truly independent, but is not strictly accurate for derived measurements such as fluid enthalpy and efficiency because in this test setup there are independent/redundant mass flow measurements, but some single temperature and pressure measurements. Since temperature and pressure measurements are comparatively more robust than mass flow rate measurement, the resulting underestimate of the standard deviation is ignored. Because the accuracy of the data acquisition hardware is so high, any data acquisition error is also omitted from the error bars. The second way in which error bars are reported here are for those sensors that have manufacturer published accuracy (e.g. pressure, temperature, rotational speed, and torque measurements). These error bars report total combined accuracy or tolerance for these types of measurements. Derived values (such as pressure ratio, torque, mechanical power) have error bars derived from the relative contribution of accuracy from each sensor. The details of these combined error calculations are available in the full Matlab code of Appendix B.

Figure 3.10 and figure 3.9 show temperature and pressure measurements of air entering and exiting the expander are 310K, 10 bar, and 273K, 1 bar respectively with relatively small variations at different expander rotational speeds. The enthalpy change of the working fluid as shown in figure 3.11 is calculated from these measured temperature and pressure values using the Engineering Equation Solver software.
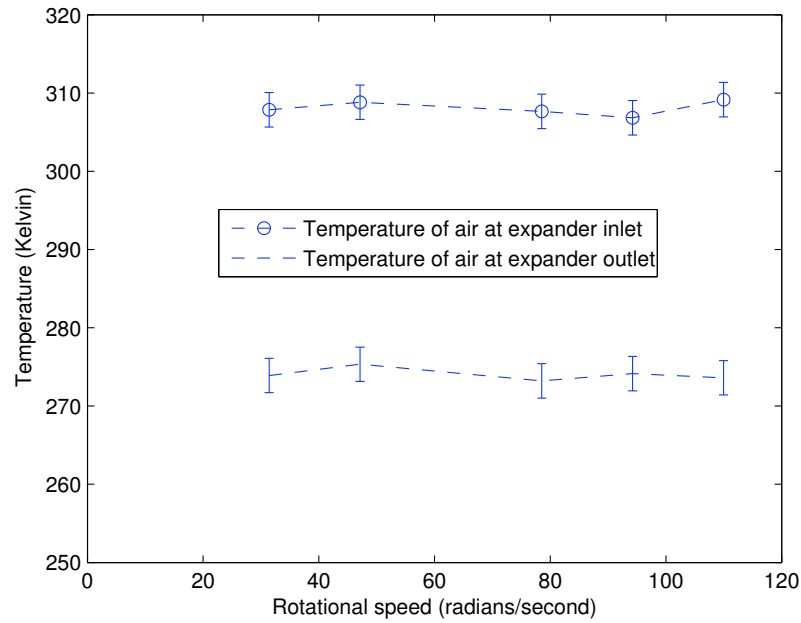
Figure 3.9: Temperature of air at expander inlet and outlet (error bars indicate combined total accuracy)
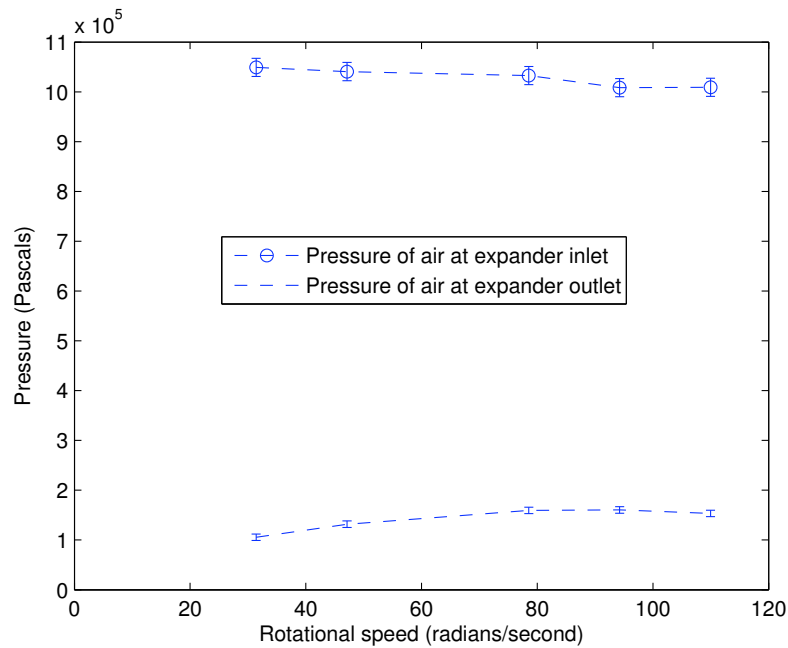
Figure 3.10: Pressure of air at expander inlet and outlet (error bars indicate combined total accuracy)
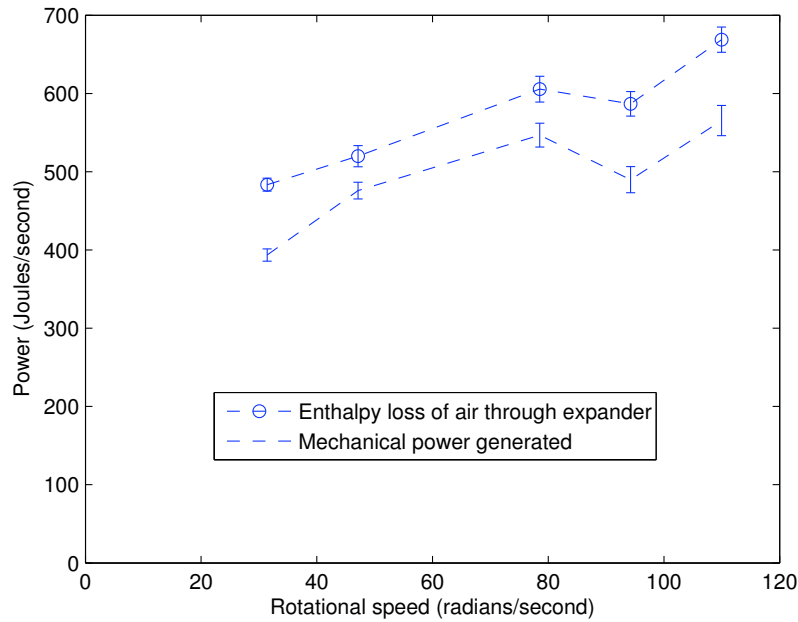
Figure 3.11: Enthalpy loss of air through expander, and mechanical power generated (error bars indicate total combined accuracy)

Mechanical power, also shown in figure 3.11, is simply calculated as rotational speed (as regulated by the VFD) multiplied by average torque, shown in figure 3.12.

3.4.2 Torque oscillation

As mentioned in the last section, the measurement of torque on the shaft between the expander and VFD mysteriously resulted in large periodic oscillations that varied inversely with rotational speed as shown in figure 3.13. Figure 3.14 through figure 3.20 show the 300 second oscillating differential pressure (across the orifice plate) and torque data at each rotational speed. Note that these speeds are set points of the VFD, as we do not actually measure the speed independently in this test setup. Mass flow rate is proportional to differential pressure, therefore the orifice plate flow meter data corroborates the oscillating torque data as a real effect. Note that the torque oscillates so greatly that the expander goes from generating power to absorbing power over the course of one period of oscillation. The full data can be found in Appendix A.

A few possibilities as to the cause of the oscillations have been hypothesized and explored limitedly:

1. A Helmholtz oscillation occurs in the air intake port or supply line to the expander inlet where the opening and closing of the passageways into the expander leads to a resonance similar to that generated by blowing across the top of a bottle. Initial analysis of this phenomena indicates that the frequency of the observed torque oscillation is several orders
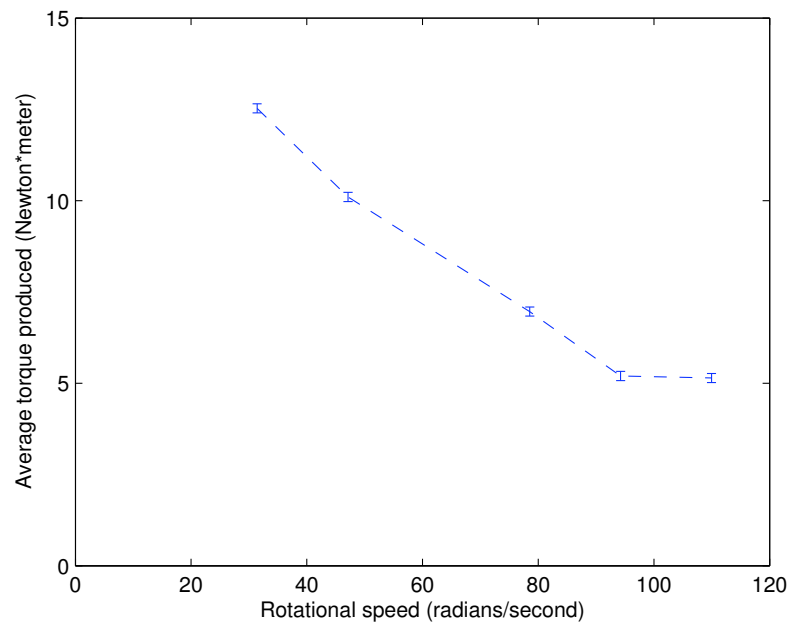
Figure 3.12: Torque generated by expander (error bars indicate total combined accuracy)
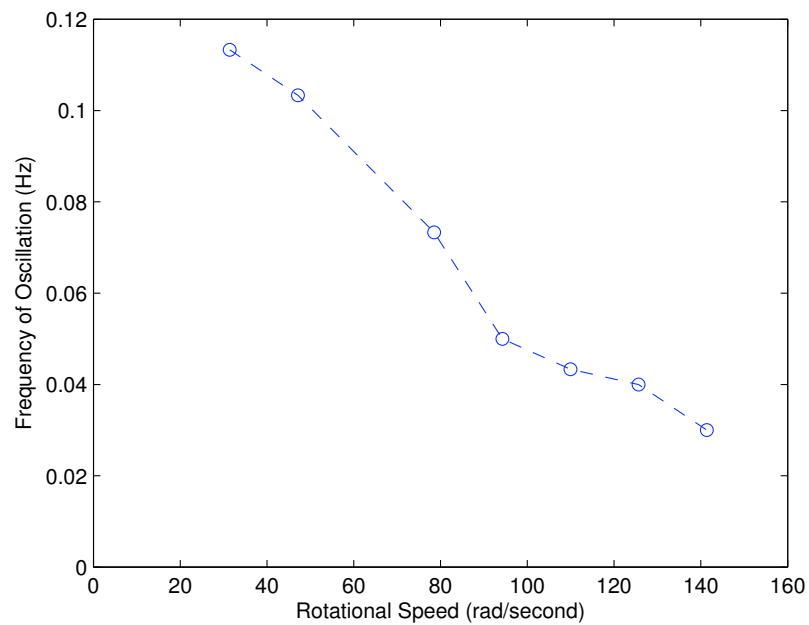
Figure 3.13: Frequency of torque oscillation on shaft
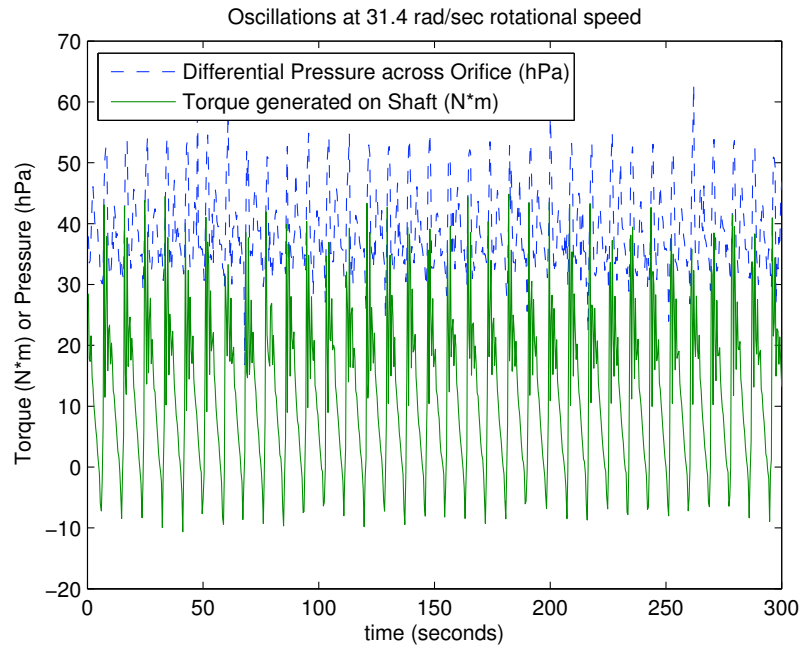
Figure 3.14: Torque and differential pressure oscillations at 31.4 rad/sec set point
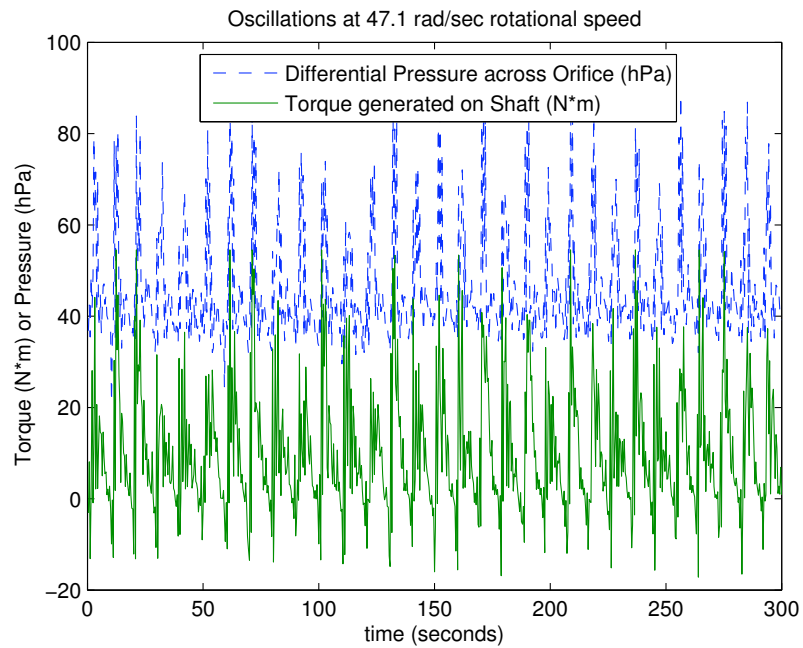
Figure 3.15: Torque and differential pressure oscillations at 47.1 rad/sec set point
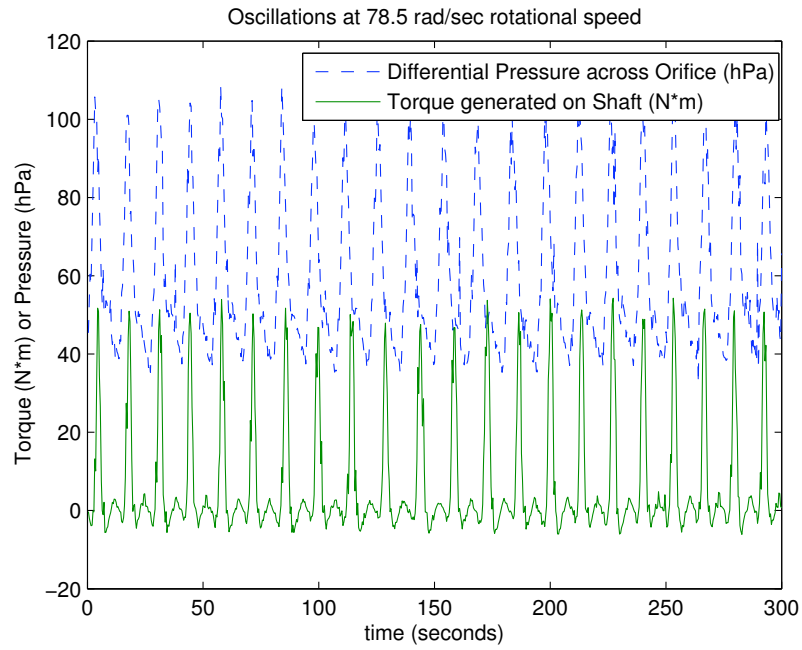
Figure 3.16: Torque and differential pressure oscillations at 78.5 rad/sec set point
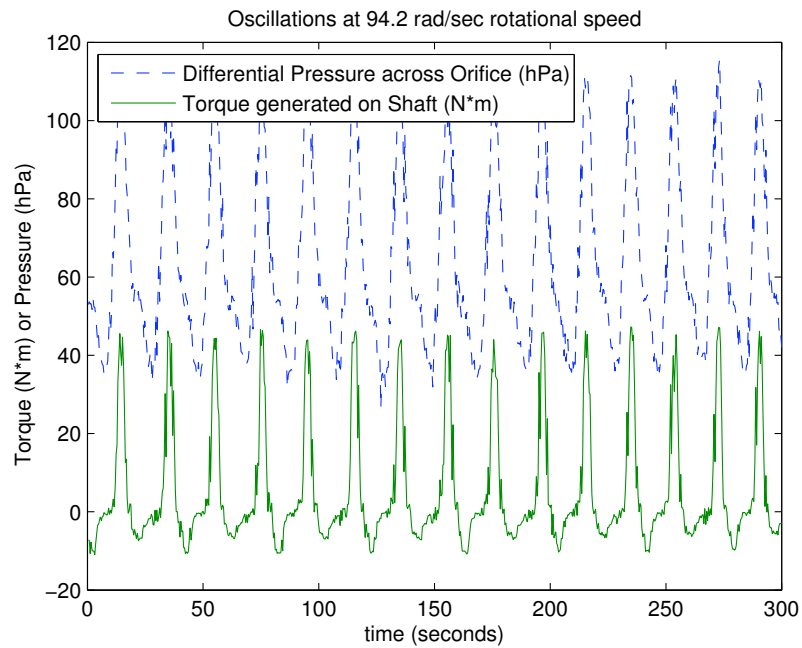
Figure 3.17: Torque and differential pressure oscillations at 94.2 rad/sec set point
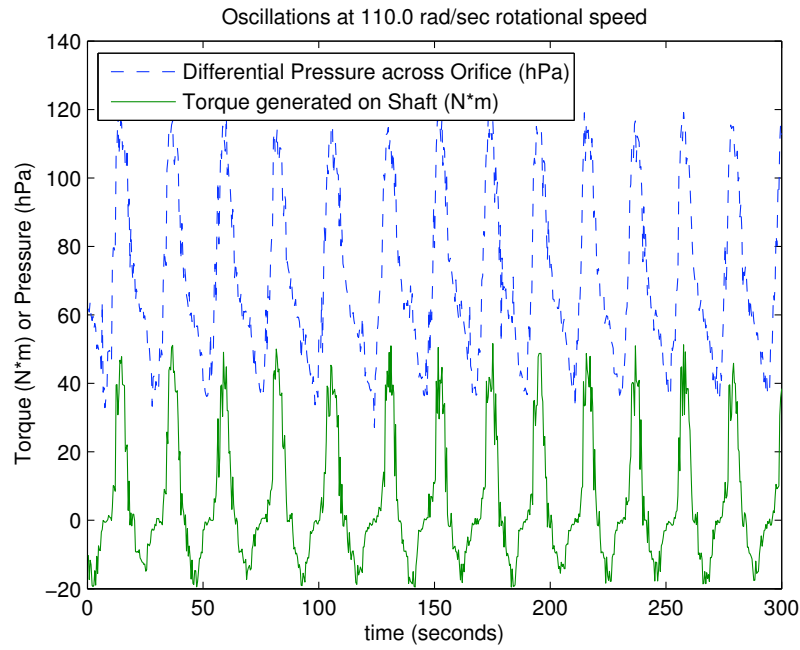
Figure 3.18: Torque and differential pressure oscillations at 110.0 rad/sec set point
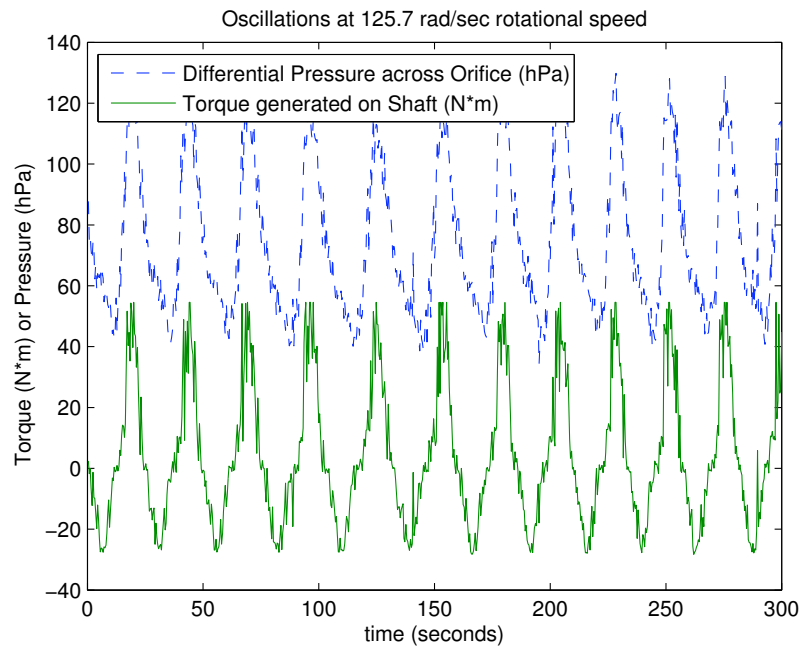
Figure 3.19: Torque and differential pressure oscillations at 125.7 rad/sec set point
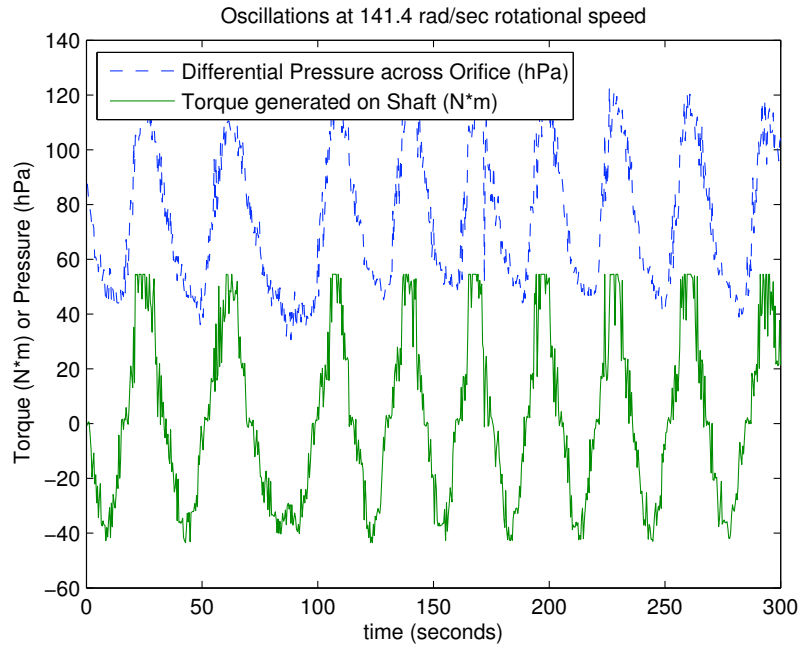
Figure 3.20: Torque and differential pressure oscillations at 141.4 rad/sec set point

of magnitude too low given the length of the ports internal to the expander and the air lines from the booster pump leading up to the expander.

2. A beat frequency is generated by some combination of the effects of the pulsed nature of the operation and control of the induction motor by the VFD, the pulsed air intake into the expander, vibrations in the shaft couplings, etc. This option was not fully explored before the expander failed, however given that we are using a fairly rigid coupling (Lovejoy jaw-type L coupling) between the expander shaft and the induction motor, that the air pressure remains fairly constant at the expander inlet (as shown in Appendix B) and that the VFD is operating in speed control mode, it is difficult to imagine such a large torque oscillation being the result. Additionally, a corresponding speed oscillation might be expected in such a case, and although we are not measuring rotational speed directly, the VFD would fault if speed varied by more than a couple percent. If speed did vary we should hear this oscillation during the operation of the expander, but we do not.

3. The torque sensor is faulty. The fact that the mass flow rate into the expander varies exactly in phase with the torque indicates this is a real phenomenon, not a measurement artifact. However, there could be some subtle (unlikely) effect due to static charge building up on the in-line torque measurement devices shaft, distorting the electrical output and causing the actual magnitude of this effect to be exaggerated. The torque sensor was successfully calibrated manually under a static load in the mid-range of its sensitivity before tests began, and the manufacturer calibrated the device prior to shipping.

4. A lubrication or other internal affect in the Katrix expander is periodically restricting flow

62

rate into the expander. This type of problem would be a "breathing" effect as studied extensively in engine design. The result of this effect would be both an oscillating torque output and a mass flow oscillation, in agreement with measured results. Further exploration of the internal breathing of the Katrix expander and possibility of internal periodic blockage by lubricant (or something else) is recommended. All signs seem to indicate that flow is actually being restricted, unlikely to be caused by increased mechanical friction, but more likely caused by an actual periodic restriction of the intake or exhaust pathways of the air through the expander.

Whatever the cause, the oscillating torque periodically saturates the sensor at its maximum value as can be seen in figure 3.19 and figure 3.20. For this reason, these last two data runs, at the highest rotational speeds tested, were not reported in the efficiency analysis.

3.5 Conclusions

It is worth noting that although I went to great pains to get good data, there are ways in which these efficiency results could overpredict (or underpredict) actual performance. Typically the mass flow rate measurement is the most difficult to measure, but using multiple mass flow rate sensors in good agreement indicates this is not likely an issue. However, there were not redundant measurements for torque, temperature, nor downstream pressure in this test setup. If the downstream temperature or pressure measurement was too high, upstream temperature too low, or torque measured too high, these results would overpredict actual performance. There are several factors that lead me to believe the measured reading were indeed accurate. For instance the upstream piping was the right temperature to the touch, and frost formation on the expander outlet indicated that thermocouple was certainly not reading too low. Pressure guages on the expander inlet confirmed the sensor reading, but downstream pressure was harder to verify because the expander outlet was vented to atmosphere. Lastly, the torque sensor was calibrated by the manufacturer, and then again under static load in our laboratory, but not under dynamic load.

It is clear from the results of testing that rotary lobe expanders exhibit great promise for small-scale efficient systems. Not only are the mechanisms simple and easy to manufacture, but an expansion ratio greater than 8:1 and demonstrated isentropic efficiency of 80-95% are best in class. Detailed analysis of DCS-CHP systems (see Chapter 4) show that this combination of efficiency and pressure ratio enables high overall solar-electric system efficiency. Furthermore, positive expansion devices can expand wet fluids, opening up the possibility of using water at saturated conditions. Water is an excellent fluid to use for DCS-CHP systems because of its benign nature, ubiquity, and unsurpassed two-phase heat transfer properties. Additionally, the boiling point of water is well matched to the grades of heat used in residential and commercial establishments. The next steps in development of an efficient rotary lobe expander for DCS-CHP applications will be improving reliability, and design of lubricant-free bearings that work with condensing steam.

Chapter 4

Simulation Framework for a Distributed Concentrating Solar Combined Heat and Power System

4.1   Introduction

A distributed concentrating solar combined heat and power system will use solar energy to provide the heat input to a Rankine cycle to serve thermal and electrical loads. This system aims to produce heat and electricity cost competitively with other renewable technologies, while being simple to manufacture. An efficient and low-cost heat engine is crucial to system efficacy and is the main focus of research. Determining an appropriate working fluid and turbine design requires modeling the turbine performance as it interacts with all other system components. To accomplish this, analytical models of expanders and certain aspects of solar thermal collectors have been coded in Matlab software. These different simulations of Rankine cycle components provide valuable information, however analysis can only be done on individual components. A framework that integrates each component of a Rankine cycle is important to predict overall cost and performance.

Many components in a Rankine cycle system, when optimized, have adverse effects on other parts of the system. For example, high pressure ratios are good for maximizing cycle efficiency, but higher pressure ratios often cause efficiency problems in the expander due to air leakage around the rotor. Certain collectors operate at higher efficiencies with wet steam, but turbines often see increased wear with wet steam due to water droplets impinging on the blades. To facilitate the design and evaluation of a Distributed Concentrating Solar Combined Heat and Power (DCS-CHP) system, an advanced Rankine cycle simulation software that is able to model interactions between different component choices is useful. Because elements of a Rankine cycle operate differently at varying pressures, temperatures, flow rates, vapor ratios, and weather conditions, thermodynamic Rankine cycle analysis falls short of optimizing hardware-working fluid interactions. In previous research, a model for performance of a small-scale radial inflow

turbine (Sunter et al. [35]) and Tesla turbines (Romanin et al. [30]) were analyzed, and Chapter 3 shows the experimental results of a rotary lobe expander. This new tool can use these results to model interactions between the system and environment for the purpose of location-based design of appropriate technology. This tool uses an object-oriented framework, in Matlab software, that combines existing elements and allows addition of other elements – including heat exchangers, pumps, generators, turbines, solar collectors, and energy storage mechanisms. In this chapter, first the tool is described, and then results and analysis of a case study of the tool used for comparing appropriate expander and collector choices is demonstrated.

4.2 Program description

The program follows the Simulation-Environment-Agent framework. A Simulation contains several agents, called *System*s, and several *Environment*s. The *System*s contain several components, which represent each element of a Rankine cycle (e.g. turbine, condenser, pump, generator, etc.). An *Environment* consists of weather data for a specific location. This data is uploaded from NREL's National Solar Radiation Database. This program integrates the data into a method of the *Environment* class. This method can be run (with an input of the imported data) to build *Environment* objects containing useful weather information including site name, site location, typical insolation, typical temperatures, etc.

Components contain the necessary information to calculate the output state of a fluid based on the input state. Currently all components are generic in that they do not contain any in-depth analysis of their operation - most operate simply with an isentropic efficiency. In the future, our advanced component models will be coded into objects that can provide a more in-depth analysis of component operation.

*System*s contain one of each component necessary for a Rankine cycle. When given constraints on the Rankine cycle, specifically the high temperature, high pressure, and low pressure of the system, the *System* is able to calculate the thermodynamic properties of the cycle (work output, heat output, energy input, solar-electric efficiency, etc.) by passing an input fluid state to the component, which then returns an output fluid state (to be passed as input to the next component).

Fluid states are stored as properties of components. Each component has a *StateIn* and a *StateOut* property (for generators, *PowerIn* and *PowerOut*) that represent objects of the *FluidState* class. *FluidState* objects have the properties of *Temperature*, *Pressure*, *Entropy*, *Enthalpy*, *InternalEnergy*, *Density*, and *Quality*. These objects also have a *FluidModel* property that will accommodate multiple fluids. Engineering Equation Solver or XSteam (by Excel Engineering) software calculates fluid properties. This allows systems to be analyzed with many different working fluids, including water.

Creating a *Simulation* object calls its *GUI* property. This brings up a graphical user interface (GUI) that displays a list of *Environment*s and *System*s contained in the *Simulation*. *Environment*s can be added by running the *getSitesFromSite* method of *Simulation* with an input of the *site* structure, or by using the GUI. The *site* structure is is processed NREL TMY3 (Typical Meteorological Year) data stored in the file *SITESsaved.mat*. This data can also be imported from

raw TMY data, but re-processing the raw data takes a significant amount of time compared to importing preprocessed data.

System data can be added using the **Add System** button. Pressing the button brings up a GUI with an image of a Rankine cycle. Next to each component of the Rankine cycle is a pop-up menu that allows the user to select the type of component. The user can also select efficiencies and input conditions to the cycle. Currently only default components exist, but additional components will be added as the code is developed. For example, the turbine pop-up menu currently only allows the user to select *Turbine*, which simply calculates output given a user-specified isentropic efficiency, but other expander types can be incorporated, which could allow configuration of the rotor size, max speed, efficiency as a function of pressure ratio, etc. Once a system is configured, pushing the **Save & Add System** button constructs a *System* containing the components and returns to the original GUI with the new *System* added.

Once *System*s and *Environment*s have both been added, any number of *System*s and *Environment*s can be selected from the respective lists. Clicking the **Calculate** button then analyzes each possible combination of *System* and *Environment* and returns the results.

4.3   Program structure

Figure 4.1: UML diagram of program
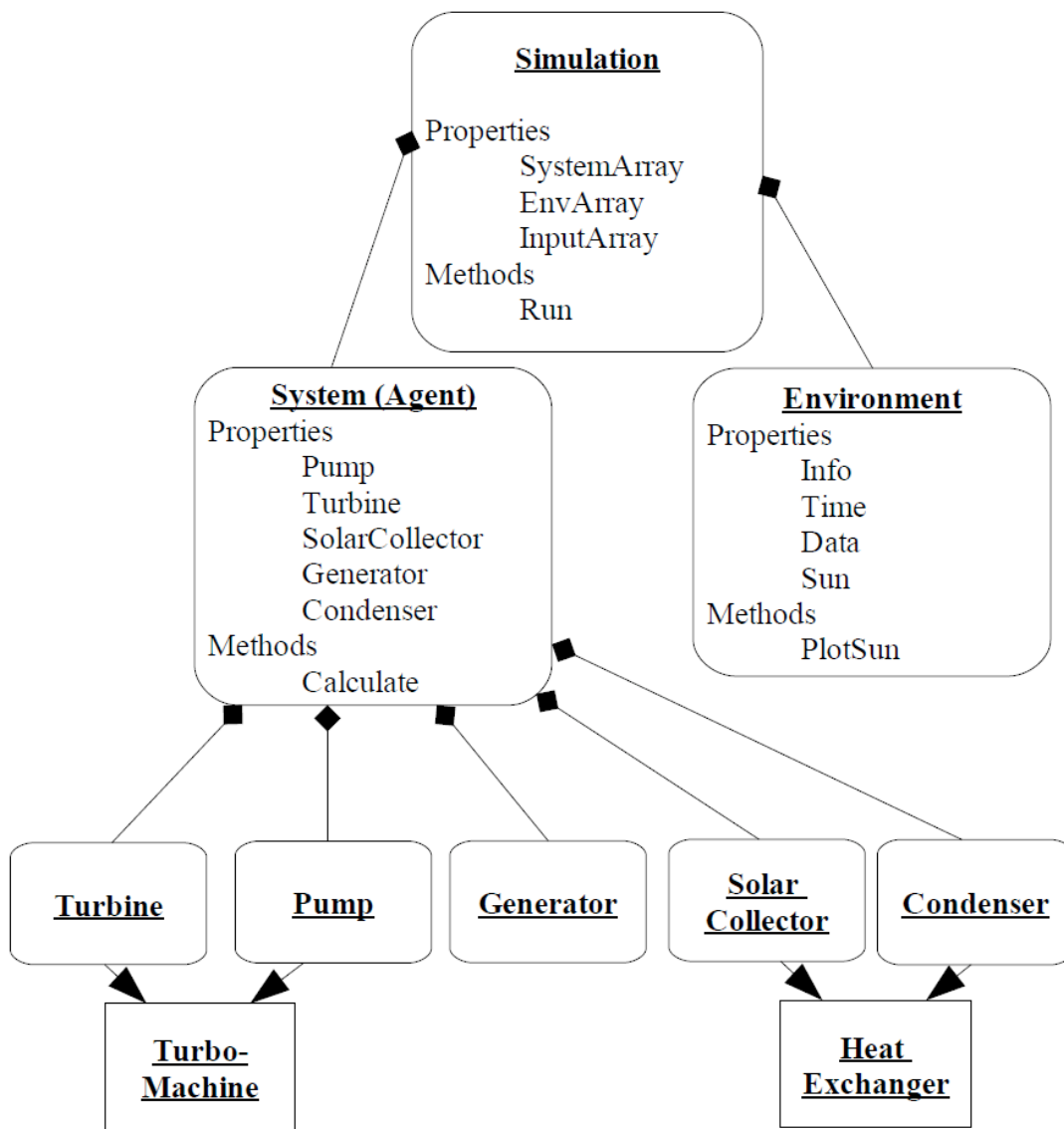
Classes will be discussed from the "bottom" of the hierarchy to the "top" (i.e. classes that are part of or properties of other classes will be discussed first)

4.3.1   FluidState

FluidState is the class that contains fluid properties. The constructor of *FluidState* must be called with the name of a fluid and with two independent properties of that fluid. For example:

```
        F = FluidState('water','Pressure',5,'Temperature',230)
```

A case statement then determines the two independent state properties, and enters the appropriate inputs into a fluid calculator. The constructor then populates the remaining properties of *FluidState* (*Temperature*, *Pressure*, *Entropy*, *Enthalpy*, *InternalEnergy*, *Density*, and *Quality*) so that all thermodynamic properties of the fluid are known. Instead of a property name and value, *FluidState* also accepts the strings `'Saturated Liquid'` or `'Saturated Vapor'`, in which case the fluid calculator finds a state using one specified property at saturation conditions. *FluidState* also contains a property for the fluid model. All string inputs to *FluidState* are case insensitive.

4.3.2   Components

Components is not a class itself, but all mechanical elements of a Rankine cycle, including turbines, pumps, generators, solar collectors, and condensers, are referred to as components. Some components inherit from a shared super class (e.g. *Turbine*s and *Pump*s are both *TurboMachine*s, and *Condenser*s and *SolarCollector*s are both *HeatExchanger*s).

4.3.2.1   HeatExchangers

The *HeatExchanger* class contains the properties *StateIn*, *StateOut*, and *Eta*. It has a *getHeat* function that calculates the enthalpy difference between its *StateOut* and *StateIn* properties.

*Condenser*s are *HeatExchanger*s that remove heat from the Rankine cycle in the process of condensing the fluid from a vapor to a liquid. If no input is given to the constructor, all properties of *Condenser* are left blank. If one *FluidState* is given as an input, it is set to the *Condenser*'s *StateIn* property and *Condenser*'s *calculate* method is called with *StateIn* as an input. *Condenser*'s *calculate* method calculates *StateOut* by constructing a *FluidState* with inputs of *StateIn.Pressure* and `'Saturated Liquid'`. In other words, the input to the condenser is typically partially or completely vapor; the output to the condenser is at the same pressure as the input, but in a saturated liquid state.

SolarCollectors are *HeatExchanger*s that transfer heat from the sun's radiation into the working fluid. *SolarCollector*s have a static method *getDefaultEta* that returns the default value for the efficiency of the collector. The constructor takes two inputs, *stateIn* and *temperatureOut*. If no inputs are specified, all properties of *SolarCollector* are left blank. If both inputs are specified, *SolarCollector*'s *calculate* method is called. If one or more than two inputs are specified, the constructor returns an error. The *calculate* method takes three inputs aside from a collector object: *stateIn*, *temperatureOut*, and *eta*. If no *eta* is specified, a default *eta* is returned from the static method *getDefaultEta*. The *calculate* method than sets to *StateOut* a *FluidState* with the same pressure as *StateIn* and with a temperature of *temperatureOut* (the specified high temperature of the system).

4.3.2.2   TurboMachines

TurboMachine is an abstract class inherited by classes like *Turbine* and *Pump*. Similar to
HeatExchanger, *TurboMachine* has three properties; *StateIn*, *StateOut*, and *Eta*. *TurboMachine*
has three methods, which calculate the volumetric ratio, pressure ratio, and work using the fluid
properties of *StateIn* and *StateOut*.

*Turbine*s are *TurboMachine*s that expand a fluid and produce work. The constructor of a *Turbine*
takes three inputs: a *stateIn*, *pressureOut*, and *eta*. If all three are specified, the calculate method
is called. If none are specified, the *Turbine* object is left blank. *Turbine* has a static method called
getDefaultEta that returns a default value for the isentropic efficiency if none is specified. The
calculate method takes in a *Turbine* object, a *stateIn*, *pressureOut*, and *eta*. *StateIn* is a *FluidState*
specifying the inlet conditions. *PressureOut* is the low side pressure of the turbine. If no *eta* is
specified, the default *eta* is read from *getDefaultEta*. The *calculate* method then calculates the
enthalpy of a constant entropy expansion (i.e. a *FluidState* with *stateIn.Entropy* and *pressureOut*),
then multiplies the ideal enthalpy difference by the isentropic efficiency to find the actual
enthalpy drop. This new *enthalpy* and *pressureOut* is used to determine *Turbine.StateOut*. The
calculate function also outputs turbine work, which is calculated by subtracting the enthalpy of
StateOut from *StateIn*.

Pumps are *TurboMachine*s that use work to compress a fluid. The constructor of a *Pump* works
exactly like that of a *Turbine*. The *calculate* method of a *Pump* functions like that of a *Turbine*,
except that the work is calculated by subtracting the enthalpy of *StateIn* from *StateOut*.

4.3.2.3   Generators

*Generator*s, unlike other components, have the properties of *PowerIn, PowerOut* (instead of
StateIn) and *Eta*. These properties are *double*s as opposed to *FluidStates*. The *PowerIn* property
is typically set to the work output of the *Turbine*, and the *PowerOut* is that work multiplied by
Eta. Like the other components, *Generator* has a static method called *getDefaultEta*. The
constructor calls this method if no *eta* is entered. The *calculate* function for *Generator* takes in a
Generator object, *powerin*, and *eta*. The *Generator.Eta* property is set to *eta* (or to default if none
specified) and the *powerin* value is set to *Generator.PowerIn*. The *PowerOut* property is then
simply the product of those two values. *Calculate* returns *PowerOut*.

4.3.3   System

The *System* class contains all the necessary information for one specific Rankine cycle
configuration (i.e. one specific set of hardware). It has properties *Pump*, *Turbine*, *Condenser*,
Generator, and *SolarCollector*; each being an object of its respective class. Currently, since only
default objects exist, these properties have the same names as the classes of objects that occupy

them. In the future as more types of each component are coded it is possible, for example, for the *Turbine* property to be a *TeslaTurbine* or a *RotaryLobe*. The constructor of *System* takes five inputs, one for each property. If a zero is specified, the constructor builds a default object of that type. *System* has one method, *calculate*, which takes four inputs: *System*, *Thigh*, *Phigh*, and *Plow*. The last three inputs represent the constraints on the Rankine cycle, namely the input pressure and temperature to the turbine and the exit pressure of the turbine.

To calculate all properties of the Rankine cycle, a *FluidState* is created with *Thigh* and *Phigh* as the inputs. This fluid state and *Plow* are passed to *System.Turbine*'s *calculate* method, which then creates the *StateOut* of *Turbine* and outputs the work of the turbine as *turbineWork*. The *Condenser* then takes into its *calculate* function *Turbine.StateOut*, and produces its own *StateOut* (recall from basic thermodynamics that a Condenser is modeled as constant pressure heat removal until the fluid reaches saturated liquid). The output of *Condenser.calculate* (*heatOut*) is the heat output of the Rankine cycle. This heat can be used for domestic heating loads. Next *Pump.calculate* is called with *Condenser.StateOut* and *Phigh*. This returns the fluid, now completely liquid, to the high pressure of the system. The pump work is stored as *pumpWork* for later calculating efficiencies. Finally *SolarCollector.calculate* is called with *Pump.StateOut* (high pressure liquid) and *Thigh*. *SolarCollector.StateOut* is calculated by raising the temperature of the fluid to the high temperature of the system. This value, the heat input to the solar collector, is stored as *heatIn*. Now the *calculate* method of *Generator* is called with *turbineWork* as an input, which then calculates and sets the *Generator.PowerOut* property and outputs *generatorElec*, the amount of electricity generated.

The heat and work inputs and outputs to the system are used to calculate the heat engine efficiency *etaTherm*, the solar to electric efficiency *systemElecEta*, the solar to heat efficiency *systemHeatEta*, and the fraction of Carnot efficiency achieved *fractionCarnotElec*. The latter three values are then set to the output of *System.calculate*.

4.3.4   Environment

Environment objects store the weather data processed from NREL's TMY3 database. Nearly all *Environment*s will be built using *Simluation.getSitesFromSite*, which is called through the GUI. Each of *Environment*'s properties; *Info*, *Time*, *Data*, and *Sun*, are structures that contain all the data from the TMY database. *Environment* has one method, *PlotTestSunData*. When taking as an input a day of the year (1 to 365), this function plots the insolation over the course of a day at that *Environment*'s location for a typical year. This plot provides a visual representation of that site's radiation as shown in figure 4.2.

4.3.5   Simulation

The *Simulation* class properties are an array of all the *System*s, their names, and the inputs to those *System*s. Its methods include a constructor, which by default sets all properties to empty cell arrays, a *Run* function that calculates the performance of every possible combination of systems

70
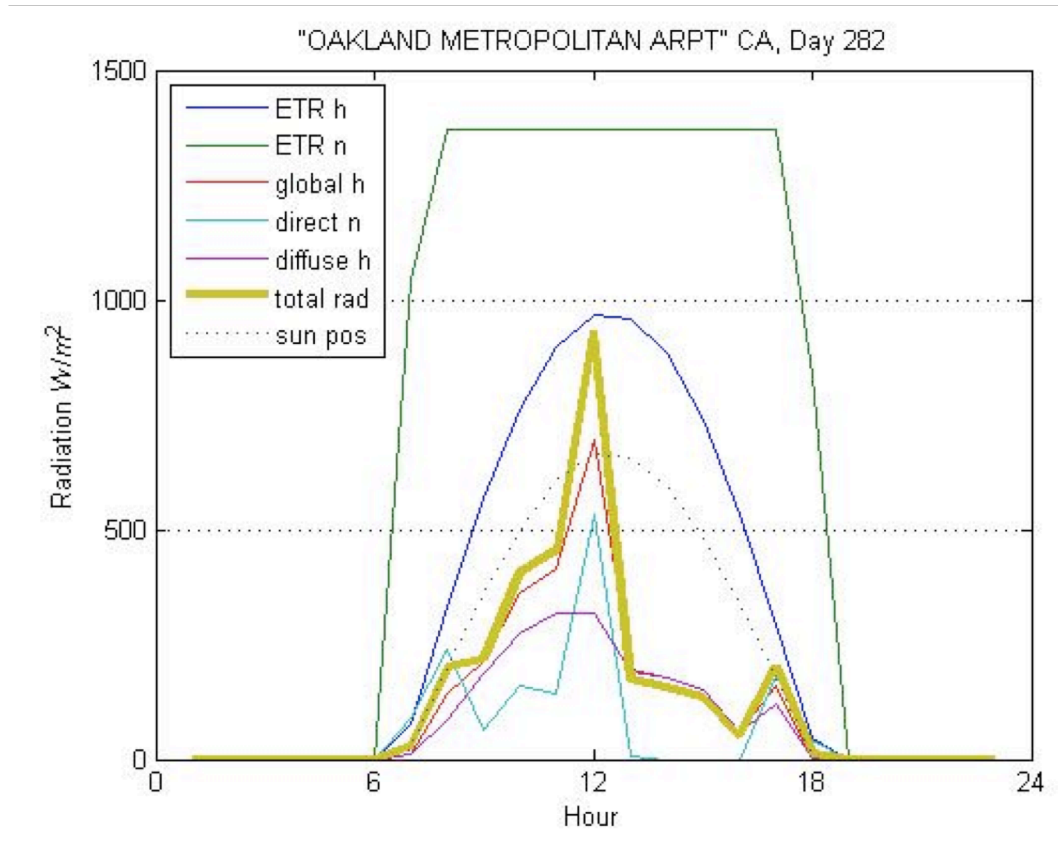
Figure 4.2: Radiation levels for October 9th of a typical meteorological year in Oakland, CA. "ETR" is extraterrestrial radition, "h" is horizontal, "n" is normal, and "sun pos" is the sun's position in the sky

and environments selected on the GUI, and a *Plot* function, which plots the simulation results showing seasonal heat and electricity output for a single system at any number of selected sites. The plot function calls *PlotUSLevels*, a function to display seasonal and yearly data on latitude and longitude axis.

4.3.5.1   Simulation GUI

The *Gui* function of the *Simulation* class provides an interface to select as many different environment and system combinations as desired for simulation. Callback functions are used to process data, call the system GUI or plot the results GUI. The results GUI allows the user to select yearly total heat or electricity output generated by the system and plot it in both seasonal and yearly form.

4.4   Operation of the simulation software

After navigating to the correct Matlab path, the software can be run as follows:

1. Start the Simulation at the command prompt by typing >> S = Simulation()

2. The Simulation GUI will pop up (figure 4.4), and the first step is to select **Add System**, which will bring up the System GUI (figure 4.3):
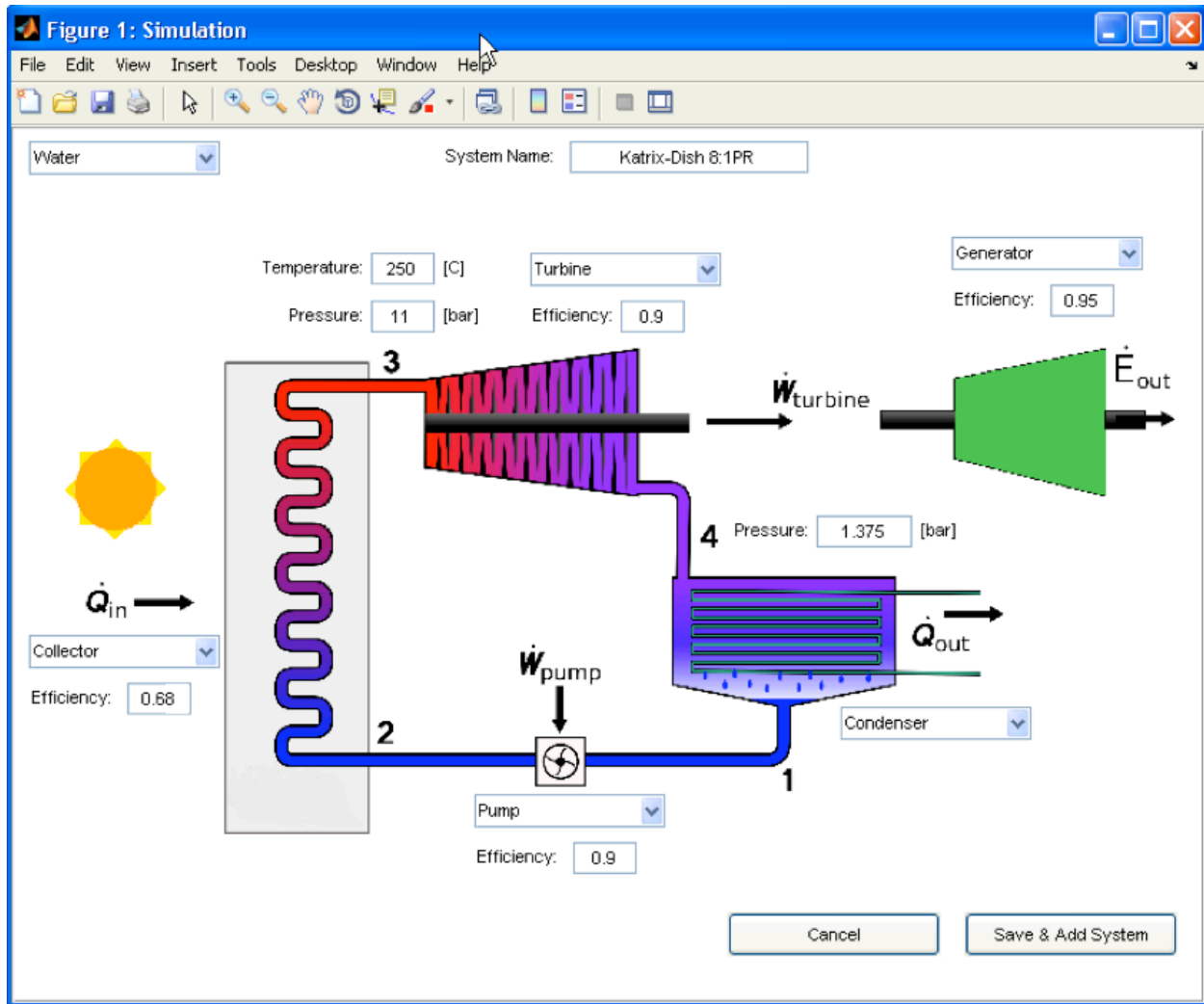
Figure 4.3: System GUI, shown with conditions appropriate for a Katrix expander and dish collector DCS-CHP system

3. Enter desired efficiencies into the boxes for each component and enter appropriate input high and low pressures of the system and the high temperature, then press **Save & Add System**.

4. After adding one or more systems, select **Import Environments** from the Simulation GUI (loading saved yearly solar data from 1020 sites in the US will take several minutes):
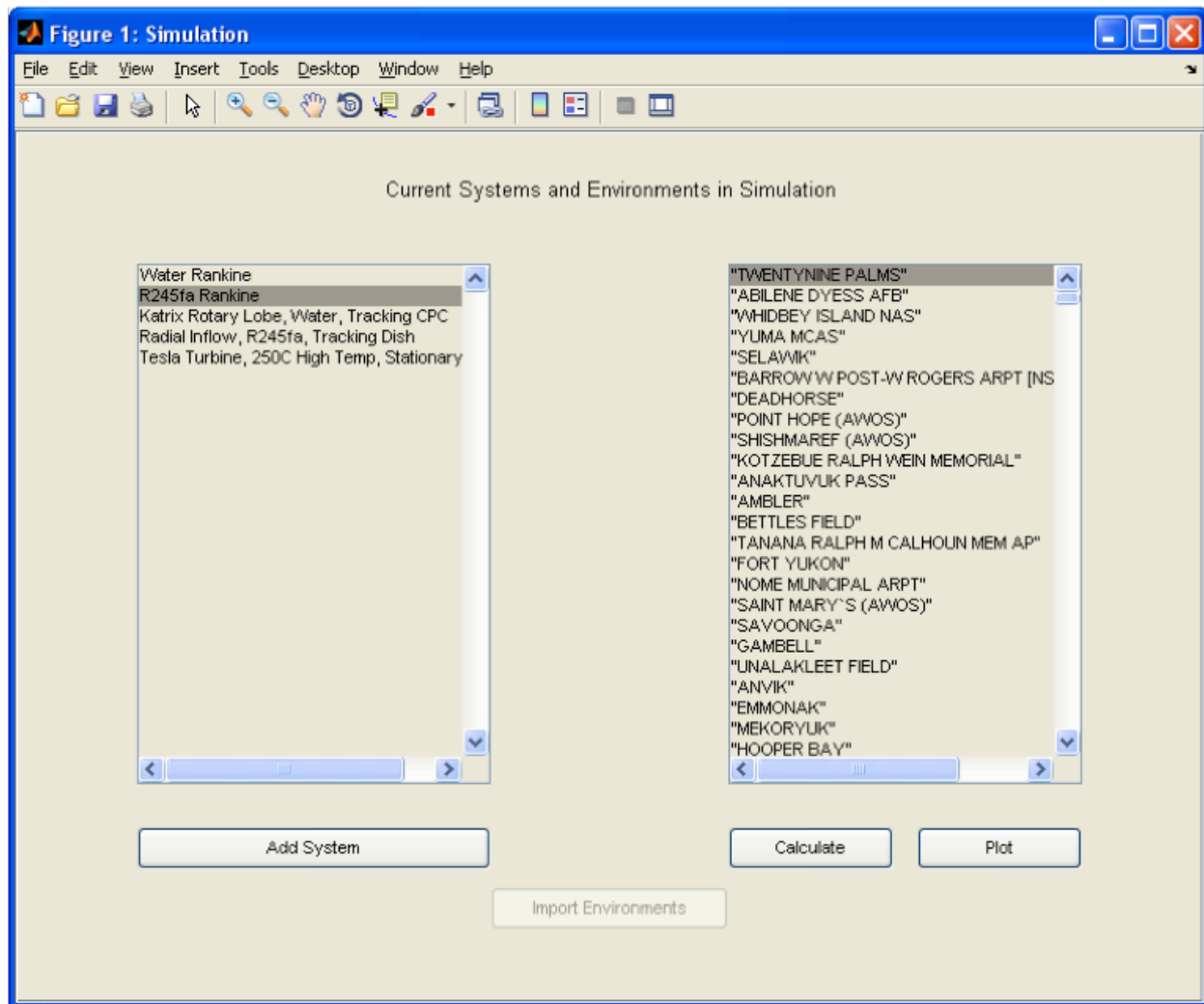
Figure 4.4: The Simulation GUI, shown after several systems and all 1020 environments have been loaded

5. Finally, select as many systems and environments as desired and click the **Calculate** button which will run the simulation for each site-system combination and output *Results* as a cell array to the Matlab workspace.

6. To plot the data, select a single system and as many environments as desired (Selecting all sites, ctrl-a, looks good), then press the `Plot` button. Select if you would like yearly heat or electrical as output and seasonal and yearly data will pop up in new figures as shown in Figures 4.7, 4.8, 4.9 and 4.10.

The *Results* variable is created in the workspace after pressing **Calculate**. *Results* is a cell array is of dimension Nx5, where N is the number of systems, with each cell being the performance results for the whole year, spring, summer, winter, and fall seasons in that order. Within each of these cells there are results for all site combinations selected in the GUI containing five numbers,

corresponding to (1) solar-thermal efficiency, (2) solar-electric efficiency, (3) fraction of Carnot efficiency for electrical generation, (4) total yearly heat output at that site, and (5) total yearly electrical output at that site. The following is an example of the Matlab output as reported in Table 4.1:

>> Results{1}{1}
ans =
0.5833 0.0919 0.5267 969.5886 152.7057

4.5   Case study of an appropriate DCS-CHP system

There is demand today for Distributed Concentrating Solar Combined Heat and Power (DCS-CHP), as demonstrated by the strong growth in photovoltaics and recent growth in solar-thermal heating, but DCS-CHP technology does not exist in the marketplace today to fill that niche. The two technical challenges that have been prohibitive towards the development of a DCS-CHP system are the cost of the solar collector and the efficiency of a small-scale turbine. Continuing innovation in these areas combined with advanced system analysis and design now make such a system possible. One such expander and collector combination is described and evaluated below.

4.5.1   The Orbital Concentrator

One of the fundamental technologies we explore is a new type of solar collector optimally designed for DCS-CHP applications, referred to as the Orbital Concentrator, conceived with the founders of Raw Solar (RawSolar [27]). This technology combines high concentration optics with a compact and static plumbing system, enabling excellent efficiency at working temperatures high enough for efficient steam Rankine cycle performance, while reducing capital and operational costs. This new Orbital Concentrator is a fundamentally different form of solar concentrator, a hybrid balancing the pros and cons of traditional dish and power-tower systems. There is one receiver per reflector, like a dish, but the receiver is fixed in place while the reflector orbits around it following the sun. Specifically, the reflector rotates around a vertical axis passing through the receiver to track the azimuth angle of the sun, and simultaneously tilts up and down and translates in and out to track the zenith angle of the sun while maintaining a fixed focal length between the reflector and the receiver so as to keep a sharp focus on the receiver (Figure 4.5).

Dishes have been well explored by many organizations, including the US Department of Energy. Notable systems include LaJet, SES, and Zenith. Like traditional dishes, Orbital Concentrators have the advantage of achieving very high concentration ratios, suffer near-zero cosine losses, and are robust to tracking and slope error because of their relatively short focal length. Dishes, however, are poorly suited for heating a high temperature working fluid to power a remote heat engine, as the fluid plumbing must be routed circuitously through the dish structure and must include articulate joints. These joints pose significant costs as they must handle continuous

75
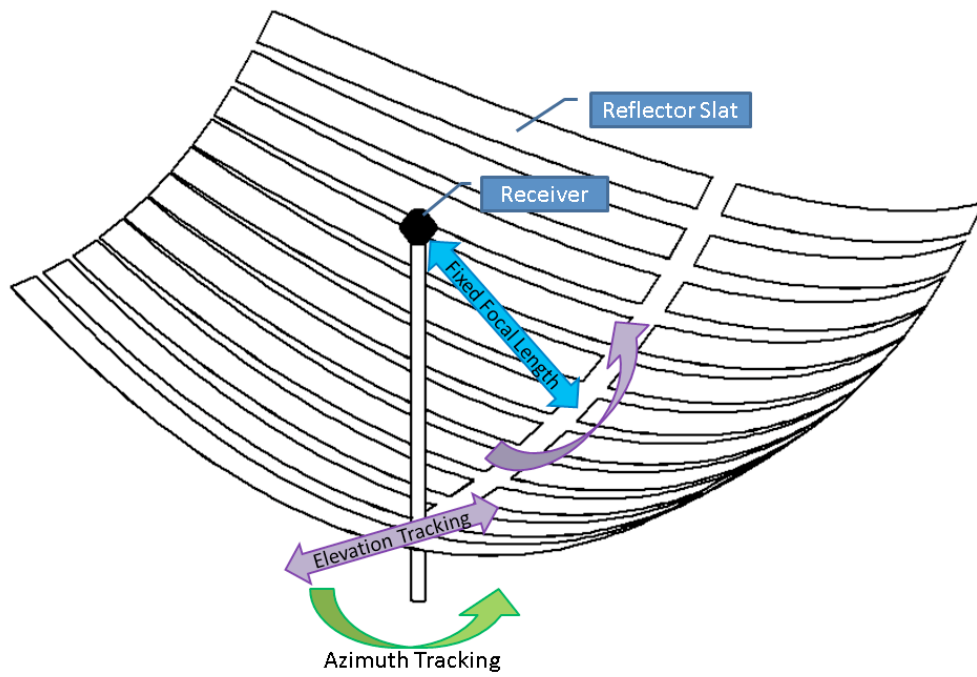
(a)
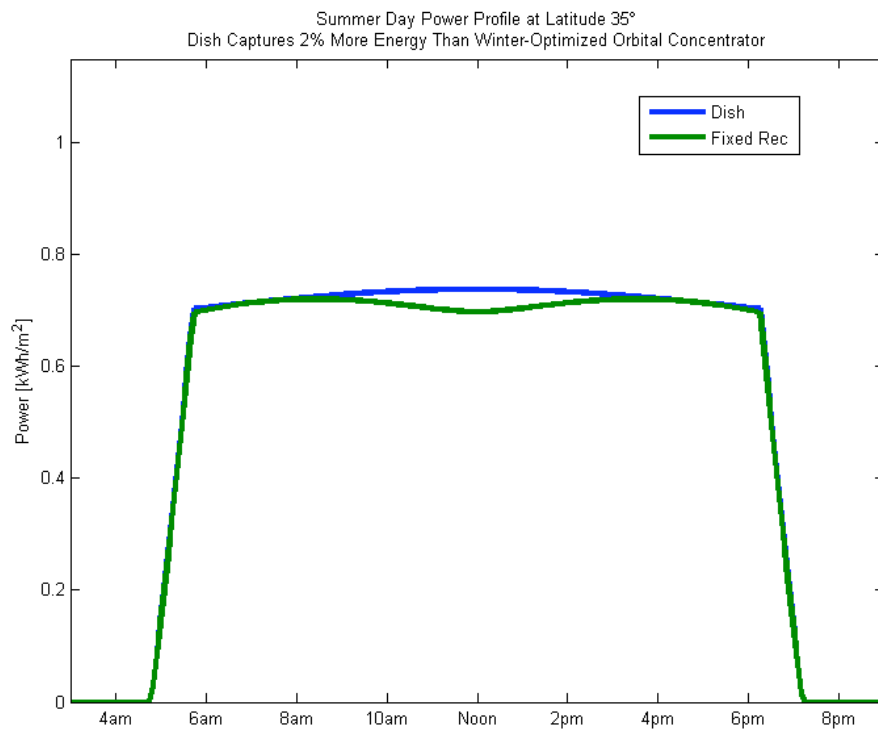
(b)

Figure 4.5: Orbital Concentrator (a) tracking motion and (b) comparison of summer day power output versus dish

movement while transporting hot and potentially high pressure fluids, and are known to be a primary failure point of many dish and trough systems, including the SEGS plants. These complications have led most dish implementations to use self-contained systems (typically Stirling engines or CPV modules) for electricity production, avoiding the need for these joints but restricting CHP options.

Having a remote heat engine has many advantages over a focal-mounted engine (e.g. dish-Stirling) by decoupling the two components. Vibrational decoupling decreases fatigue on the structure, yielding longer life and lower cost, and increases tracking performance by reducing noise to the sensors. Decoupling of scale allows several smaller collectors to power one larger engine. Smaller collectors are more cost effective because they have significantly lower wind loads, can use off-the-shelf actuators, and are more ground-supported. Larger engines are lower cost per watt, more efficient, and have lower operational costs per kWh produced. There is also no need to suspend the weight of the entire thermal-electric system up in the air, further reducing structural costs.

Power towers have also been well explored, notably by BrightSource, Solar Two, and PS10. Just as in power-tower systems, the receiver and plumbing in the Orbital Concentrator are fixed, eliminating the complications of movable plumbing joints. Power-towers, however, have several disadvantages that are avoided by the Orbital Concentrator. They must be of very large scale in order to work efficiently, restricting CHP and distributed applications because they typically must be sited very far from energy loads. The heliostats suffer from moderate cosine losses, reducing material efficiency. The distance from reflector to receiver target is very large, reducing concentration factors and robustness to tracking and slope error. Towers are typically over 100 meters tall with the thermal-electric system located at the top, adding significant complexity and cost.

This novel Orbital Concentrator is highly conducive for low-cost mass production, rapid scale up, and ease of deployment by leveraging commodity materials, the existing manufacturing base, and off-the-shelf components. One of the historical challenges of building two-axis concentrators is the manufacture of the compound reflector surface. The Orbital Concentrator uses the technique of arraying single-axis reflector slats to form a hybrid Fresnel reflector surface, suitable for any number of reflector laminates such as flexed mirrored glass, metal sheeting (such as Miro by Alanod), or Mylar films (such as ReflecTech). It is unclear which of these reflector options is ideal, but the Orbital Concentrator will work with all of the above and testing could be done to select an ideal candidate for mass-production. Using flat reflector strips allows the compound structure to be assembled out of easily mass-produced reflector modules, sourced by existing manufacturing entities. The compound surface has a concentration ratio in the Fresnel direction on the order of the number of slats, whereas the flexed axis can achieve much higher concentration because of the continuous curvature. This combination is conducive to a short and wide configuration of a few long horizontal strips, and thus the final dimension can be matched for easy stacking and packing into standard shipping containers for efficient transportation to the deployment site.

There are of course trade-offs with the Orbital Concentrator compared to power-tower and dish systems, but they have been carefully balanced in consideration of the over-all system. For

example, the Orbital Concentrator cannot achieve concentration factors as high as high-fidelity dishes because it operates slightly off-axis for a portion of every day and has a hybrid Fresnel surface. Fortunately, higher concentration is only necessary for significantly higher temperatures, which are not the goal of this project because they increase costs significantly. Based on first-order engineering calculations, the Orbital Concentrator will be able to achieve 500x concentration, which is more than adequate to generate steam at over 75% efficiency and of the pressure and temperature needed to operate the Katrix expander effectively. Orbital Concentrators also suffer from slight cosine losses compared to dishes, but engineering analysis shown in Figure 4.5 indicates this loss is on the order of 2%. A worst-case comparison of the daily power profiles of a dish and Orbital Concentrator exhibits the highest instantaneous loss of about 6% when the sun is highest in the sky, but an average loss of about 2% over the course of the day. The final trade-off is that a smaller system has limited thermal-electric conversion efficiency compared to power-towers, but this is lost in favor of modular, distributed, CHP generation.

4.5.2   The Rankine cycle powering a Katrix rotary lobe expander

The second enabling technology for this DCS-CHP system is an efficient small-scale rotary lobe expander. As Aoun concludes in his thesis on the subject of residential solar CHP, volumetric expansion devices like Wankels, vane expanders, and screws/scrolls are the most promising for distributed applications (Aoun [1]). The problem with small expanders in general is that the power generated is proportional to the displaced volume, however many losses are proportional to the surface area (e.g. friction on moving seals/rings in positive displacement machines), so shrinking the expander size decreases the overall efficiency because volume is a function of the cube of the characteristic dimension, whereas surface area is a function of the square of that dimension. This effect is what makes Tesla turbines so interesting in small-scale in that they turn this relationship around since power is generated by viscous forces, dragging on the rotor, which actually increases (inversely to volumetric flow rate) as the size of the device is scaled down. Much work still needs to be done in improving Tesla turbines however, and it is unclear whether they will reach efficiencies in the useful realm for this application (Romanin et al. [30]), although some work has indicated it is possible they already have (Saitoh et al. [31]) . Aerodynamic turbines, even those used in the smallest scale commercial applications, radial inflow turbines, are also incompatible with the high pressure ratios and low power outputs needed for DCS-CHP (Sunter et al. [35]) .

That leaves screw, scroll, piston, vane, and rotary lobe expanders (e.g. Wankel). Of those, screw and scroll expanders exhibit modest performance in small-scale (Aoun [1]), and pistons show good performance, but at the cost of more complex valves and more moving parts than rotary lobe expanders. Vane expanders have not been explored thoroughly in this research but may suffer from lower efficiencies than other volumetric devices at high pressure ratios (Aoun [1]). For those reasons the rotary lobe expander appears nearly ideal for DCS-CHP if good pressure ratios and performance can be achieved with the desired working fluid.

The current generation Katrix expander was experimentally verified to provide an 8:1 pressure expansion ratio at greater than 80% isentropic efficiency, as reported in Chapter 3. This technology, originally developed for waste heat applications with funding from the Australian

government and private sources, will need to be optimized for use in the DCS system, but should provide greater than 20 years of reliable operation in the 10 bar and 200-250 °C operating condition range. This device is in a new class of positive displacement machines that uses Limaçon motion to enable high expansion ratios, high torque, and low-speed operation in a compact package.

To choose an appropriate working fluid and components for a DCS-CHP system, we compared many different working fluids, collectors, and expander choices. Of the possibilities analyzed, including piston expanders, radial inflow turbines, Tesla turbines, screw expanders and scroll expanders, the rotary lobe expander shows the greatest promise in small scale power applications due to its high efficiency in expanding fluids over large pressure ratios and its low-cost to manufacture. Because the typical heating load in many facilities is on the same order as the electrical load, increasing the fraction of electrical to heat output of the system is desirable. Thermodynamic modeling in Engineering Equation Solver (EES) and Matlab has shown that an efficient large pressure ratio expansion for a Rankine cycle is crucial for getting theoretical solar-electric efficiencies as high as possible, and thereby increasing the relative fraction of electricity to heat produced by the cycle.

Sunter et al. modeled a variety of working fluids in the analysis of radial inflow turbines for Solar CHP (Sunter et al. [35]). As that paper concludes, there are not any suitable working fluids that would exhibit desirable properties for use in dry or wet expansion, that don't also either exhibit high global warming potential (R123, R134, R245FA, etc.) or are highly toxic (Toluene, methanol, etc.). Aoun came to the conclusion (in his very comprehensive thesis devoted to residential solar CHP systems) that in terms of both heat transfer properties and maximum efficiency at higher expansion ratios water is the preferred choice.

At temperatures above 150°C as provided by a tracking concentrating solar collector, water is a remarkable working fluid choice that is ubiquitous, safe, environmentally benign, and well-suited to CHP systems because its saturation temperature at atmospheric pressure (100 °C) is good for process heat, DHW, and other thermal heating and cooling demands. Considering organic working fluids such as alcohols, refrigerants, pentane, etc. the author has found that the relative performance of these fluids is only better than water for Rankine cycles in lower temperature regimes, or electricity-only cycles (non-CHP). In addition, the added manufacturing, greenhouse gas and ozone depletion factors, safety concerns (flammability, toxicity, etc.), and cost make these fluids less desirable for a DCS-CHP system.

4.5.3 Results of simulating a Katrix expander, dish collector DCS-CHP system

System optimization is challenging due to the fact that the combined performance of the collector, turbine, and steam accumulator are dependent on widely varying environmental conditions. Choosing components that interact well with each other requires advanced system modeling. The DCS-CHP simulation software described earlier in this chapter is able to model the performance of each component as they interact with the system as a whole incorporating location-based
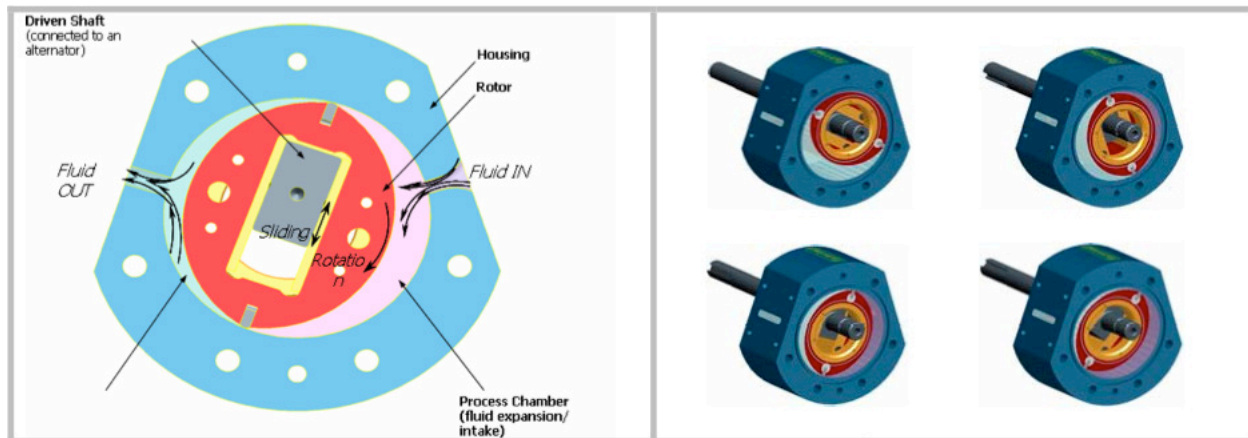
Figure 4.6: Stages in the Katrix expansion cycle

insolation and weather data. Achieving direct steam generation in the receiver with varying levels of sunlight and potentially low-flow rates of steam will require a robust control scheme. The system should be optimized for not only peak times, but must respond well to intermittent clouds, low light levels, and periods of darkness. Throughout the design process, the primary metric for optimization has been full system life-cycle cost and environmental analysis, considering materials, manufacturing, installation, operation, and decommissioning.

Figures 4.7, 4.8, 4.9 and 4.10 show expected output for a dish system with a steam Rankine cycle with a Katrix expander and 8:1 pressure ratio at all 1020 United States locations in the NREL TMY3 data. Electrical and heat data are plotted in units of kWh per square meter of collector aperture. The specifics of this system, shown in Figure 4.3, are chosen as realistic expectations for an actual installed system, and are the same used in Chapter 2 . Specifically, the experimentally measured Katrix efficiency and expander pressure ratio results using air as the working fluid (Chapter 3) are used as a performance estimate when operating with steam. No dynamic similitude analysis was performed to predict operation on steam from the air testing results, so results should only be considered an approximation. Because the temperatures and pressures were exactly the same as expected operation on steam, and because we did not have permission to access the internal geometry of the expander to assess Reynolds, Prandtl, Mach or other non-dimensional parameters related to the working fluid choice, this rough estimate should suffice until further testing is done on the next generation Katrix expander. A caveat to operation of the current expander with steam is that special lubrication (steam oil) would have been required. In the future, design changes to bearings could be explored to achieve a condensate-lubricated expander instead of one that is oil lubricated. Such a design would be well worth it, in the author's opinion, as it would greatly enhance the expanders utility in moderate temperature steam Rankine cycles such as these by both eliminating a possible source of failure (i.e. oil lubrication system failure), and preventing lubricant from being mixed with the working fluid. This latter benefit of a steam-lubricated expander would enable use of a single-loop Rankine cycle without oil separation thereby minimizing cost without sacrificing system efficiency.

Simulation results of a typical meteorological year of operation in Oakland, CA are shown in

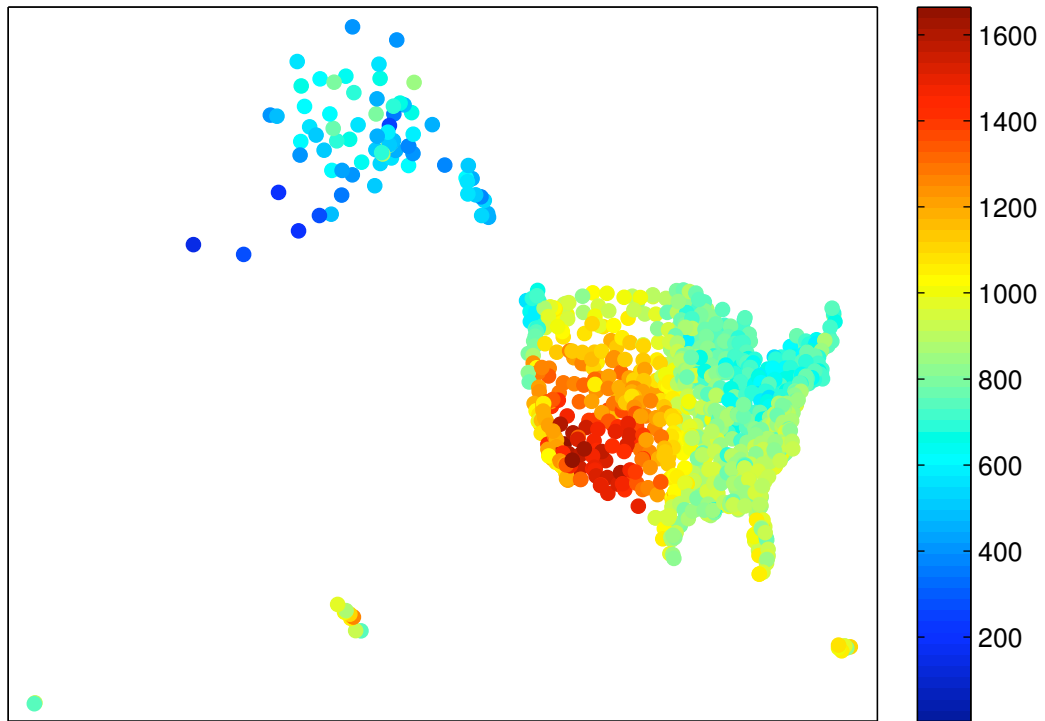Figure 4.7: Katrix-Dish system yearly heat output (scale is kWh thermal per m^2 of collector aperture)
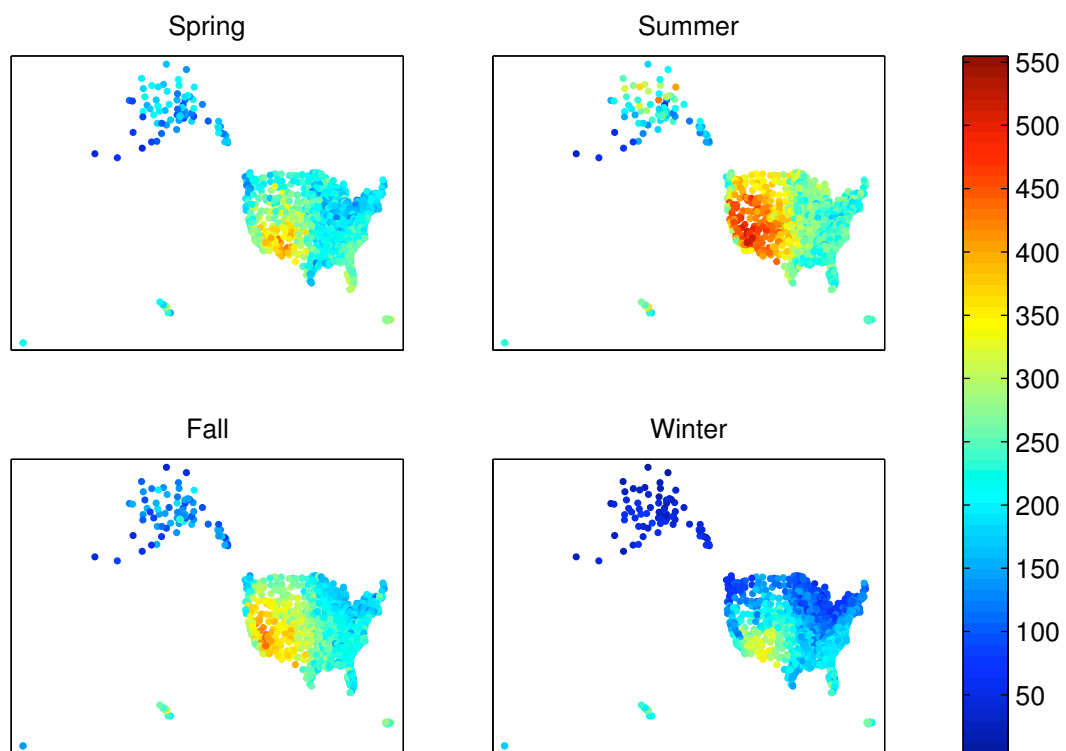
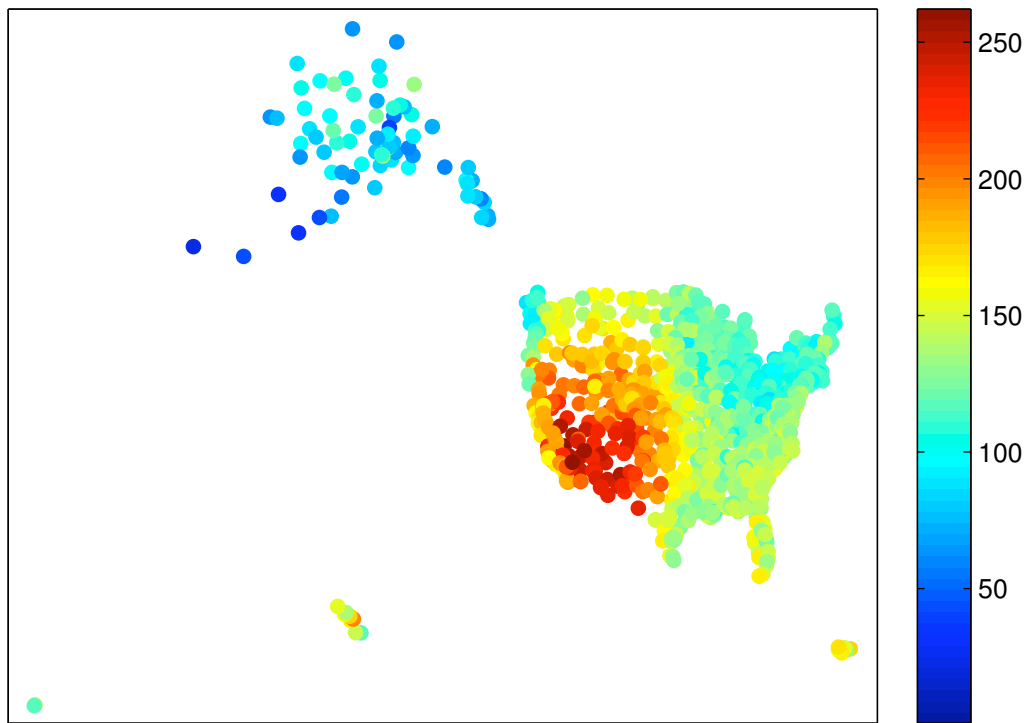Figure 4.8: Katrix-Dish system seasonal heat output (scale is kWh thermal per m^2 of collector aperture)

Figure 4.9: Katrix-Dish system yearly electrical output (scale is kWh electric per m^2 of collector aperture)
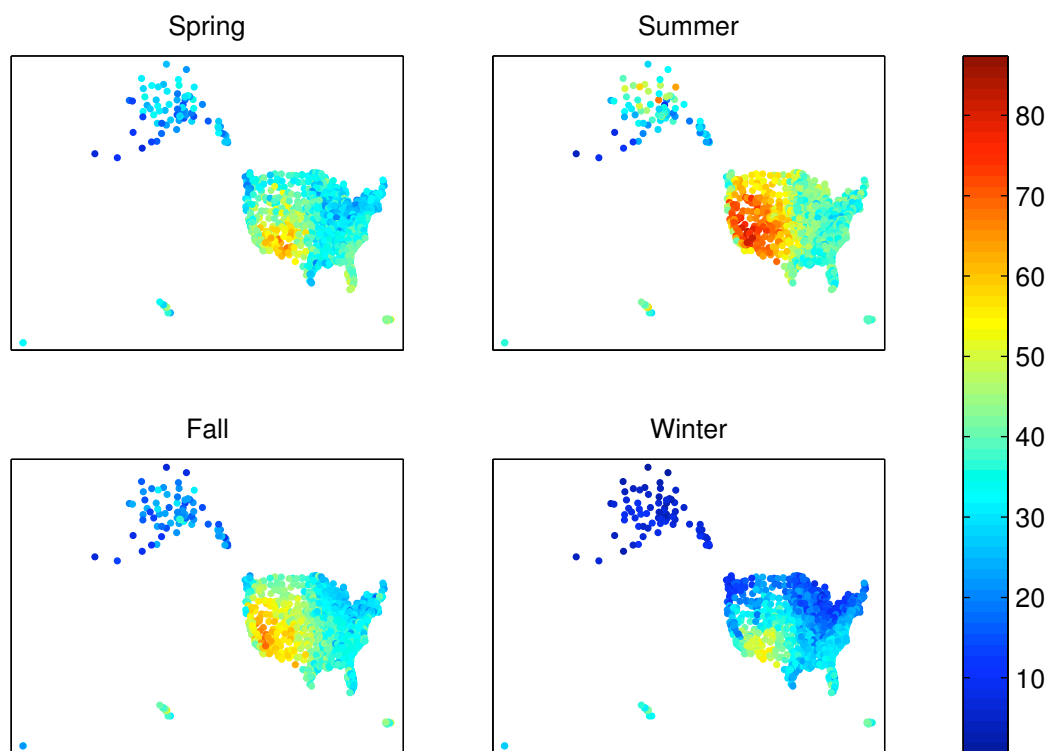
Figure 4.10: Katrix-Dish system seasonal electrical output (scale is kWh electric per m^2 of collector aperture)

Parameter	Value
Solar-thermal efficiency	0.58
Solar-electric efficiency	0.09
Fraction of Carnot efficiency achieved in Rankine cycle	0.53
Total yearly heat generated (kWh per m^2 collector aperture)	970
Total yearly electricity generated (kWh per m^2 collector aperture)	150

Table 4.1: Results of the simulated output of the Katrix expander, dish collector system in Oakland, CA as used in the LCA analysis of Chapter 2

Table 4.1. Note that these results combined with the cost modeling results of Chapter 1 indicate such a system could simultaneously achieve 9% solar-electric efficiency and 58% solar-to-useful-heat efficiency at competitive costs to existing small-scale dedicated solar-thermal or solar-electric systems. Because the same solar array would be used for each system, the total collector area would be reduced by about one half compared to a typical PV and thermal system providing the same output. To demonstrate this, consider that a 9% efficient solar-electric system (typical for thin-film panels currently) plus a 58% efficient solar-thermal system (flat-plate efficiency would actually be much less for the modeled 100ºC usable heat from a DCS-CHP system) would take up exactly twice as much land area as the proposed solar CHP system. This higher land area density makes this technology suitable for urban and rural areas, especially if building integrated.

4.6   Potential impact

There are currently two primary technologies for solar-electric energy conversion: photovoltaics which utilize the photo-electric effect for direct conversion of light to electricity, and solar thermal technologies that collect light as heat, typically driving mechanical-electrical generators. Solar Combined Heat and Power (CHP) systems convert sunlight to both heat and electricity. This research focuses on Distributed Concentrating Solar Combined Heat and Power (DCS-CHP) for the following reasons: (a) DCS-CHP has the potential for more than 70% solar-thermal conversion efficiency at temperatures in excess of 200°C. (b) Electricity is currently very difficult to store economically; while energy in the form of heat can be cost-effectively stored with available technologies. (c) DCS-CHP thus can ameliorate grid-balancing problems caused by temporal differences between renewable energy peak generation and peak demand. (d) DCS-CHP technology can be manufactured using abundant and easily processed engineering materials including steel, aluminum, and glass.

As outlined in the 2005 Dept. of Energy publication "Basic Research Needs for Solar Energy Utilization," moderate temperature distributed solar thermal is an area where there is potential for significant cost-reducing innovation. Thermal demands, including space heating and cooling, are a large fraction of total energy demands for small facilities (e.g. greater than 50% of energy demands for California households are thermal).

The value proposition for Distributed Generation (DG) compared to centralized generation favors DG for several reasons: (a) The price for DG compares to electricity and natural gas (or fuel oil) at retail cost, not wholesale cost, as consumers will be producing electricity and displacing natural gas (or fuel oil) at the site of end-use. The retail cost of electricity is approximately 100% higher than wholesale, giving DG this considerable advantage. (b) DCS-CHP is capable of efficiently offsetting domestic demands for heating and cooling, unlike utility scale systems, which are not located in close enough proximity to end-users to take much advantage of the rejected waste heat from power generation. (c) Electrical transmission concerns are alleviated because power is being generated at or near the point of use, where existing transmission infrastructure often already exists.

The combined advantages of distributed generation and solar-thermal CHP have the potential to make this a transformative technology. Solar PV, wind, geothermal, and hydropower are currently the leading technologies for distributed renewable power generation; however several barriers prevent these technologies from being ubiquitous. Local environmental resources limit wind, geothermal, and hydropower; while solar energy is nearly universally available, although in varying amounts. Photovoltaics are functional in a much wider range of environments, however the scarcity of required materials, lower efficiencies, and the complexity of manufacturing make them costly and impractical for rapid and universal adoption. DCS-CHP has the advantage of using solar energy while overcoming the manufacturing difficulties of photovoltaics, giving it a potential for deep market penetration of renewable distributed energy generation. Additionally, the ability to create both heat and power, adjustable on demand, allows the proposed system to offset imports from foreign fossil fuel sources (e.g. natural gas and fuel oil), and also greatly impact regional GHG emissions from electricity production (e.g. coal power plants).

According to the Energy Information Administration's 2007 Annual Energy Review, fossil fuels (including petroleum) in the commercial, industrial, and residential sectors account for more than half of the total energy used in the United States, with transportation accounting for less than 30% of this. Because DCS-CHP targets both heat and power generation in buildings, it has the ability to reduce fossil fuel usage dramatically.

A Life Cycle Assessment of DCS-CHP has been conducted in order to select low-cost, non-polluting and widely available materials. The calculated greenhouse gases emitted from electricity produced by DCS-CHP is 5 to 10 times lower than that same unit of electricity typically consumed in the United States, and the ease of recycling the DCS-CHP system further reduces GHG emissions at the end of the product's life. This result lies in the same emission range as other renewable energy technologies in solar thermal and PV, and ensures that as the demand in DCS-CHP increases prices will not fluctuate due to material scarcity or an increased cost of carbon emissions. The levelized cost of energy generated by the DCS-CHP system over its lifetime is estimated to be $0.25/kWh electric, and $0.03/kWh of a 100ºC heat source, or $3.20/W electric and $0.40/W thermal based on installed capital cost per peak power output. The LCA of the system affirms that small scale solar combined heat and power systems can directly compete with other renewable energy systems and have comparable environmental impacts to PV systems.

The proposed DCS-CHP system, in the 1-10 kW peak electric range, will be appropriate for small residential communities or single households with reasonable land area. Commercial and

industrial applications could be served by a solar orchard, consisting of many solar dishes arrayed on rooftops, above parking lots, or in open fields, hillsides, etc. For congested areas, this district system can supply heat and power to local residences or businesses. Although it may seem that the decreased efficiency of solar-electric conversion, for a distributed system (~10%) as compared to a centralized CSP plant (>20%), would decrease efficiency of the energy generation sector as a whole, this is not the case. First, the heat generated by this system, if put to use displacing fossil fuels would more than make up for the decreased solar-electric efficiency, especially when comparing relative GHG intensities. Secondly, distributed generation effectively bypasses many of the hurdles found in siting and permitting other renewable energy generation technologies or transmission lines, which limit the speed at which fossil fuel generation can be replaced. Also, the number of green jobs created by a DG technology is greater than that of a centralized technology due to the increased labor force needed to install, maintain, and operate many small systems, as compared to a typical large central generation plant. And lastly, although oft overlooked, distributed energy generation technology promotes democracy in energy choices by putting the generation equipment in the hands of the consumer instead of the corporations that typically control centralized energy generation.

Bibliography

[1] Aoun, B. (2009, May). Micro combined heat and power operating on renewable energy for residential building. Ph. D. thesis, Ecole Doctorale 432 Sciences des Métiers de l'Ingénieur.

[2] Appropedia (2011, April). Levelised cost of electricity literature review. http://www.appropedia.org/.

[3] Blevins, R. (2003). Applied fluid dynamics handbook. Krieger Pub.

[4] Casten, T. R. and R. U. Ayres (2007). Energy myth eight – worldwide power systems are economically and environmentally optimal. In Energy and American Society – Thirteen Myths. Springer Netherlands.

[5] Çengel, Y. A. and M. A. Boles (2006). Thermodynamics: an engineering approach (5 ed.). McGraw-Hill Higher Education.

[6] El-Dessouky, H. T., H. M. Ettouney, and F. Mandani (2000). Performance of parallel feed multiple effect evaporation system for seawater desalination. Applied Thermal Engineering 20(17), 1679 – 1706.

[7] Gleick, P. H. (1994). Water and energy. Annual Review of Energy and the Environment 19(1), 267–299.

[8] Hansen, J., M. Sato, P. Kharecha, D. Beerling, R. Berner, V. Masson-Delmotte, M. Pagani, M. Raymo, D. Royer, and J. Zachos (2008). Target atmospheric CO2: Where should humanity aim? Open Atmospheric Science Journal 2, 217–231.

[9] Hendrickson, C., A. Horvath, S. Joshi, M. Klausner, L. Lave, and F. McMichael (1997, May). Comparing two life cycle assessment approaches: a process model vs. economic input-output-based assessment. In Electronics and the Environment, 1997. ISEE-1997., Proceedings of the 1997 IEEE International Symposium on, pp. 176–181.

[10] IEEE (2009). IEEE application guide for IEEE std 1547, IEEE standard for interconnecting distributed resources with electric power systems. IEEE Std 1547.2-2008, 1 –207.

[11] Kalogirou, S. (1997). Survey of solar desalination systems and system selection. Energy 22(1), 69 – 81.

[12] Kalogirou, S. A. (2004). Solar thermal collectors and applications. Progress in Energy and Combustion Science 30(3), 231 – 295.

[13] Kalogirou, S. A. (2005). Seawater desalination using renewable energy sources. Progress in Energy and Combustion Science 31(3), 242 – 281.

[14] Lenzen, M. (2008). Life cycle energy and greenhouse gas emissions of nuclear energy: A review. Energy Conversion and Management 49(8), 2178 – 2199.

[15] Lewis, N. S., G. Crabtree, A. J. Nozik, M. R. Wasielewski, P. Alivisatos, H. Kung, J. Tsao, E. Chandler, W. Walukiewicz, M. Spitler, R. Ellingson, R. Overend, J. Mazer, M. Gress, J. Horwitz, C. Ashton, B. Herndon, L. Shapard, and R. M. Nault (2005, April). Basic research needs for solar energy utilization. Technical report, US DOE - Office of Basic Energy Sciences.

[16] Mahjouri, F. (2004). Vacuum tube liquid-vapor (heat-pipe) collectors. Proceedings of the ASES Solar 2004 Conference.

[17] Mathworks (2011, March). http://www.mathworks.com/help/techdoc/ref/std.html.

[18] Mills, D. (2004). Advances in solar thermal electricity technology. Solar Energy 76(1-3), 19 – 31. Solar World Congress 2001.

[19] Montgomery, Z. (2009, December). Environmental impact study: CSP vs. CdTe thin film photovoltaics. Master's thesis, Duke University.

[20] Müller-Steinhagen, H. (2004). Durability, reliability and performance of a solar collector. Technical report, University of Stuttgart.

[21] Norwood, Z., N. Kamphuis, and D. Soltman (2006, December). Distributed solar-thermal/electric generation. Technical report, University of California at Berkeley, CA (US).

[22] Norwood, Z., T. Lipman, M. Stadler, and C. Marnay (2010). Assessment of combined heat and power "premium power" applications in California. International Journal of Distributed Energy Resources 6(2), 131–147.

[23] Norwood, Z., S. Pepe, V. Romanin, and D. Kammen (2010). Performance-cost analysis of solar combined heat and power systems. ASME Conference Proceedings 2010(43956), 27–34.

[24] Pehnt, M. (2006). Dynamic life cycle assessment (LCA) of renewable energy technologies. Renewable Energy 31(1), 55 – 71.

[25] PG&E (2010, December). Pacific gas and electric rule no. 21: Generating facility interconnections.

[26] Price, H., E. Lupfert, D. Kearney, E. Zarza, G. Cohen, R. Gee, and R. Mahoney (2002). Advances in parabolic trough solar power technology. Journal of Solar Energy Engineering 124(2), 109–125.

[27] RawSolar (2009, June). http://www.raw-solar.com/.

[28] Reich-Weiser, C., S. Horne, and D. A. Dornfeld (2008). Environmental metrics for solar energy. Technical report, University of California at Berkeley, Laboratory for Manufacturing and Sustainability.

[29] REN21 (2009). Renewables global status report: 2009 update. Technical report, Renewable Energy Policy Network for the 21st Century.

[30] Romanin, V., V. P. Carey, and Z. Norwood (2010). Strategies for performance enhancement of Tesla turbines for combined heat and power applications. ASME Conference Proceedings 2010(43956), 57–64.

[31] Saitoh, T., N. Yamada, and S.-i. Wakashima (2007). Solar Rankine cycle system using scroll expander. Journal of Environment and Engineering 2(4), 708–719.

[32] Spencer, L. (1989a, January). A comprehensive review of small solar-powered heat engines part II: Research since 1950-conventional engines up to 100kW. Solar Energy 43(4), 197–210.

[33] Spencer, L. (1989b, January). A comprehensive review of small solar-powered heat engines. part III: Research since 1950-unconventional engines up to 100 kW. Solar Energy 43(4), 211–225.

[34] Stoppato, A. (2008). Life cycle assessment of photovoltaic electricity generation. Energy 33(2), 224 – 232. 19th International Conference on Efficiency, Cost, Optimization, Simulation and Environmental Impactof Energy Systems - ECOS 2006.

[35] Sunter, D. A., V. P. Carey, and Z. Norwood (2010). Radial inflow turbine assessment for small-scale concentrated solar Rankine combined heat and power technology. ASME Conference Proceedings 2010(43956), 45–56.

[36] Swamy, M. (2005). Passive techniques for reducing input current harmonics. Technical report, Yaskawa Electric America, Inc.

[37] Thomas, K. E. (1997, April). Overview of village scale, renewable energy powered desalination. Technical Report NREL/TP–440-22083, National Renewable Energy Lab., Golden, CO (United States).

[38] UNESCO (2010, December). Valuing water. http://www.unesco.org/.

[39] USDOE. Concentrating solar power commercial application study: Reducing water consumption of concentrating solar power electricity generation. Technical report, Report to Congress.

[40] Wade, N. M. (1999). Energy and cost allocation in dual-purpose power and desalination plants. Desalination 123(2-3), 115 – 125. Selected papers presented at The WSTA Fourth Gulf Water Conference.

[41] Weisman, A. (2008). <u>Gaviotas: a village to reinvent the world</u>. White River Junction, VT: Chelsea Green Pub. Co.

[42] Weiss, W., I. Bergmann, and R. Steizer (2009, May). Solar heat worldwide: Markets and contribution to the energy supply 2007. Technical report, International Energy Agency Solar Heating and Cooling Programme.

[43] WHO and UNICEF (2010). Progress on sanitation and drinking-water: 2010 update.

[44] Wiser, R., G. Barbose, and C. Peterman (2009, February). Tracking the sun: The installed cost of photovoltaics in the U.S. from 1998-2007. Technical Report LBNL-1516E, Ernest Orlando Lawrence Berkeley National Laboratory, Berkeley, CA (US).

Chapter 5

Appendix A: Katrix Testing Equipment and Data

5.1 Test equipment

This is a list of the main test equipment, including sensors' make and model used in testing the Katrix expander:

- Upstream pressure transducer: Omega PX26-250GV

- Downstream pressure transducer: Omega PX181-300G5V

- Differential (Orifice) pressure transducer: Cole Parmer EW-68071-56

- Orifice Plate Flow Meter: Dwyer TE-D-1 with Omega PS-4G series pressure snubbers on both pressure ports

- Upstream thermocouple: Omega TJ36-CAXL-18G-6

- Downstream thermocouple: Omega TJ36-CAXL-18G-6

- Torque transducer: Interface T8-50-A4A

- Variable frequency drive: Yaskawa V-1000 Series CIMR-VU2A0056FAA with Yaskawa braking resistor pack URS-000140

- Induction motor: Leeson G150006.60

- Thermocouple DAQ board: National Instruments USB-9211

- Voltage DAQ board: National Instruments USB-6210

- 12V Power supply for all sensors: Acme Electric DMP1-120125

- Computer and data logging software: Dell Dimension 4600 with LabView Signal Express

- Rotameter: Fisher & Porter (ABB) 1" tube FP-1-35-G10 with float FP-1-GNSVGT-64A

The rotameter was calibrated at the average upstream air pressure and temperature in each test run, using the ABB provided calibration software. An example of this calibration scale is shown in Fig. 5.1.

5.2 Katrix measured data from test runs

The following graphs show the raw data collected from the test runs reported.

Sizing Record

Flow Table:			Reading:	m3/min:
Tube:	FP-1-35-G-10		100%	.315
Float:	FP-1-GNSVGT-64A		90%	.2835
			80%	.252
			70%	.2205
Fluid:	Air		60%	.189
Qv.req:	.314	m3/min	50%	.1575
			40%	.126
Dens 0°C:	1.293	kg/m3	30%	.0945
Viscosity:	0.0181	cP	20%	.063
			10%	.0315
Press(a):	900000	Pa		
Temp:	35	Deg C		
Dens:	10.18	kg/m3		
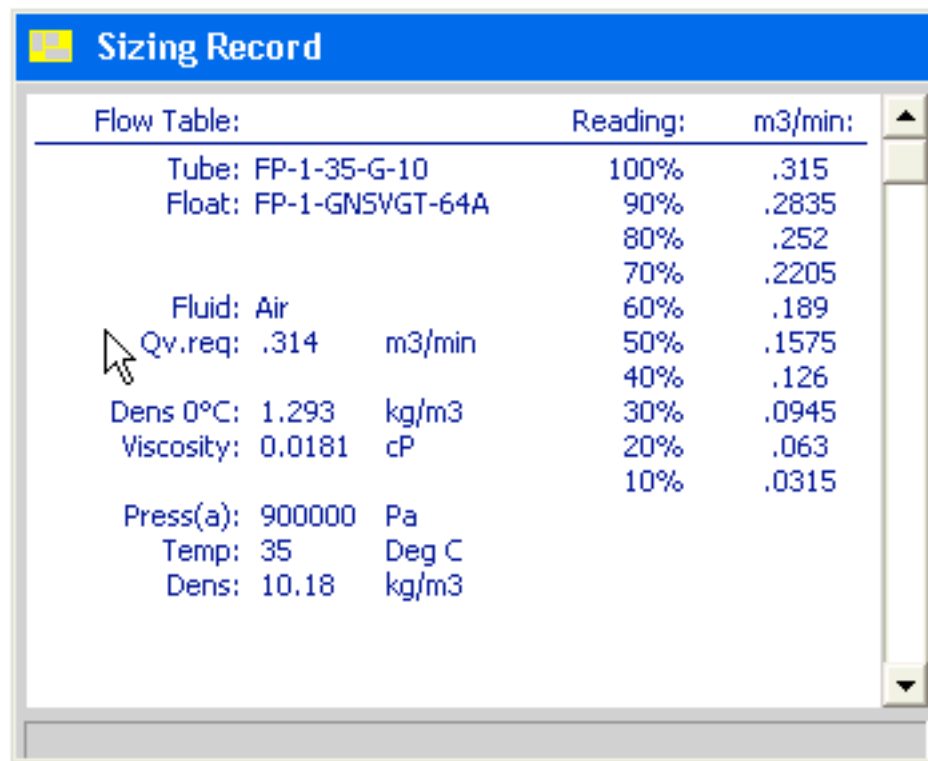
Figure 5.1: Rotameter calibration scale for air at 9 bar absolute pressure and 35ºC

Figure 5.2: Measured data from Katrix at 31.4 rad/sec set point, 300 second interval

Figure 5.3: Measured data from Katrix at 47.1 rad/sec set point, 300 second interval

Figure 5.4: Measured data from Katrix at 78.5 rad/sec set point, 300 second interval

Figure 5.5: Measured data from Katrix at 94.2 rad/sec set point, 300 second interval

Figure 5.6: Measured data from Katrix at 110.0 rad/sec set point, 300 second interval

Figure 5.7: Measured data from Katrix at 125.7 rad/sec set point, 300 second interval
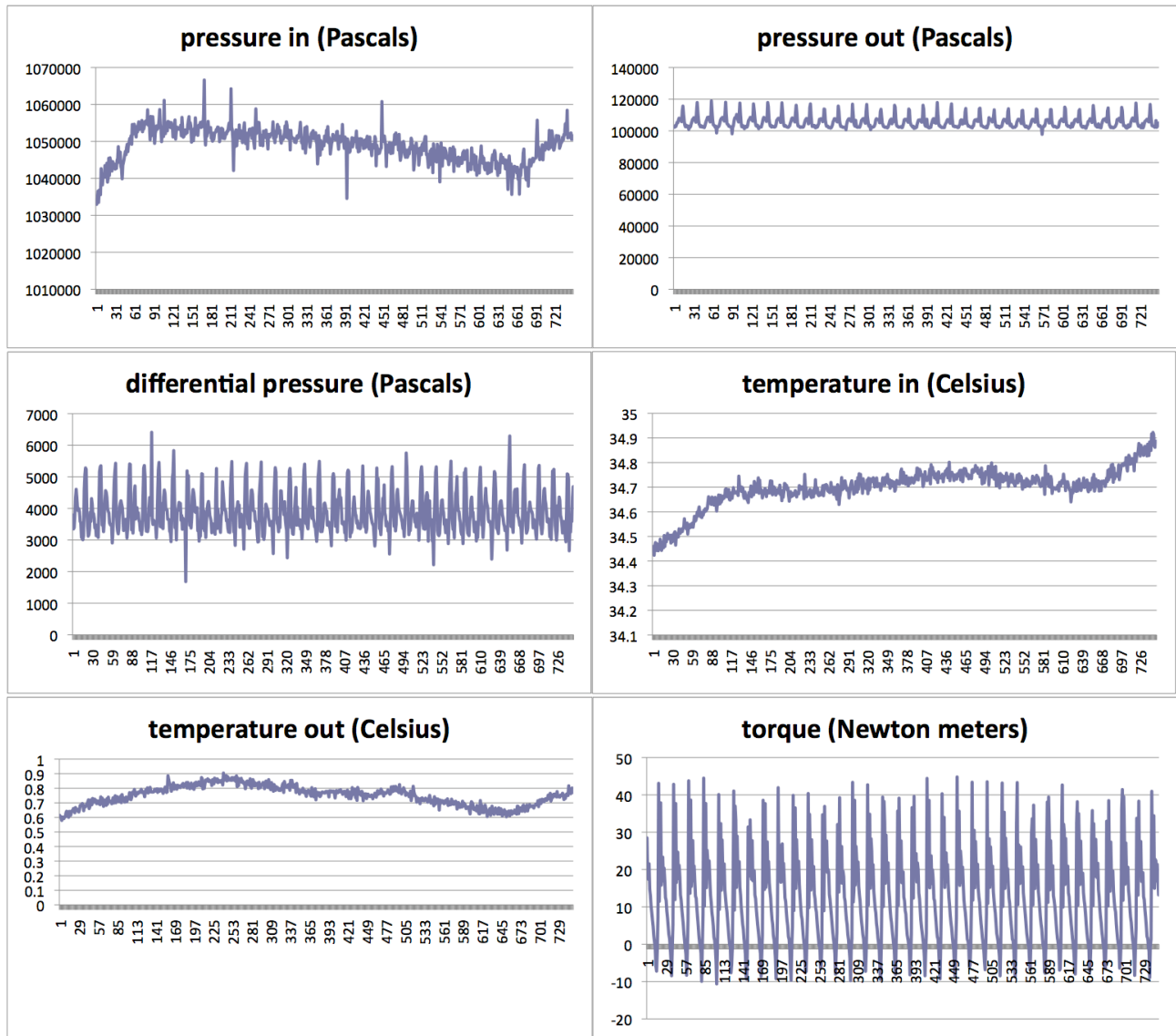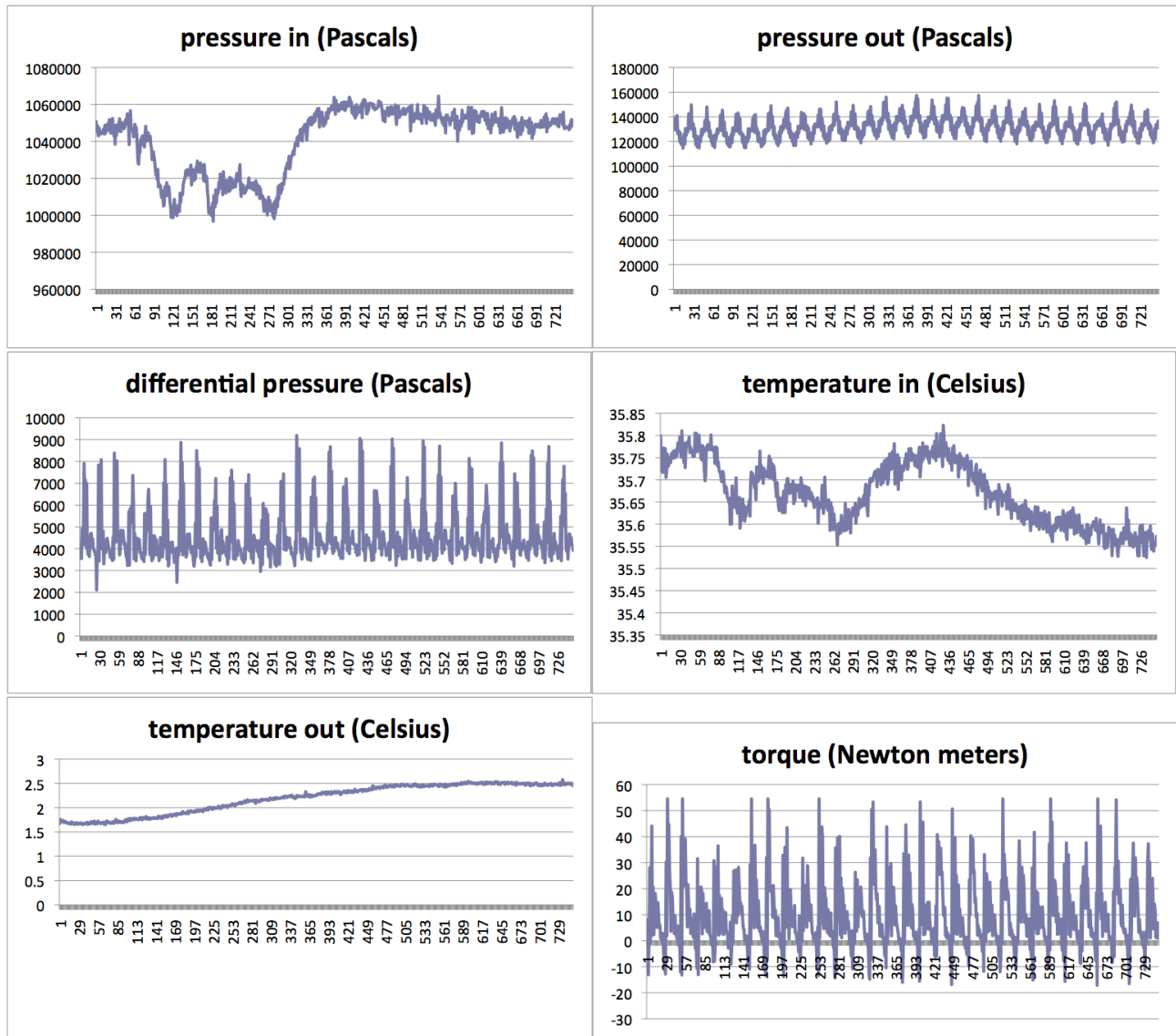
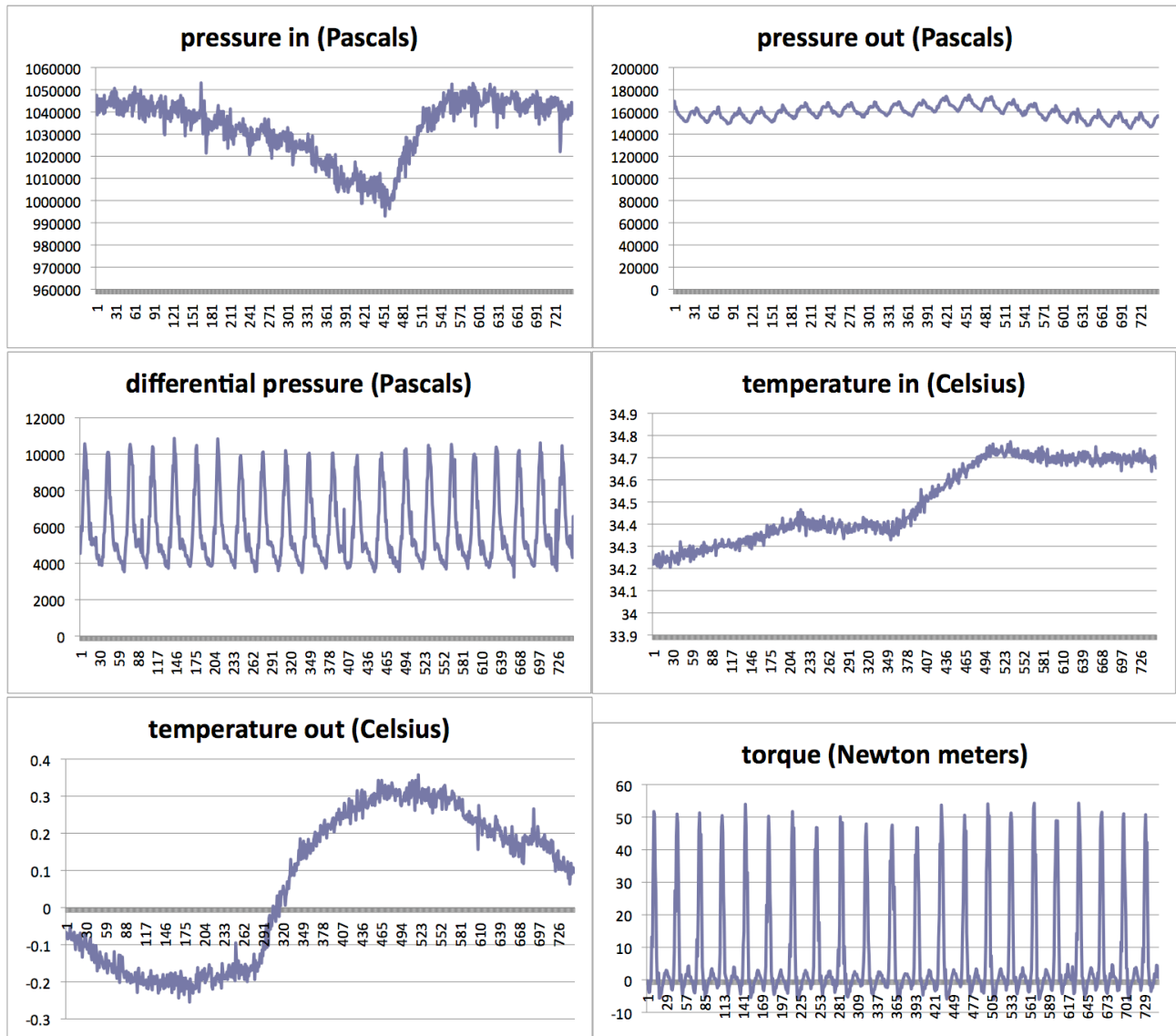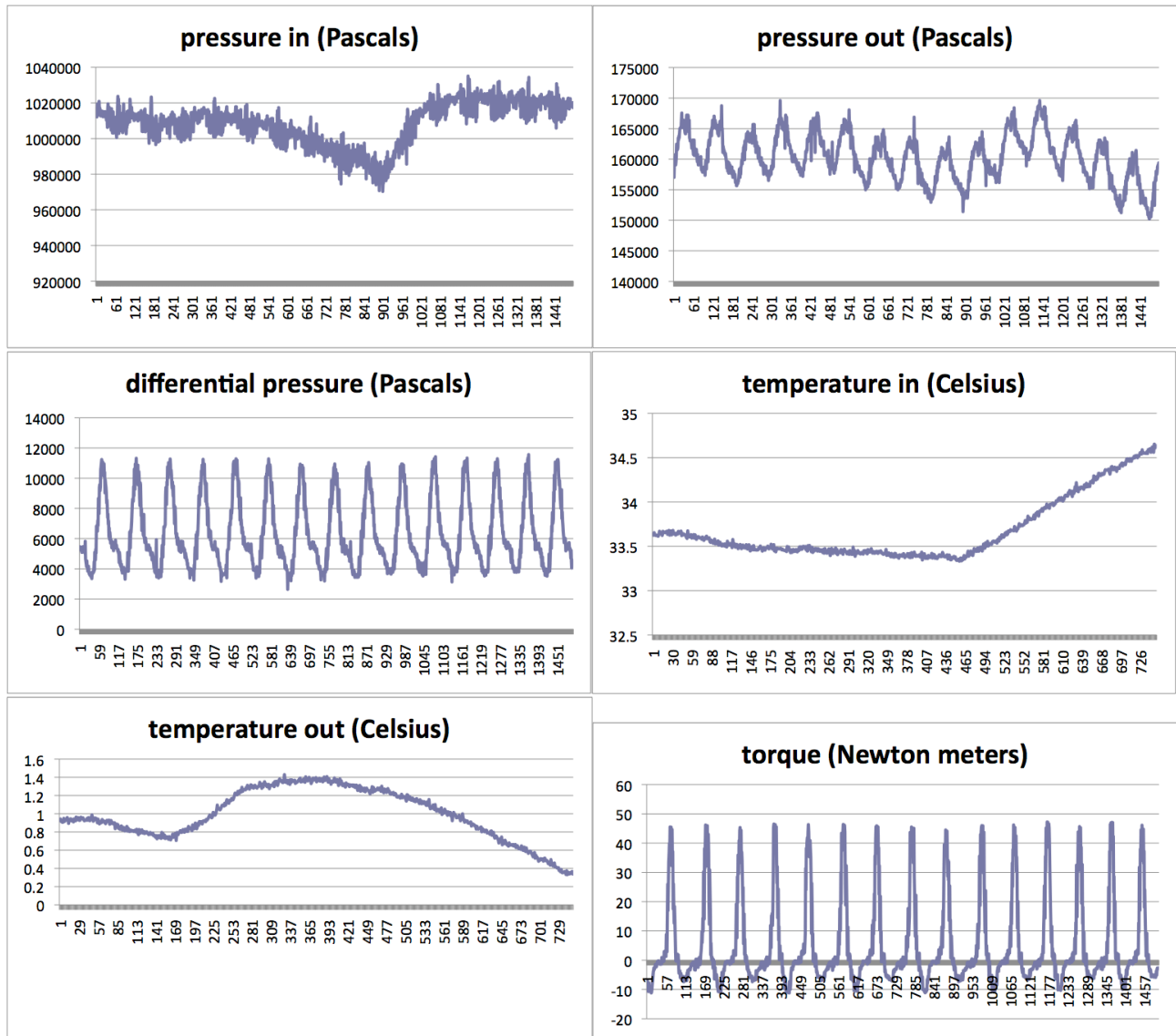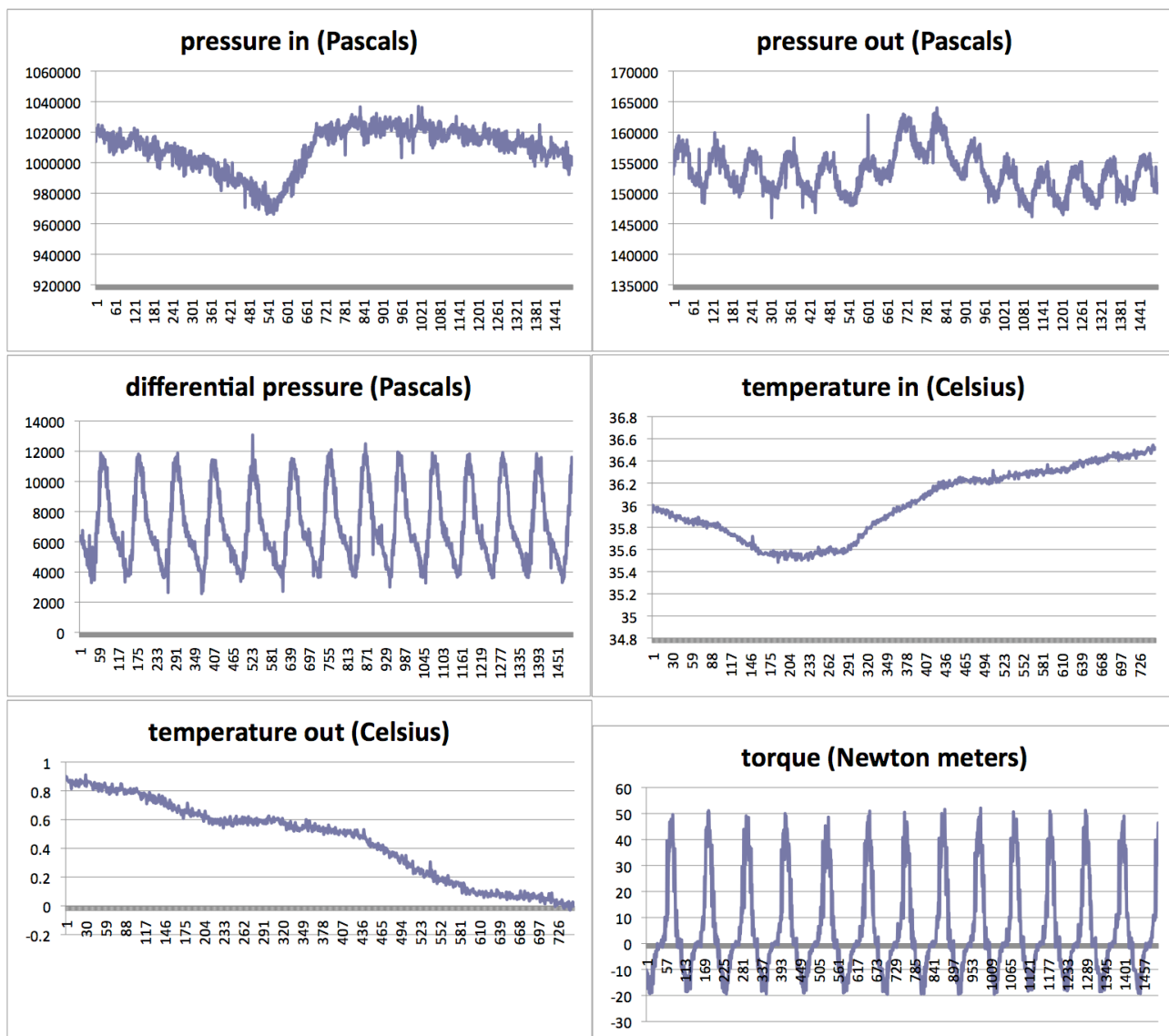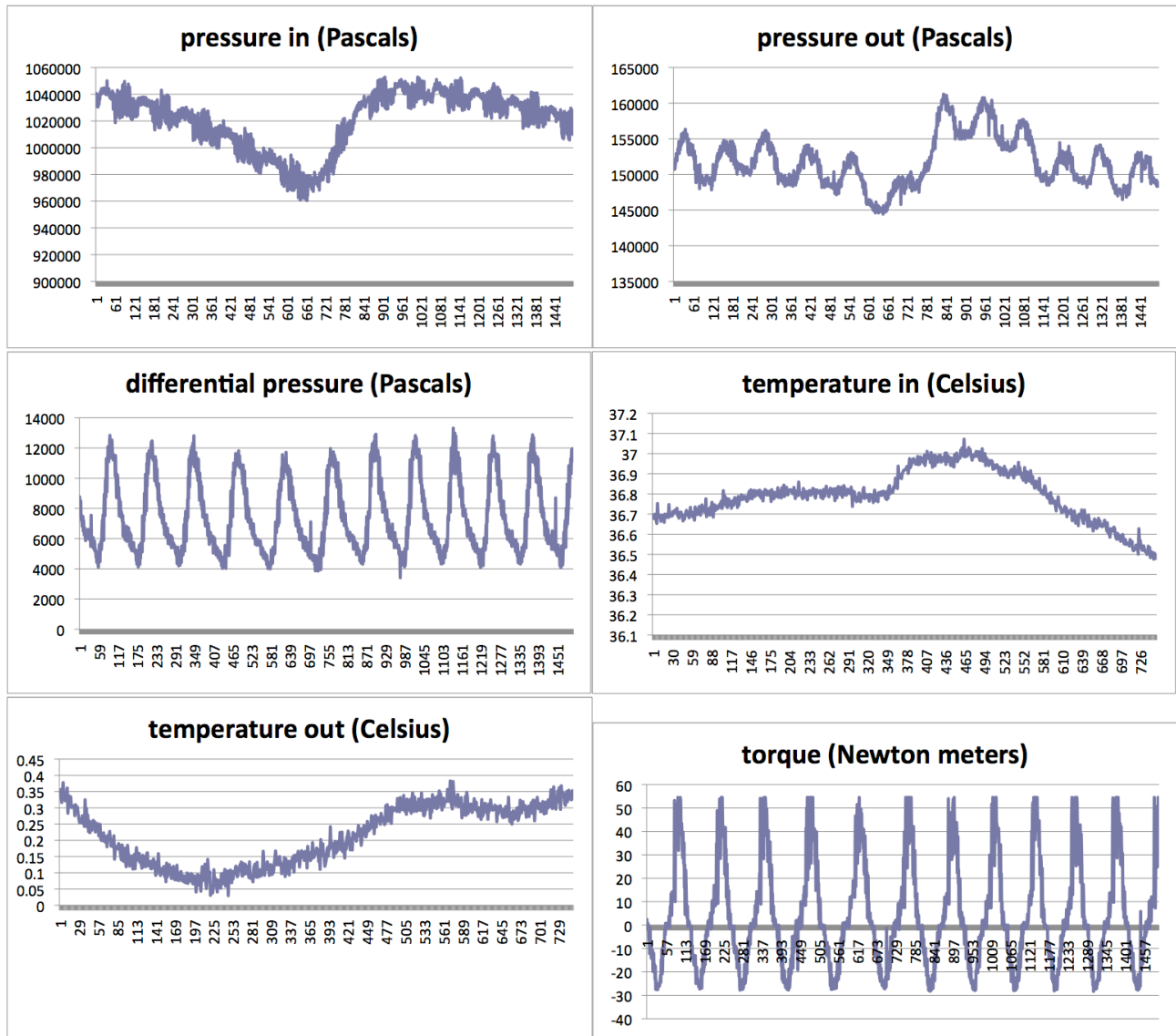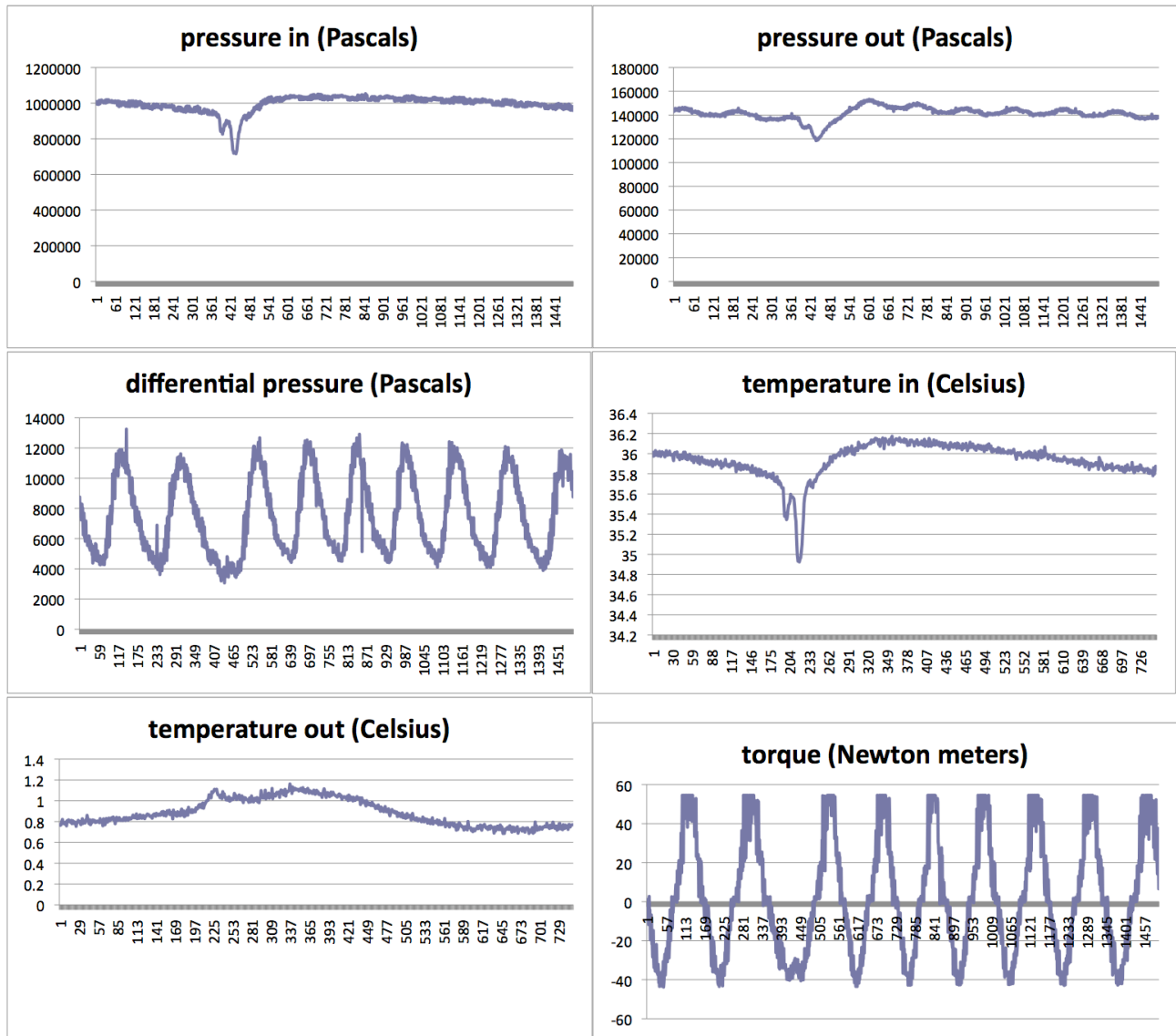Figure 5.8: Measured data from Katrix at 141.4 rad/sec set point, 300 second interval

Chapter 6

Appendix B: Matlab Code for Katrix Data Processing

6.1 katrixDataProcess.m

```
% katrix data processing
close all;
clear all; clear classes;
[efficiencyOrifice10 aveDensity10 avePin10 aveTin10 avePout10 aveTout10
aveTorque10 aveShaftPower10 aveSpecificEnthalpy10 aveFluidPowerOrifice10
aveMassFlowOrifice10] =
orificeKatrixEfficiency('matlab-10hz.xls',10,60,1800,'Air_ha',0.01016,0.29);
    [efficiencyOrifice15 aveDensity15 avePin15 aveTin15 avePout15 aveTout15
aveTorque15 aveShaftPower15 aveSpecificEnthalpy15 aveFluidPowerOrifice15
aveMassFlowOrifice15] =
orificeKatrixEfficiency('matlab-15hz.xls',15,60,1800,'Air_ha',0.01016,0.29);
    [efficiencyOrifice25 aveDensity25 avePin25 aveTin25 avePout25 aveTout25
aveTorque25 aveShaftPower25 aveSpecificEnthalpy25 aveFluidPowerOrifice25
aveMassFlowOrifice25] =
orificeKatrixEfficiency('matlab-25hz.xls',25,60,1800,'Air_ha',0.01016,0.29);
    [efficiencyOrifice30 aveDensity30 avePin30 aveTin30 avePout30 aveTout30
aveTorque30 aveShaftPower30 aveSpecificEnthalpy30 aveFluidPowerOrifice30
aveMassFlowOrifice30] =
orificeKatrixEfficiency('matlab-30hz.xls',30,60,1800,'Air_ha',0.01016,0.29);
    [efficiencyOrifice35 aveDensity35 avePin35 aveTin35 avePout35 aveTout35
aveTorque35 aveShaftPower35 aveSpecificEnthalpy35 aveFluidPowerOrifice35
aveMassFlowOrifice35] =
orificeKatrixEfficiency('matlab-35hz.xls',35,60,1800,'Air_ha',0.01016,0.29);
    % [efficiencyOrifice40 aveDensity40 avePin40 aveTin40 avePout40 aveTout40
aveTorque40 aveShaftPower40 aveSpecificEnthalpy40 aveFluidPowerOrifice40
aveMassFlowOrifice40] =
orificeKatrixEfficiency('matlab-40hz.xls',40,60,1800,'Air_ha',0.01016,0.29)
    % [efficiencyOrifice45 aveDensity45 avePin45 aveTin45 avePout45 aveTout45
aveTorque45 aveShaftPower45 aveSpecificEnthalpy45 aveFluidPowerOrifice45
aveMassFlowOrifice45] =
orificeKatrixEfficiency('matlab-45hz.xls',45,60,1800,'Air_ha',0.01016,0.29)
    %
    [efficiencyRotameter10 aveMassFlowRotameter10 aveFluidPowerRotameter10]
= rotameterKatrixEfficiency( 26.5, 0.291, aveDensity10, aveSpecificEnthalpy10,
aveShaftPower10 );
    [efficiencyRotameter15 aveMassFlowRotameter15 aveFluidPowerRotameter15]
= rotameterKatrixEfficiency( 29.3, 0.292, aveDensity15, aveSpecificEnthalpy15,
aveShaftPower15 );
    [efficiencyRotameter25 aveMassFlowRotameter25 aveFluidPowerRotameter25]
= rotameterKatrixEfficiency( 33.1, 0.293, aveDensity25, aveSpecificEnthalpy25,
aveShaftPower25 );
```

```matlab
    [efficiencyRotameter30 aveMassFlowRotameter30 aveFluidPowerRotameter30]
= rotameterKatrixEfficiency( 34.2, 0.296, aveDensity30, aveSpecificEnthalpy30,
aveShaftPower30 );
    [efficiencyRotameter35 aveMassFlowRotameter35 aveFluidPowerRotameter35]
= rotameterKatrixEfficiency( 35.7, 0.297, aveDensity35, aveSpecificEnthalpy35,
aveShaftPower35 );
    % [efficiencyRotameter40 aveMassFlowRotameter40
aveFluidPowerRotameter40] = rotameterKatrixEfficiency( 37.7, 0.296,
aveDensity40, aveSpecificEnthalpy40, aveShaftPower40 )
    % [efficiencyRotameter45 aveMassFlowRotameter45
aveFluidPowerRotameter45] = rotameterKatrixEfficiency( 39.0, 0.30, aveDensity45,
aveSpecificEnthalpy45, aveShaftPower45 )
    rotationalSpeed = [300 450 750 900 1050].*(2*pi/60); % rpm to rad/second
    numSamples = length(rotationalSpeed);
    efficiencyOrifice = [efficiencyOrifice10 efficiencyOrifice15 efficiencyOrifice25
efficiencyOrifice30 efficiencyOrifice35 ];
    efficiencyRotameter = [efficiencyRotameter10 efficiencyRotameter15
efficiencyRotameter25 efficiencyRotameter30 efficiencyRotameter35 ];
    fluidPowerOrifice = [aveFluidPowerOrifice10 aveFluidPowerOrifice15
aveFluidPowerOrifice25 aveFluidPowerOrifice30 aveFluidPowerOrifice35 ];
    fluidPowerRotameter = [aveFluidPowerRotameter10 aveFluidPowerRotameter15
aveFluidPowerRotameter25 aveFluidPowerRotameter30 aveFluidPowerRotameter35
];
    massFlowOrifice = [aveMassFlowOrifice10 aveMassFlowOrifice15
aveMassFlowOrifice25 aveMassFlowOrifice30 aveMassFlowOrifice35 ];
    massFlowRotameter = [aveMassFlowRotameter10 aveMassFlowRotameter15
aveMassFlowRotameter25 aveMassFlowRotameter30 aveMassFlowRotameter35 ];
    shaftPower = [aveShaftPower10 aveShaftPower15 aveShaftPower25
aveShaftPower30 aveShaftPower35 ];
    Torque = [aveTorque10 aveTorque15 aveTorque25 aveTorque30 aveTorque35 ];
    Pin = [avePin10 avePin15 avePin25 avePin30 avePin35 ];
    Pout = [avePout10 avePout15 avePout25 avePout30 avePout35 ];
    Tin = [aveTin10 aveTin15 aveTin25 aveTin30 aveTin35 ] + 273.15;% Celsius to
Kelvin
    Tout = [aveTout10 aveTout15 aveTout25 aveTout30 aveTout35 ] + 273.15;%
Celsius to Kelvin
    specificEnthalpy = [aveSpecificEnthalpy10 aveSpecificEnthalpy15
aveSpecificEnthalpy25 aveSpecificEnthalpy30 aveSpecificEnthalpy35 ];
    Pratio = Pin./Pout;
    meanEfficiency = mean([efficiencyOrifice; efficiencyRotameter]);
    meanFluidPower = mean([fluidPowerOrifice; fluidPowerRotameter]);
    meanMassFlow = mean([massFlowOrifice; massFlowRotameter]);
```

stdDevEfficiency = std([efficiencyOrifice; efficiencyRotameter], 1, 1); %one standard deviation based on 2 independent data points, orifice and rotameter

stdDevFluidPower = std([fluidPowerOrifice; fluidPowerRotameter], 1, 1); %one standard deviation based on 2 independent data points, orifice and rotameter

stdDevMassFlow = std([massFlowOrifice; massFlowRotameter], 1, 1); %one standard deviation based on 2 independent data points, orifice and rotameter

accuracyTorque = (0.0025*50).*ones(1,numSamples); % Interface T8-50-A4A, T8-Eco w/ 50 Nm capacity, +/-0.25% combined accuracy

accuracyShaftPower = (accuracyTorque./Torque + 0.01).*shaftPower; % Multiplication, Power = Torque*angular velocity, so add relative error. Yaskawa V1000, +/-1.0% speed regulation in V/f mode

accuracyPin = (0.01*1825042).*ones(1,numSamples); % PX26-250GV, +/-1.0% accuracy, 250psig capacity

accuracyPout = (0.003*2169780).*ones(1,numSamples); % PX181-300G5V, +/-0.3% combined accuracy, 300psig capacity

accuracyTin = 2.2.*ones(1,numSamples); % Omega TJ36-CAXL-18G-6 grounded, type K thermocouple, 2.2 degree ASTM tolerance

accuracyTout = accuracyTin; % Omega TJ36-CAXL-18G-6 grounded, type K thermocouple, ASTM tolerance

accuracyPratio = (accuracyPin./Pin + accuracyPout./Pout).*Pratio; % Division, so add relative error

figure();
errorbar(rotationalSpeed,meanEfficiency,stdDevEfficiency,'o–');
axis([0, 120, 0.5 , 1]);
ylabel('Isentropic efficiency');
xlabel('Rotational speed (radians/second)');
figure();
errorbar(rotationalSpeed,meanFluidPower,stdDevFluidPower,'o–');
hold on;
errorbar(rotationalSpeed,shaftPower,accuracyShaftPower,'–');
axis([0, 120, 0 , 700]);
ylabel('Power (Joules/second)');
xlabel('Rotational speed (radians/second)');
legend('Enthalpy loss of air through expander', 'Mechanical power generated', 'Location', 'Best');
figure();
errorbar(rotationalSpeed,Torque,accuracyTorque,'–');
axis([0, 120, 0 , 15]);
ylabel('Average torque produced (Newton*meter)');
xlabel('Rotational speed (radians/second)');
figure();
errorbar(rotationalSpeed,Pratio,accuracyPratio,'–');
axis([0, 120, 0 , 11]);

```
ylabel('Pressure ratio of expansion');
xlabel('Rotational speed (radians/second)');
figure();
errorbar(rotationalSpeed,Pin,accuracyPin,'o–');
hold on;
errorbar(rotationalSpeed,Pout,accuracyPout,'–');
axis([0, 120, 0 , 1100000]);
ylabel('Pressure (Pascals)');
xlabel('Rotational speed (radians/second)');
legend('Pressure of air at expander inlet', 'Pressure of air at expander outlet',
'Location', 'Best');
figure();
errorbar(rotationalSpeed,Tin,accuracyTin,'o–');
hold on;
errorbar(rotationalSpeed,Tout,accuracyTout,'–');
axis([0, 120, 250, 320]);
ylabel('Temperature (Kelvin)');
xlabel('Rotational speed (radians/second)');
legend('Temperature of air at expander inlet', 'Temperature of air at expander
outlet', 'Location', 'Best');
figure();
plot(rotationalSpeed,specificEnthalpy,'o–');
axis([0, 120, 20000 , 35000]);
ylabel('Specific enthalpy loss of air through expander (Joules/kg)');
xlabel('Rotational speed (radians/second)');
```

6.2   readxlsData.m

```
function [ Torque Pin Pout dP Tin Tout ] = readxlsData( filename )
%readxlsData Reads Torque, Pin, Pout, dP, Tin, Tout from specially formatted
excel spreadsheet.
% It is assumed that the time period of the data samples exactly coincide and that
the sampling period of voltage data is an
%integer multiple of the thermocouple data. For instance, a 0.2 second
%thermocouple sampling period and a 0.4 second voltage sampling period
%having exactly 1500 and 750 samples respectively would work, but a 0.2 and
0.3 sampling periods, respectively, would not.
%
% Input:
% filename: excel spreadsheet filename with data formatted correctly in
% .xls format (e.g. 'matlabdata.xls')
%
```

% Output:
% Torque: a matrix containing time (s) and torque values (N*m) in columns
% Pin: a matrix containing time (s) and input pressure values (Pa) in columns
% Pout: a matrix containing time (s) and output pressure values (Pa) in columns
% dP: a matrix containing time (s) and differential pressure values (Pa) in
% columns
% Tin: a matrix containing time (s) and input temperature (Celsius) values in
% columns
% Tout: a matrix containing time (s) and output temperature (Celsius)
% values in columns
% Excel file read from sheets ignoring label of first column
Torque = xlsread(filename, 'Torque');
Pin = xlsread(filename, 'Pin');
Pout = xlsread(filename, 'Pout');
dP = xlsread(filename, 'dP');
Tin = xlsread(filename, 'Tin');
Tout = xlsread(filename, 'Tout');
% calibrated scale error correction:
% this corrects an incorrect scale (old) that was originally used on the collected differential pressure data for
% the Katrix expander with a corrected scale (new).
% y = mx + b, dP = mnew* (dPold+bold)/mold + bnew + zerobalance
% zerobalance = mold*xold(@dP=0)-bold
% dP(:,2) = 7980.*((dP(:,2)+7818)./7093)-8618+158;
incrementV = length(Pin)/length(Tin);
minLength=min(length(Tin(:,2)),length(Pin(:,2)));
% if sample period for thermocouple is greater than that for voltage
% devices.
if incrementV > 1
%initialize
newTorque=zeros(minLength,2);
newPin=zeros(minLength,2);
newPout=zeros(minLength,2);
newdP=zeros(minLength,2);
j = 1;
% ignore every incrementV (2nd, 3rd, 4th, etc.) reading on the more frequently sampled data
% and overwrite the resulting shorter data set to the same original
% variables of Torque, Pin, Pout, dP.
for i=1:incrementV:length(Pin)
newTorque(j,:) = Torque(i,:);
newPin(j,:) = Pin(i,:);
newPout(j,:) = Pout(i,:);

```
newdP(j,:) = dP(i,:);
j = j+1;
end
Torque = newTorque;
Pin = newPin;
Pout = newPout;
dP = newdP;
% if sample period for thermocouple is less than that for voltage
% data.
elseif incrementV < 1
% initialize
newTin=zeros(minLength,2);
newTout=zeros(minLength,2);
j = 1;
% ignore every incrementV (2nd, 3rd, 4th, etc.) reading on the more frequently
sampled data
% and overwrite the resulting shorter data set to the same original
% variables of Tin, Tout.
for i=1:(1/incrementV):length(Tin)
newTin(j,:) = Tin(i,:);
newTout(j,:) = Tout(i,:);
j = j+1;
end
Tin = newTin;
Tout = newTout;
end
end
```

6.3   orificeKatrixEfficiency.m

```
function [ efficiencyOrifice aveDensity avePin aveTin avePout aveTout aveTorque
aveShaftPower aveSpecificEnthalpy aveFluidPower aveMassFlow] =
orificeKatrixEfficiency( filename, frequency, basefrequency, ratedrpm, workingfluid,
d, orificeRatio)
%katrixEfficiency computes the expander isentropic efficiency, average fluid
density,
%pressure in, temperature in, pressure out, temperature out, torque, shaft power,
%fluid power, and mass flow rate from experimental data stored in specially
formatted excel spreadsheets.
%Flow rate is calculated using data from an orifice plate flow meter, and
%using the Blevins orifice equation. It is assumed that the time period of
```

%the data samples exactly coincide and that the sampling period of voltage data
is an
    %integer multiple of the thermocouple data. For instance, a 0.2 second
    %thermocouple sampling period and a 0.4 second voltage sampling period
    %having exactly 1500 and 750 samples respectively would work, but a 0.2 and
0.3 sampling periods, respectively, would not.
    %
    % Variables;
    %
    % Output:
    % efficiencyOrifice: average isentropic efficiency of expander (0 = 0%, 1 = 100%)
    % aveDensity: average density of working fluid upstream of expander
    % (kg/m^3)
    % avePin: average pressure upstream (Pa)
    % aveTin: average temperature upstream (Celsius)
    % avePout: average pressure downstream (Pa)
    % aveTout: average temperature downstream (Celsius)
    % aveTorque: average torque produced on shaft (N*m)
    % aveShaftPower: average power produced on shaft (J/s)
    % aveSpecificEnthalpy: average specific enthalpy loss across expander
    % (J/kg)
    % aveFluidPower: average fluid enthalpy loss expressed as power (J/s)
    % aveMassFlow: average mass flow rate into the expander (kg/s)
    %
    % Input:
    % filename: excel spreadsheet filename with data formatted correctly in
    % .xls format (e.g. 'matlabdata.xls')
    % frequency: AC frequency provided to induction motor/generator (Hz)
    % baseFrequency: motor nameplate frequency of excitation (Hz)
    % ratedrpm: motor rated speed at nameplate frequency (Hz)
    % workingFluid: EES recognized name of working fluid (e.g. 'Air_ha')
    % d: diameter of orifice in orifice plate flow meter (m)
    % orificeRatio: ratio of diameter of orifice to pipe diameter
    [Torque Pin Pout dP Tin Tout] = readxlsData(filename);
    % Initial value of the velocity of the fluid through the pipe
    % upstream of the orifice. This will iteratively be solved, so need
    % not be correct.
    U = 2; % m/s
    % Initialize
    specificEnthalpy=zeros(minLength,1);
    viscosity=zeros(minLength,1);
    density=zeros(minLength,1);
    mdot=zeros(minLength,1);

109

```matlab
fluidPower=zeros(minLength,1);
shaftPower=zeros(minLength,1);
% Calculate the instantaneous power, enthalpyloss, mass flow, etc. for each
% time step in the data set using the EES/matlab interface.
for i=1:1:length(Tin)
% Calculate the shaftpower (converting from rpm to rad/sec
shaftPower(i) = 2*pi/60 * frequency / basefrequency * ratedrpm * Torque(i,2);
% Calculate specific enthalpy drop in fluid across expander.
specificEnthalpy(i) = EES_Enthalpy(workingfluid,'P',Pin(i,2),'T',Tin(i,2)) -
EES_Enthalpy(workingfluid,'P',Pout(i,2),'T',Tout(i,2));
% Calculate density of fluid in upstream flow.
density(i) = EES_Density( workingfluid, 'P', Pin(i,2), 'T', Tin(i,2));
% Calculate viscosity of fluid in upstream flow.
viscosity(i) = EES_Viscosity( workingfluid, 'P', Pin(i,2), 'T', Tin(i,2));
% Using an iterative algorithm with the Blevins incompressible flow correlation,
calculate the mass
% flow rate based on the orifice plate differential pressure reading and a velocity
guess.
mdot(i) = Blevins(d,orificeRatio,density(i),viscosity(i),dP(i,2),U);
% Calculate the total enthalpy drop of fluid across the expander.
fluidPower(i) = mdot(i)*specificEnthalpy(i);
end
% calculate average values (across the whole dataset) of the above
% calculated instantaneous values.
avePin = mean(Pin(:,2));
aveTin = mean(Tin(:,2));
avePout = mean(Pout(:,2));
aveTout = mean(Tout(:,2));
aveTorque = mean(Torque(:,2));
aveShaftPower = mean(shaftPower);
aveSpecificEnthalpy = mean(specificEnthalpy);
aveFluidPower = mean(fluidPower);
aveDensity = mean(density);
aveMassFlow = mean(mdot);
% average isentropic efficiency across this dataset.
efficiencyOrifice = aveShaftPower/aveFluidPower;
end
```

6.4   Blevins.m

```matlab
function [ mdot ] = Blevins( d, beta, rho, mu, dP, U )
% Blevins mass flow rate for orifice plate with corner tap, incompressible
```

```
% fluid
% source: Blevins Applied Fluid Dynamics Handbook.
%
% Variables:
%
% Output
% mdot: mass flow rate (kg/s)
%
% Input
% d: diameter of orifice (m)
% beta: ratio of diameter of orifice to inner diameter of pipe
% rho: density of working fluid upstream of orifice (kg/m^3)
% mu: viscosity of working fluid upstream of orifice
% dP: differential pressure across the orifice (corner flange)
% U: velocity of air through the pipe
% orifice outer diameter
D = d/beta;
% start with a high mdotdelta to enter the while loop.
mdotdelta = 0.02;
% assume zero mass flow so at least two iterations are always performed in
% while loop.
mdotlast = 0;
while mdotdelta > 0.0001
% Reynolds number of flow through upstream pipe
Re = rho*U*D/mu;
% Blevins 6-40, calculation of discharge coefficient to account for
% viscous losses
C = 0.5959 + 0.0312*beta^2.1 - 0.1840*beta^8 + 91.71*beta^2.5*Re^(-0.75);
% Blevins 6-39, calculation of mass flow rate
mdot = (rho*pi*d^2*C/(4*(1-(beta)^4)^0.5)*(2*dP/rho)^0.5); %kg/s
U = mdot/rho/(pi*(D/2)^2); % m/s
% calculation of difference between this and previous iterations mdot
% result.
mdotdelta = mdot - mdotlast;
% this mdot becomes the previous before returning to the while loop
% condition
mdotlast = mdot;
end
end
```

6.5 rotameterKatrixEfficiency.m

```
function [ rotameterEfficiency mdot fluidPower ] = rotameterKatrixEfficiency(
percentMeasured, highLimit, rho, specificEnthalpy, shaftPower)
%rotameterKatrixEfficiency calculates mass flow rate based on rotameter.
% Using an upstream rotameter with a maximum capacity measured in
% m^3/min, calculates the fluidPower and efficiency of the katrix expander given
% also the average shaft power produced and density and specific enthalpy of the
% air through the rotameter at the time of the reading (steady state).
%
% Variables:
%
% Output
% rotameterEfficiency: isentropic efficiency of the expander (0 = 0%, 1 =
% 100%)
% mdot: mass flow rate of working fluid (kg/s)
% fluidPower: enthalpy loss of working fluid through expander (J/s)
%
% Input
% percentMeasured: flow as percent of scale measured on rotameter (%)
% highLimit: volumeteric flow capacity (100% of scale) of rotameter (m^3/min)
% rho: average density of working fluid through rotameter (kg/m^3)
% specificEnthalpy: average specific enthalpy drop of fluid through expander
(J/kg)
% shaftPower: average shaft power produced by expander (J/s)
% measurement * capacity * density (converted to kg/s)
mdot = percentMeasured/100 * highLimit * rho / 60;
fluidPower = specificEnthalpy * mdot;
%isentropic efficiency of expander based on average rotameter reading
rotameterEfficiency = shaftPower/fluidPower;
end
```

6.6 dpTorquePlot.m

```
close all; clear all; clear classes;
[Torque10 Pin10 Pout10 dP10 Tin10 Tout10] = readxlsData('matlab-10hz.xls');
[Torque15 Pin15 Pout15 dP15 Tin15 Tout15] = readxlsData('matlab-15hz.xls');
[Torque25 Pin25 Pout25 dP25 Tin25 Tout25] = readxlsData('matlab-25hz.xls');
[Torque30 Pin30 Pout30 dP30 Tin30 Tout30] = readxlsData('matlab-30hz.xls');
[Torque35 Pin35 Pout35 dP35 Tin35 Tout35] = readxlsData('matlab-35hz.xls');
[Torque40 Pin40 Pout40 dP40 Tin40 Tout40] = readxlsData('matlab-40hz.xls');
[Torque45 Pin45 Pout45 dP45 Tin45 Tout45] = readxlsData('matlab-45hz.xls');
```

```
x = 1:length(dP10);
x = x.*0.4;
figure();
plot(x, dP10(:,2)./100, '–', x, Torque10(:,2))
ylabel('Torque (N*m) or Pressure (hPa)');
xlabel('time (seconds)');
legend('Differential Pressure across Orifice (hPa)', 'Torque generated on Shaft
(N*m)', 'Location', 'Best');
title('Oscillations at 31.4 rad/sec rotational speed');
figure();
plot(x, dP15(:,2)./100, '–', x, Torque15(:,2))
ylabel('Torque (N*m) or Pressure (hPa)');
xlabel('time (seconds)');
legend('Differential Pressure across Orifice (hPa)', 'Torque generated on Shaft
(N*m)', 'Location', 'Best');
title('Oscillations at 47.1 rad/sec rotational speed');
figure();
plot(x, dP25(:,2)./100, '–', x, Torque25(:,2))
ylabel('Torque (N*m) or Pressure (hPa)');
xlabel('time (seconds)');
legend('Differential Pressure across Orifice (hPa)', 'Torque generated on Shaft
(N*m)', 'Location', 'Best');
title('Oscillations at 78.5 rad/sec rotational speed');
figure();
plot(x, dP30(:,2)./100, '–', x, Torque30(:,2))
ylabel('Torque (N*m) or Pressure (hPa)');
xlabel('time (seconds)');
legend('Differential Pressure across Orifice (hPa)', 'Torque generated on Shaft
(N*m)', 'Location', 'Best');
title('Oscillations at 94.2 rad/sec rotational speed');
figure();
plot(x, dP35(:,2)./100, '–', x, Torque35(:,2))
ylabel('Torque (N*m) or Pressure (hPa)');
xlabel('time (seconds)');
legend('Differential Pressure across Orifice (hPa)', 'Torque generated on Shaft
(N*m)', 'Location', 'Best');
title('Oscillations at 110.0 rad/sec rotational speed');
figure();
plot(x, dP40(:,2)./100, '–', x, Torque40(:,2))
ylabel('Torque (N*m) or Pressure (hPa)');
xlabel('time (seconds)');
legend('Differential Pressure across Orifice (hPa)', 'Torque generated on Shaft
(N*m)', 'Location', 'Best');
```

```matlab
title('Oscillations at 125.7 rad/sec rotational speed');
figure();
plot(x, dP45(:,2)./100, '-', x, Torque45(:,2))
ylabel('Torque (N*m) or Pressure (hPa)');
xlabel('time (seconds)');
legend('Differential Pressure across Orifice (hPa)', 'Torque generated on Shaft
(N*m)', 'Location', 'Best');
title('Oscillations at 141.4 rad/sec rotational speed');
frequency = [34 31 22 15 13 12 9]./300; % number of periods in 300 seconds
rotationalSpeed = [300 450 750 900 1050 1200 1350].*(2*pi/60); % rpm to
rad/second
figure();
plot(rotationalSpeed, frequency, 'o-')
axis([0, 160, 0 , 0.12]);
ylabel('Frequency of Oscillation (Hz)');
xlabel('Rotational Speed (rad/second)');
```